A 3–D Chemistry Transport Model for Titan's Thermosphere

Inaugural-Dissertation
zur Erlangung des Doktorgrades
der Mathematisch-Naturwissenschaftlichen Fakultät
der Universität zu Köln

vorgelegt von

MARTIN C. DOEGE

aus Hamburg

NCAR, Boulder, Colorado, USA
and the University of Cologne

Köln 2010

Berichterstatter (Gutachter):

Prof. Dr. Joachim Saur

Prof. Dr. Michael Kerschgens

Tag der mündlichen Prüfung:

26.1.2011

Contents

1 Current scientific knowledge about Titan **19**
- 1.1 Titan and its atmosphere 19
- 1.2 Atmospheric chemistry on Titan 26
- 1.3 The Cassini-Huygens mission and other available observations . . 30
- 1.4 Modeling efforts and open scientific questions 31

2 Model description **37**
- 2.1 The MOZART Chemistry Transport Model 37
- 2.2 The basic MOZART setup for Titan 39
- 2.3 Discussion 51

3 Model validation **53**
- 3.1 Control experiment chemical distributions 53
- 3.2 Sensitivity to the strength of circulation 84
- 3.3 Fitting observational data to a distribution function 93
- 3.4 Discussion 102

4 Science questions **105**
- 4.1 What is the influence of solar variability on chemistry? 105
  - 4.1.1 Solar minimum run (“SolMin”) 109
  - 4.1.2 Solar maxium run (“SolMax”) 113
  - 4.1.3 Relative changes between Solar minimum and maximum . 118
- 4.2 How do gravitational tides affect composition? 119
- 4.3 Discussion 125

5 Summary and outlook **129**
- 5.1 Further research 130

A Model parameters and reaction rates **133**

B A Titan column chemistry model **145**

C Cassini INMS validation data **151**

D Some names of chemical species **157**

E Glossary and list of abbreviations **159**

List of Figures

1.1 Size comparison between the largest seven Saturn moons. Color variations, except for Titan being slightly reddish, are random. . 20

1.2 Gravitational acceleration in Titan's atmosphere. 21

1.3 Time series of Titan's subsolar latitude for the IAU pole (top) and Stiles *et al.*, 2008 pole (bottom). 23

1.4 Surface map of Titan from Cassini images acquired through August 2008. The seas ("mare") and lakes at the poles are prominent features, as is the equatorial basin of Xanadu. Putative shorelines are indicated in red, or blue if they have been found to change seasonally, as would be expected from a lake. The Huygens landing site (not drawn in) is close to the center of the first map, at 10.34°S and 167°W. Image credit: NASA/JPL/Space Science Institute (slide PIA11146, dated 2009-01-29). 27

1.5 This Voyager 2 photo shows that Titan's surface is completely obscured by layers of haze in visible light. Image credit: NASA . 28

1.6 Dependence of shadow height on zenith angle. 28

1.7 Time series of the daily NOAA Mg II solar activity index (Viereck and Puga, 1999) with its 60-day running average (red line). This index is a good proxy of solar EUV output, which drives photochemistry. The peaks of solar cycles 21 to 23 are clearly visible. 29

2.1 Basic structure of the MOZART Chemistry Transport Model (CTM). 38

2.2 Variability of the Solar spectrum between Solar maximum and Solar minimum, i.e. Solar maximum irradiance divided by Solar minimum irradiance. The strongest variability exists in the most energetic part of extreme ultraviolet (i.e., wavelengths below about 70 nm), while the variation for larger wavelengths is below a factor of two. 41

2.3 Level of maximum radiation absorption (optical depth $\tau = 1$) in Titan's atmosphere as a function of wavelength. 41

2.4 Photolysis coefficients for Solar average conditions for selected species and a zenith angle of 30°. 42

2.5 Factor between Solar max and Solar min photolysis coefficients for selected species and a zenith angle of 30°. 43

2.6 Photolysis coefficients around Titan (shown in gray) for (a) C_2H_2, (b) C_3H_8, and (c) CH_4, with the Solar rays coming from the right (3 o'clock) side of the plot and the atmosphere being shown between the surface and 1,200 km altitude. 44

2.7 Combined grid with pressure levels from the T-GITM (red area) and TitanWRF (green area) GCMs (left panel), global-average temperature profile with shaded range of minima and maxima (center panel), and eddy-diffusion profile used by MOZART. . . . 45

2.8 Zonal-average, time-average meridional wind v (left panel) and zonal wind u (right panel). 47

2.9 Zonal average (left panel) and transformed Eulerian Mean (TEM) circulation (right panel) in kg/s. 47

2.10 Time-average Transformed Eulerian Mean (TEM) vertical wind w^* in mm/s at 45°N/ S and at the equator. 48

2.11 Highly simplified Titan chemistry scheme, showing how long-lived heavy species (blue) are produced from methane via shorter-lived intermediate species (yellow). Atomic and molecular hydrogen (green) take part in many reactions of the scheme, therefore their concentrations are crtitical to the overall stability of the chemistry scheme. 50

3.1 2–D and 1–D views of acetylene lifetime: on the left, colored related to the logarithm of lifetime and on the right, average profiles at the equator. If the base-10 logarithms of the various lifetimes are l_1, l_2, and l_3, and m is their minimum value, then the colors in the first plot are computed as Red = max(0, $1 - 0.3(l_1 - m)$), and analogously for Green (with l_2) and Blue (with l_3). 56

3.2 Like Fig. 3.1, but for C_4H_6. 56

3.3 Like Fig. 3.1, but for C_3H_8. 57

3.4 Methane (a) zonal-mean production-minus-loss rate [cm^{-3}s^{-1}], (b) zonal-mean VMR, and VMR at about 1,019 km altitude, (c) colored the same as in (b) and with contours labeled in VMR, and (d) as a fraction of the VMR maximum on that level to show the horizontal distribution more clearly. 60
3.5 Same as Fig. 3.4, but for CH_3. 61
3.6 Same as Fig. 3.4, but for C_2H_2. 62
3.7 Same as Fig. 3.4, but for C_2H_4. 63
3.8 Same as Fig. 3.4, but for C_2H_6. 64
3.9 Same as Fig. 3.4, but for C_3H_8. 65
3.10 Same as Fig. 3.4, but for C_4H_2. 66
3.11 Same as Fig. 3.4, but for C_6H_6. 67
3.12 Same as Fig. 3.4, but for HCN. 68
3.13 Same as Fig. 3.4, but for HC_3N. 69
3.14 Same as Fig. 3.4, but for C_2N_2. 70
3.15 Maximum diurnal amplitude of VMR in percentage of mean VMR (left) and Local Solar Time (in Titan hours) of maximum concentration, both for ethane. 71
3.16 Scatter plots comparing INMS measurements above 1,000 km altitude (horizontal axis) and corresponding MOZART values (vertical axis) from the Control run for (a) C_2H_6, (b) C_3H_8, (c) C_4H_2, (d) C_4H_6, (e) C_6H_6, and (f) CH_3C_2H. The Spearman rank correlation and best-fit line (green) as well as the slope-one line (red) are also shown. 73
3.17 Same as Fig. 3.16, but for (a) C_2N_2, (b) HC_3N, and (c) CH_3CN. 74
3.18 Scatter plots comparing all INMS measurements (horizontal axis) and corresponding MOZART values (vertical axis) from the Control run for (a) C_2H_6, (b) C_3H_8, (c) C_4H_2, (d) C_4H_6, (e) C_6H_6, and (f) CH_3C_2H. The Spearman rank correlation and best-fit line (green) as well as the slope-one line (red) are also shown. Data for heights above 1,000 km is colored blue, data for 975 km and below green, and data in between red. 75
3.19 Same as Fig. 3.18, but for (a) C_2N_2, (b) HC_3N, and (c) CH_3CN. 76
3.20 CH_3 loss rates for the equator with the Sun at the zenith. 77
3.21 Global-average VMR profiles for selected species from the Control run with measurements from Cui *et al.* (2009). (The measured value for propane is meant to represent an upper bound.) 79
3.22 Global-average total VMR profiles for each class of species, where the class number corresponds to the number of carbon atoms in the molecule. 80

3.23 Propargyl radical (a) production and (b) loss rates for the equator with the Sun at the zenith. 82

3.24 Scatter plots comparing INMS measurements above 1,000 km altitude (horizontal axis) and corresponding MOZART values (vertical axis) from the Zero run for (a) C_2H_6, (b) C_3H_8, (c) C_4H_2, (d) C_4H_6, (e) C_6H_6, and (f) CH_3C_2H. The Spearman rank correlation and best-fit line (green) as well as the slope-one line (red) are also shown. 86

3.25 Same as Fig. 3.24, but for (a) C_2N_2, (b) HC_3N, and (c) CH_3CN. 87

3.26 Scatter plots comparing all INMS measurements (horizontal axis) and corresponding MOZART values (vertical axis) from the Zero run for (a) C_2H_6, (b) C_3H_8, (c) C_4H_2, (d) C_4H_6, (e) C_6H_6, and (f) CH_3C_2H. The Spearman rank correlation and best-fit line (green) as well as the slope-one line (red) are also shown. Data for heights above 1,000 km is colored blue, data for 975 km and below green, and data in between red. 88

3.27 Same as Fig. 3.26, but for (a) C_2N_2, (b) HC_3N, and (c) CH_3CN. 89

3.28 Relative differences for C_2H_6 VMR (Zero/Control -1). The red contour corresponds to no change in concentration. 90

3.29 Same as 3.28, but for C_3H_8. 91

3.30 Same as 3.28, but for HC_3N. 91

3.31 Scatter plots comparing INMS measurements above 1,000 km altitude (horizontal axis) and corresponding MOZART values (vertical axis) from the V-Sens run for (a) C_2H_6, (b) C_3H_8, (c) C_4H_2, (d) C_4H_6, (e) C_6H_6, and (f) CH_3C_2H. The Spearman rank correlation and best-fit line (green) as well as the slope-one line (red) are also shown. 94

3.32 Same as Fig. 3.31, but for (a) C_2N_2, (b) HC_3N, and (c) CH_3CN. 95

3.33 Scatter plots comparing all INMS measurements (horizontal axis) and corresponding MOZART values (vertical axis) from the V-Sens run for (a) C_2H_6, (b) C_3H_8, (c) C_4H_2, (d) C_4H_6, (e) C_6H_6, and (f) CH_3C_2H. The Spearman rank correlation and best-fit line (green) as well as the slope-one line (red) are also shown. Data for heights above 1,000 km is colored blue, data for 975 km and below green, and data in between red. 96

3.34 Same as Fig. 3.33, but for (a) C_2N_2, (b) HC_3N, and (c) CH_3CN. 97

3.35 Least-squares best-fit horizontal distributions at 1,020 km height for (a) C_2H_6, (b) C_3H_8, (c) C_4H_2, and (d) C_6H_6 using data points for 1,000 km altitude and above. 99

3.36 ODR best-fit horizontal distributions at 1,020 km height for (a) HC_3N, (b) C_2H_6, (c) C_4H_2, and (d) CH_3C_2H using data points for 1,000 km altitude and above. 101

4.1 Zonal average (left panel) and transformed Eulerian Mean (TEM) circulation (right) for Solar maximum, both in kg/s. 107

4.2 Zonal average (left panel) and transformed Eulerian Mean (TEM) circulation (right) for Solar minimum, both in kg/s. 107

4.3 Average change in temperature from Solar Min to Solar Max. Maximum warming occurs at around 1,000 km height. 108

4.4 Scatter plots comparing INMS measurements above 1,000 km altitude (horizontal axis) and corresponding MOZART values (vertical axis) from the SolMin run for (a) C_2H_6, (b) C_3H_8, (c) C_4H_2, (d) C_4H_6, (e) C_6H_6, and (f) CH_3C_2H. The Spearman rank correlation and best-fit line (green) as well as the slope-one line (red) are also shown. 110

4.5 Same as Fig. 4.4, but for (a) C_2N_2, (b) HC_3N, and (c) CH_3CN. . 111

4.6 Scatter plots comparing INMS measurements above 1,000 km altitude (horizontal axis) and corresponding MOZART values (vertical axis) from the SolMax run for (a) C_2H_6, (b) C_3H_8, (c) C_4H_2, (d) C_4H_6, (e) C_6H_6, and (f) CH_3C_2H. The Spearman rank correlation and best-fit line (green) as well as the slope-one line (red) are also shown. 114

4.7 Same as Fig. 4.6, but for (a) C_2N_2, (b) HC_3N, and (c) CH_3CN. . 115

4.8 Percentual change in zonal-average concentration between Solar Min and Solar Max for $^1CH_2$. 117

4.9 Percentual changes in zonal-average concentrations between Solar Min and Solar Max for (a) CH_4, (b) C_2H_4, (c) C_2H_6, (d) C_2N_2, (e) HCN, and (f) HC_3N. 120

4.10 CH_4 zonal-mean VMR (top panels) and temperatures (bottom panels) for two opposite phases of the wave. 122

4.11 Like Fig. 4.10, but for C_2H_6. 123

4.12 Like Fig. 4.10, but for C_3H_5. 123

4.13 Like Fig. 4.10, but for C_3H_8. 124

4.14 Instantaneous global-average VMR profiles for selected species from the Wave run with measurements from Cui *et al.* (2009). (The measured value for propane is meant to represent an upper bound.) 125

4.15 Percentual changes in concentrations due to the temperature disturbance for (a) CH_4, (b) C_2H_6, (c) C_3H_8, (d) C_4H_8, (e) C_4H_{10}, and (f) HCN. 126

B.1 Sample output from the Titan column model using an earlier version of the chemistry scheme, showing the time evolution of the benzene profile. Time interval between profiles is 100,000 s ($27.\overline{7}$ Earth hours) and the run begins with the initial benzene profile (blue line on the left), then quickly converges toward a relatively stable profile at $t = 900,000$ s (250 Earth hours). . . . 150

List of Tables

1.1 Some selected characteristics of Titan and its atmosphere. Orbital data taken from JPL HORIZONS interactive ephemeris system (Giorgini *et al.*, 1996). 22

2.1 Solution and fixed chemical species in the model. 50

3.1 Global averages for a height of about 1,025 km from Cassini measurements and the MOZART Control experiment. 54
3.2 Global-average chemical lifetimes for selected species at 1,025 km altitude. 55
3.3 Dominant species for each class, based on number of carbon atoms. 79
3.4 Best-fit VMR maxima locations for selected species. 100

4.1 Correlations between temperature and VMR for selected species. Most species are higher in concentration when the temperature is below average. 124

Abstract

A 3–D model of the atmospheric chemistry of Saturn's moon Titan has been constructed which incorporates some of the latest advances of 1–D Titan chemistry models as well as 3–D GCMs for Titan in simplified-enough way that integrations covering many Earth years are numerically feasible. The thermosphere, with its shorter transport and chemistry time scales, reasonably simple circulation, and basic 3–D coverage of the moon with Cassini INMS observations, is the primary focus of this study.

The model is first validated as far as possible against the observations, showing that it performs quite well for most species, given the general margins of error and uncertainties inherent in Titan modeling. Winds are not seen to have the same overriding influence on concentrations as an earlier study using a pre-Cassini GCM wind field suggested (Doege *et al.*, 2008), but nonetheless many species such as ethane exhibit sensitivity to advection and a chemistry transport model with advection does improve the fit to observations over a model with only diffusive transport. Overall it is found that state-of-the-art GCMs for Titan deliver winds realistic enough for the chemistry model to correctly reproduce the basic shapes of chemical species distributions with a variety of chemical lifetimes. In some instances, the limitations of the Cassini measurements become apparent and model results point to difficulties and uncertainties with the INMS data retrieval process (e.g. for C_4H_6) that would be less conspicuous by analyzing only Cassini observations without a model.

Then some specific scientific topics are explored, namely the influence of the Solar cycle and of vertically-propagating tidal waves. As the Cassini measurements so far cover a period of decreasing and generally below-average Solar activity, Solar minimum conditions are particularly of interest, because chemistry models for Titan have so far normally been run for Solar average UV output. It is found that some species such as propane react strongly to changes in Solar irradiance and the resulting concentrations of primary photolysis products. However, chemical distributions remain recognizable from the Control experiment and accounting for the Solar cycle does not resolve remaining issues with chemistry

schemes for Titan's atmosphere.

Atmospheric tidal waves which are forced mainly in the lower atmosphere also influence the thermosphere significantly, therefore the possbility that chemical concentrations might be measurably affected by these waves is explored with the model. The conclusion is drawn that the effects of such waves through their temperature perturbations alone, while they are easily detectable in the model, might be too weak to identify them in Cassini measurements.

Zusammenfassung

Diese Arbeit beschäftigt sich mit der atmosphärischen Chemie des Saturnmondes Titan anhand eines 3–D Modells basierend auf MOZART. Dabei wird die Atmosphäre zwischen dem Boden und einer Höhe von etwa 1,200 km unter Verwendung von Wind- und Temperaturfeldern aus Titan-GCMs simuliert.

Zunächst wird das Modell gegenüber den vorhandenen Cassini-Messdaten validiert. Dabei stellt sich heraus, dass der Einfluß der Advektion auf die chemischen Konzentrationen in der Thermosphäre geringer ausfällt als in früheren Versuchen, bei denen stärkere Windfelder aus einem prä-Cassini GCM verwendet wurden. Dennoch findet sich bei chemisch langlebigeren Spezies wie Ethan noch ein deutlicher Advektionseinfluss, und es wird festgestellt, dass die Berücksichtigung von Advektion eine Verbesserung der Übereinstimmung mit den Messdaten liefert. Darüberhinaus bestätigt es die schwächere thermosphärische Meridionalzirkulation in neueren GCMs, da die gemessenen chemischen Gradienten mit diesen besser übereinstimmen als solche bei stärkerer Zirkulation (Doege *et al.*, 2008). Teilweise zeigt sich jedoch auch, dass Vergleiche mit Messdaten dadurch erschwert werden, dass diese hohe Ungenauigkeiten in der Höhe besitzen, was bei Spezies mit starken vertikalen Gradienten in der Thermosphäre das Auffinden horizontaler Gradienten in den Konzentrationen erschwert. Einige Spezies weichen so stark von Modell ab (z.B. C_4H_6), dass Probleme und Unsicherheiten im Retrieval der Cassini-Daten als Erklärung am wahrscheinlichsten sind.

In Analogie zu den im Modell beobachteten Feldern wird anschließend versucht mithilfe statistischer Optimierungsfunktionen Horizontalverteilungen an die Messdaten anzupassen. Durch die geringe Zahl der Messdaten ist solch ein Verfahren zwangsläufig spekulativer, aber es zeigt sich dass durchaus statistische signifikante Ergebnisse für einige Spezies erreicht werden, die mit den Modelldaten vergleichbar sind. Eine rein statistische Auswertung der Messdaten, gestützt aus minimale Annahmen aus dem Modell, kann daher einen Beitrag leisten, Erkenntnisse über die Chemie aus punktuellen Messdaten global auszudehnen.

Schließlich werden wissenschaftliche Fragen anhand des Modells untersucht, zum einen die Auswirkungen solarer Variabilität auf die chemischen Verteilun-

gen, zum anderen der Effekt von sich aufwärts ausbreitenden Gezeitenwellen. Die Cassini-Messdaten wurden über Jahre hinweg und daher zu leicht unterschiedlichen Zeiten im Aktivitätszyklus gemacht; außerdem benutzten bisherige Titan-Chemiemodelle jeweils mittlere Sonnenaktivität. Dabei wird festgestellt, dass einige langlebige Spezies wie Propan stark von der Sonnenaktivität abhängen, da ihre Entstehung und Vernichtung auf Photolyseprodukten beruhen. Insgesamt stellt man aber fest, dass Berücksichtigung der Sonnenaktivität nur bedingte Verbesserungen gegenüber dem Kontrollexperiment bietet, da Unsicherheiten bei den chemischen Reaktionsraten davon unabhängig bestehen.

Zum Abschluß wird der Einfluß einer Gezeitenwellen-Temperaturanomalie auf die Konzentrationen untersucht. Diese Temperaturanomalien nehmen durch Veränderung der Reaktionsraten Einfluß auf die Chemie, und die Fragestellung ist ob dieser Einfluß stark genug ist um in Messdaten nachgewiesen zu werden. Vergleich der Konzentrationsschwankungen mit den Messungen ergibt dass der Effekt vermutlich zu schwach ist um anhand der vorhandenen Messdaten sicher nachgewiesen werden zu können.

Introduction

Titan has long been the subject of scientific investigation, although it has had a remarkable ability to resist closer scrutiny for a long time after its 17th-century discovery. From its—in visible light—impermeable haze layers keeping its surface out of view to long-standing questions about its radius and surface features, from first limited evidence of organic chemistry taking place to the still-unsolved problem of the long-term stability of its atmospheric methane, Titan has always been able to pose interesting questions and challenges.

The still-ongoing Cassini mission to the Saturnian system, with its occasional fly-bys of Titan, has delivered a wealth of new data, but measurements, especially of atmospheric constituents, are still quite limited in their spatial and temporal scope as well as accuracy. Further missions to Titan are already in the planning stages, as it is realized that the Cassini mission, while it has advanced the scientific understanding of Titan considerably, has not been able to provide all the necessary answers.

Modeling Titan's atmospheric chemistry is fraught with difficulty because lab measurements of desired rate coefficients are not always available for Titan's temperature conditions and as the nunber and certainty of observations are low compared to Earth. It is sometimes hard to even discern whether a model or the retrieval of measurements are to blame for discrepancies between model and observations.

Therefore modeling studies of Titan's atmosphere, whether of its dynamics or chemistry, are often quickly eclipsed by newer observations or more complex models. While models of Titan's atmospheric chemistry have made important progress due to Cassini observations, many questions about e.g. the role of surface reactions on haze particles remain unanswered and will probably only be solved by additional measurements of reaction rates in the lab rather than by model studies.

Chapter 1

Current scientific knowledge about Titan

1.1 Titan and its atmosphere

Titan, Saturn's largest moon (Fig. 1.1) and the second-largest satellite in the Solar System (second only to Jupiter's moon Ganymede), has long intrigued scientists, as ground-based observations revealed it possesses a thick nitrogen atmosphere, with a surface pressure similar to Earth's, something no other moon in the solar system boasts. Early observations from Earth could unfortunately not establish the chemical composition very firmly, although it was known that methane existed in the atmosphere, but the mixing ratio estimates varied (Yung *et al.*, 1984). Also, no surface features could be distinguished due to haze in the atmosphere. Sagan and Khare (1979) postulated that photolysis of methane and nitrogen by solar UV radiation led to the formation of what he termed *tholins* (from Ancient Greek "tholos" for mud), a reddish-brown organic aerosol, explaining the observed color of Titan.

General characteristics

Table 1.1 lists some of the basic characteristics of Titan. Discovered in 1655 by Dutch mathematician, physicist, and astronomer Christaan Huygens (1629–1695; also known for the Huygens–Fresnel principle in physics), the Saturnian moon was named Titan by John Herschel (1792–1871) in 1847 (Lassell, 1847). In 1944, Gerard P. Kuiper discovered that Titan had an atmosphere (Kuiper, 1944).

In 1981, Voyager 1 observations revealed that Titan's atmosphere was more dense than Kuiper had calculated, having about 1.45 times Earth's atmospheric surface pressure at sea level (Coustenis and Taylor, 2008). The vertical struc-

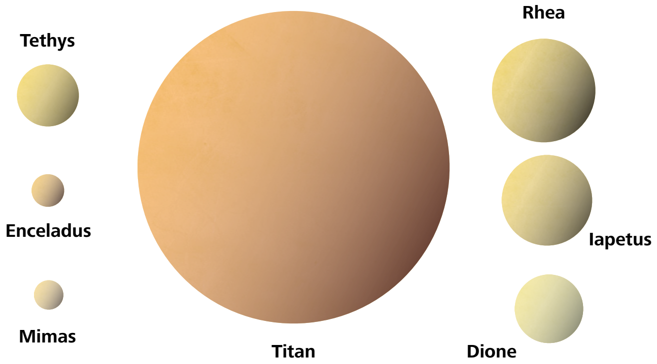

Figure 1.1: Size comparison between the largest seven Saturn moons. Color variations, except for Titan being slightly reddish, are random.

ture of the atmosphere was partly known from Voyager IRIS and occultation measurements, which yielded temperature profiles for altitudes below 300 km altitude, while Voyager UVS measurements gave a clue to the temperatures above 1,000 km altitude—in between, temperatures had to be modeled based on assumed chemical distributions (Yelle *et al.*, 1997). The latter model was also used to predict the descent of the Huygens lander.

The atmosphere is primarily composed of molecular nitrogen (N_2, about 98%) and methane (CH_4, about 2%) with other hydrocarbon and nitrile species being present in minute amounts (Cui *et al.*, 2009). Still, this "organic factory" (Atreya, 2007), the complex chemistry that produces a wide range of hydrocarbons and nitriles, starting with photolysis of nitrogen and methane, is singular in the Solar system and explains Titan's attraction as a subject of chemistry modeling, starting with the column model of Yung *et al.* (1984).

As on Earth, Titan's atmosphere is vertically divided into a tropo-, strato-, meso-, and thermosphere. In the tropo- and mesosphere, temperature decreases with height, while in the strato- and thermosphere there is an increase. Measurements by Cassini's Huygens Atmospheric Structure Instrument (HASI) suggest that the tropo-, strato-, and mesopause are located at heights of about 44 km, 250 km, and 490 km, respectively (Fig. 2 in Fulchignoni *et al.*, 2005). The same analysis yields minimum and maxium atmospheric temperatures (up to a height of about 1,400 km) of about 70 K at the tropopause and 200 K in a wave-like temperature perturbation in the thermosphere at about 1,000 km height, respectively.

Titan's orbit around Saturn causes it to experience an annual cycle of about

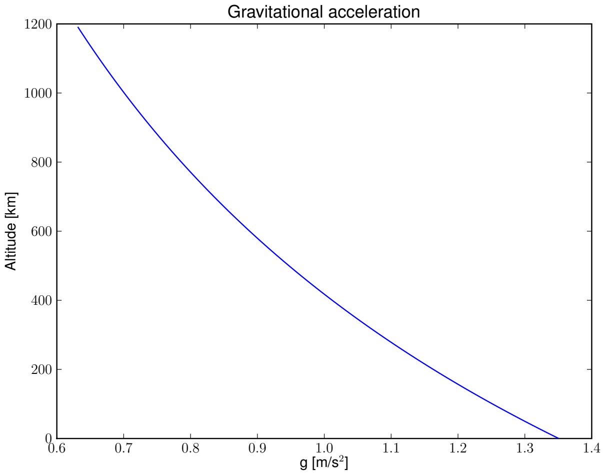

Figure 1.2: Gravitational acceleration in Titan's atmosphere.

30 Earth years. This, coupled with its strong obliquity (see corresponding subsection about the rotation axis), produces strong seasonality. Since Titan's rotation is so slow (see Appendix B for more Titan parameters), with a period of about 16 days, a global Hadley cell develops in the atmosphere, which shifts with the subsolar latitude. Most of the time, the circulation is extremely lopsided and consists of a single cell between the summer and winter hemisphere, but at equinox a symmetrical Hadley circulation can develop, which persists only a comparatively short time (Tokano *et al.*, 1999).

The atmospheric scale height $H = kT/mg$ (McEwan and Philips, 1975), with k the Boltzmann constant, T the temperature, m the molecular mass, and g the gravitational acceleration, suggests that Titan's atmosphere should have the observed large vertical extent (i.e., a much larger scale height than Earth's atmosphere), because compared to Earth, T is about 50% lower, m is about the same, and g is not only about a factor of 7 lower at the surface than on Earth, but also drops quickly with altitude (Fig. 1.2), so that the thermosphere only experiences a 14th of the g at Earth's surface.

Location of Titan's rotation axis

Firstly, one has to make clear that when referring to Titan's obliquity, one is referring to the inclination of its rotation axis in relation to Saturn's orbital plane, not Titan's, because it is the motion of Saturn around the Sun that causes the seasonal cycle on Titan. The obliquity of Titan against its own orbit is very small, so that in other words one can more or less assume that the rotation axes

Average distance from the Sun	9.54 AU (1.32 light hours)
Average distance from Saturn	1,221,870 km (4.08 light seconds)
Orbital period	15.95 Earth days
Mass	1.35×10^{23} kg (Jacobson *et al.*, 2006) $\approx$ 2.3% of Earth's mass
Length of year	29.45 Earth years (same as Saturn's)
Inclination	0.34854°to Saturn's equator
Mean radius	2,576 km (Jacobson *et al.*, 2006)
Equatorial gravitational acceleration	1.35 m/s^2 $\approx$ 14% of Earth's g
Main atmospheric gases	98.4% nitrogen; 1.6% methane, nitriles, and hydrocarbons
Surface pressure	1,467 hPa $\approx$ 145% of Earth's p_0
Surface temperature	93.7 ± 0.6 K (at 530 cm^{-1} from CIRS; Mitri *et al.,* 2007)

Table 1.1: Some selected characteristics of Titan and its atmosphere. Orbital data taken from JPL HORIZONS interactive ephemeris system (Giorgini *et al.*, 1996).

of Saturn and Titan are parallel.

Before measurements of the location of Titan's rotation axis existed, Titan was simply assumed to have an obliquity of 26.7°like Saturn. This turns out to be a relatively good estimate, because a more accurate determination of the pole position reveals that Titan does *not* have zero obliquity in reference to its own orbit (Stiles *et al.*, 2008). This combines with the 0.35°inclination of Titan's orbit around Saturn to give an obliquity of about 26.7°for Titan.

The time evolutions of the subsolar latitude are plotted in Fig. 1.3, showing the differences between the older IAU assumption (zero obliquity) and the latest observations. The former gives a maximum subsolar latitude of 26.4°, the latter of 26.7°. The position data for the Sun in relation to Titan used here comes from the JPL HORIZONS interactive ephemeris system (`http://ssd.jpl.nasa.gov/?horizons`; Giorgini *et al.*, 1996), while the pole positions in RA and Dec are based on the Stiles *et al.* text (their Table 1).

Atmospheric superrotation

An important feature that dynamical models of Titan's atmosphere have to reproduce is the strong westerly (i.e., eastward) jet with wind speeds on the order of several hundred meters per second. How this superrotation is maintained has also been investigated analytically (Zhu, 2006), with the result that the vertical profile of Solar heating has to be tweaked somewhat from its real shape to achieve superroation. Therefore, Titan's atmospheric superrotation cannot be considered to be fully understood at this time.

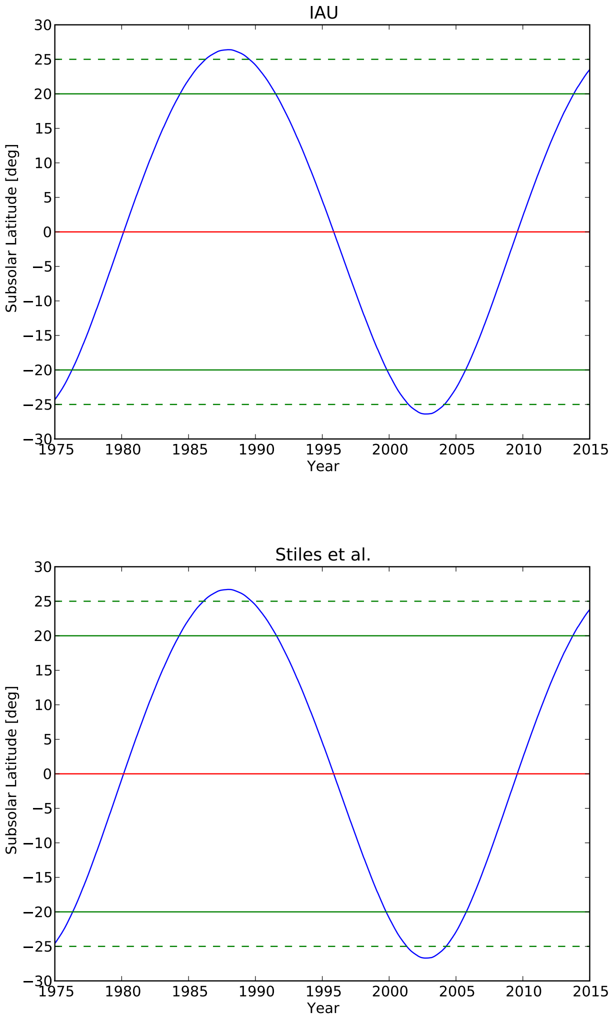

Figure 1.3: Time series of Titan's subsolar latitude for the IAU pole (top) and Stiles *et al.*, 2008 pole (bottom).

Atmospheric haze

Formation of haze in Titan's atmosphere is a facet of Titan's chemistry which is also not very well understood. Initially it was thought that haze formation was confined mainly to the tropo- and stratosphere ("bottom up haze"; McKay *et al.*, 2001), but this view has been replaced with the realization that haze formation must also begin in the high-activity photolysis zone of the thermosphere ("top down haze"; e.g. postulated in Liang *et al.*, 2007b), while the stratosphere remains an important source of haze formation.

It is clear that the photolysis of methane and molecular nitrogen first has to lead to heavier products like benzene, which then ultimately condense and coagulate into irregularly-shaped ("fractal") haze particles. How this process works exactly is still a matter of discussion, however. In chemistry models, haze production comes from the heaviest species represented in the model, but in a slightly ad-hoc formulation. Heavier species are in these models then regarded as a proxy for haze formation, which makes intuitive sense, but is difficult to quantify.

Controversy about benzene

Both the scientists who retrieve chemical concentrations from Cassini data as well as chemistry modelers generally tend to (more or less implicitly) assume that C_6H_6 equals benzene. This is of course not strictly the case (Ralph Kaiser, pers. comm.). Benzene is just *one* arrangement of six carbon and six hydrogen atoms into a molecule. When only the mass of a species is known from a spectrometer, as is the case for INMS, then this does not automatically also pinpoint the relevant isomer. Other isomers for C_6H_6 exist: Dewar benzene, fulvene, prismane, and [3]radialene. This raises the possbility that the problems that chemistry models have with reproducing realistic distributions of C_6H_6 stem at least partly from the fact that the observed C_6H_6 is only partially made up of benzene. This scientific controversy (with some believing that *all* C_6H_6 is benzene, and others thinking that perhaps only *some* of it is) highlights the problems that exist with understanding Titan's chemistry, particularly the products that are supposed to lead up to haze production in this case: If there is no certainty which chemical species Cassini has detected, then naturally chemistry models might be expected to have difficulties explaining observations.

Detached haze lazers

Another puzzling feature of Titan's haze is that above the main haze layer, between about 200 and 500 km height (Porco *et al.*, 2005), there are several detached haze layers with relatively sharp vertical definition. Several explanations have been put forward (e.g. purely as the result of advection, or condensation in the cold-temperature cycle of a gravitational tidal wave [Walterscheid and Schubert, 2006]), but the problem cannot be regarded as solved yet. Teanby *et al.* (2009) found evidence of thin haze layers in the NP strato- and mesosphere with a vertical wavelength of about 50 km and attribute this to dynamical influences, i.e. latitudinal advection across the winter pole polar vortex boundary. Other possible explanations they put forward are compression by gravitational tides (which however would only lead to VMR variations of about 0.2%, far below the observed variations of up to a factor of 50), the effect of gravitational wave temperature anomalies (which however have not been observed in the strato- and mesosphere), or catalytic destruction of trace species on haze particles, i.e. heterogeneous chemistry, which could explain composition minima, but relies on preexisting haze layering, e.g. by tides.

Haze color and composition

Finally, a seemingly very simple question about Titan's haze, namely why it is orange-brown, is also not really answered. Photochemical smog on Earth has a brown tint due to the presence of NO_x, but this is not the case for Titan. Hydrogen cyanide polymers are a possible candiate for the color of the haze (Matthews, 1995) as well as the yellow-orange-red color of Jupiter and Saturn, but unfortunately these tend to require the presence of water to form. Titan's *tholins* could either be linear chains or aromatic structures (or a mix of both) and the pathways leading to their formation are thought to be either polymerization of C_2H_2 and HC_3N, or of HCN, or of polyynes like C_4H_2 (Lebonnois *et al.*, 2002). On the other hand, *tholins* are not true polymers, because they are not made up of identical structures (Ruiz-Bermejo *et al.*, 2009), which makes understanding their chemical evolution even more challenging, therefore no conclusive explanation for their observed color has been found so far.

Surface features

It was initially assumed that more or less the entire surface of Titan might be covered with seas and therefore it was thought the Huygens lander might touch down in a global hydrocarbon ocean. This was not the case, and while Huygens images from the descent showed some surface features in the distance that might be interpreted as a shoreline, there was no definite confirmation of hydrocarbon lakes from Huygens.

The Cassini RADAR mapper found very smooth surface areas near the poles that reflected very little of the radar beam back to the probe (Stofan *et al.*, 2006). These were then called lakes, although they could really only be called confirmed when VIMS spectroscopy found the signature of liquid ethane in the lakes (Brown *et al.*, 2008).

The interaction between these lakes and the atmosphere is caused by evaporation, which according to model studies (Tokano, 2009) creates land and sea breezes due to the temperature contrasts between (in the first case) the warm lake and the cool surface around, or (in the second case) the reverse situation. The convergence of atmospheric moisture over the lake (in the case of the land breeze) then increases precipitation over the lake.

Near the equator, the radar-bright region called Xanadu (see surface map in Fig. 1.4) was initially thought to be a mountain, but the pattern of dunes around Xanadu turned out to be only consistent with it being a basin, according to GCM studies (Tokano, 2008). This was later tentatively confirmed by Cassini altimetry (Zebker *et al.*, 2009). Also, dunes are found in the equatorial region, the shape of which suggests transport by westerly winds. But since time-average winds near the equator on Titan are likely easterly, as they are on Earth, it has been suggested that intermittent episodes of strong westerlies could be the cause of their shape, while easterlies are prevailing but too weak to contribute to transport (Tokano, 2010).

Based on an analysis of the fractal dimension of Titan's North polar lakes, the topography seems to be simpler—in the sense of a lower power spectrum exponent—than the topographies of Earth or Venus (Sharma and Byrne, 2010). The same analysis suggests there are longitudinal differences in the respective importance of different geological processes that have shaped Titan's surface.

1.2 Atmospheric chemistry on Titan

In comparison to Earth's atmospheric chemistry, Titan is distinguished by its extensive hydrocarbon chemistry, started by dissociation of methane and molecular nitrogen by UV radiation and energetic particles, and the large vertical extent of the atmosphere, which causes significant photolysis on what is—at least near the ground—the night side of Titan.

In March 2009, Titan experienced a series of solar eclipses caused by the shadow of Saturn. Unfortunately, no Cassini measurements of the response of atmospheric chemistry to a temporary drop in photolysis have been made.

Solar activity influences Titan chemistry through the variability of Solar extreme ultraviolet (EUV) radiation output. The F10.7 index is commonly used as a proxy for Solar EUV output, but other indices have also been developed to provide a better correlation, notably the NOAA Mg II core-to-wing ratio index (Viereck and Puga, 1999; latest version available from `http://www.swpc.noaa.gov/ftpdir/sbuv/NOAAMgII.dat`), which is computed by taking the ratio of

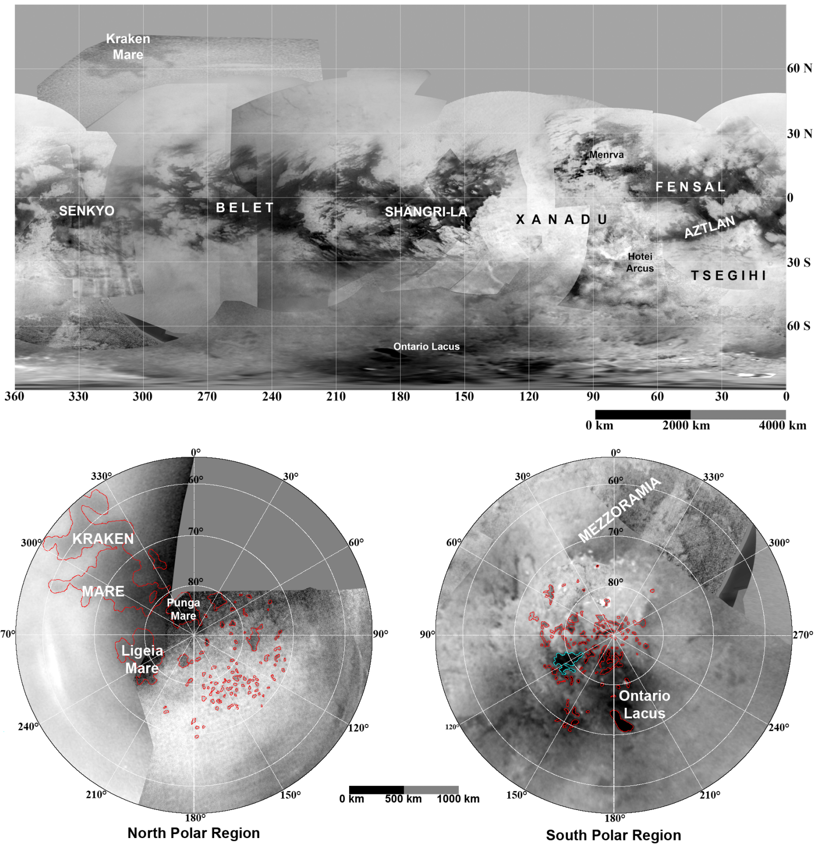
Kraken Mare
60 N
30 N
0
30 S
60 S
Menrva
FENSAL
SENKYO
BELET
SHANGRI-LA
XANADU
AZTLAN
Hotei Arcus
TSEGIHI
Ontario Lacus
360
330
300
270
240
210
180
150
120
90
60
30
0
0 km
2000 km
4000 km
0°
30°
60°
90°
120°
150°
180°
210°
240°
270°
300°
330°
60°
70°
80°
KRAKEN
MARE
Punga Mare
Ligeia Mare
0 km
500 km
1000 km
North Polar Region
MEZZORAMIA
Ontario Lacus
South Polar Region

Figure 1.4: Surface map of Titan from Cassini images acquired through August 2008. The seas ("mare") and lakes at the poles are prominent features, as is the equatorial basin of Xanadu. Putative shorelines are indicated in red, or blue if they have been found to change seasonally, as would be expected from a lake. The Huygens landing site (not drawn in) is close to the center of the first map, at 10.34°S and 167°W. Image credit: NASA/JPL/Space Science Institute (slide PIA11146, dated 2009-01-29).

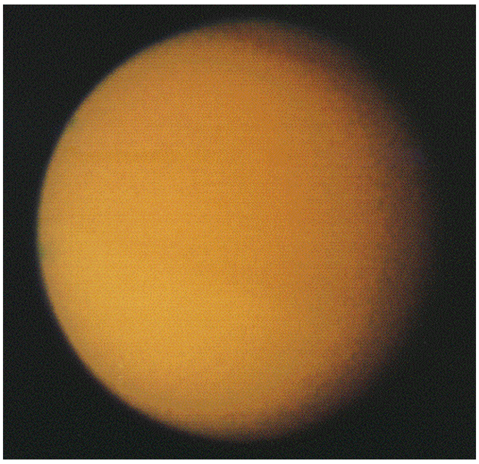

Figure 1.5: This Voyager 2 photo shows that Titan's surface is completely obscured by layers of haze in visible light. Image credit: NASA

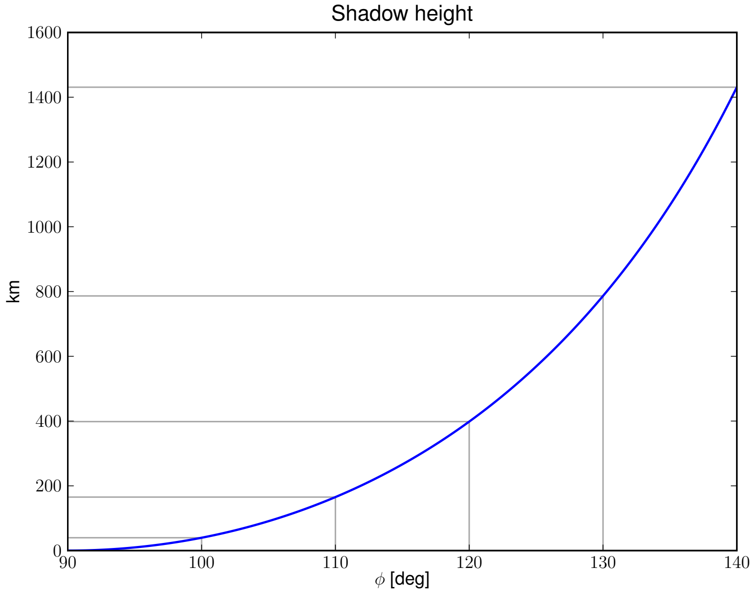

Figure 1.6: Dependence of shadow height on zenith angle.

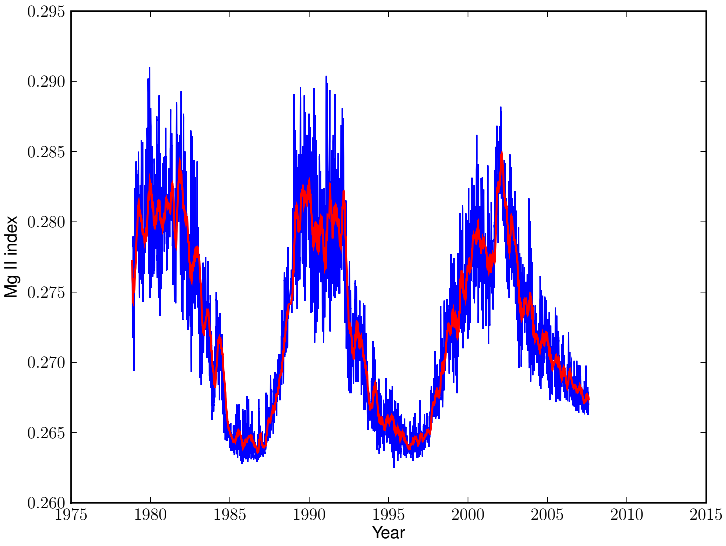

Figure 1.7: Time series of the daily NOAA Mg II solar activity index (Viereck and Puga, 1999) with its 60-day running average (red line). This index is a good proxy of solar EUV output, which drives photochemistry. The peaks of solar cycles 21 to 23 are clearly visible.

the h and k lines of the Mg II (magnesium) emission feature at 280 nm. These emission lines are strongly dependent on chromospheric activity and are therefore a good indicator of Solar ultraviolet and extreme ultraviolet emissions.

Fig. 1.7 shows the daily time series of this index with a running 60-day average. As one can see, the Cassini mission measurements fall on the subsiding part of Solar cycle 23, with Solar output steadily decreasing during the time period starting in 2004. In 2009, the Solar cycle 24 had yet to pick up, as the Solar minimum at the end of cycle 23 has proven to be unusually protracted.

2–D and 3–D structure of constituents

Even the early Pioneer images of Titan showed brightness differences between the SH and NH, due to the effect of the subsolar latitude on chemistry via photolysis and via advection through the induced Hadley circulation from summer to winter hemisphere. That the gases also exhibited meridional gradients in the stratosphere was determined from Voyager data (Coustenis and Bezard, 1995) and some pre-Cassini modeling studies looked into this seasonal effect on chemical composition in the stratosphere (Lebonnois *et al.*, 2001), assuming idealized winds for the region below 500 km altitude.

Both models and observations from Voyager show that many species undergo enrichment on the winter hemisphere in the descending branch of the Hadley circulation. The more detailed Cassini measurements supported these conclusions from Voyager data (Coustenis *et al.*, 2007), finding strong concentration gradients between the equator and NP, but weak gradients on the SH.

1.3 The Cassini-Huygens mission and other available observations

The first close-up photos of Titan were made by the Pioneer probes. Pioneer 11 flew by Titan in 1979, but its visible-light camera could not penetrate the haze layer. The next mission to Saturn were the Voyager probes, with Voyager 1 reaching Titan in 1980. Again, the haze proved an obstacle, therefore, Voyager 2 did not examine the moon more closely, as it was apparent the instrumentation of the probes could not penetrate the haze. However, Voyager 1 discovered the existence of haze layers, but could not discern surface detail. It also made measurements with its UVS and IRIS sensors, the latter finding that polar enrichment of species existed in the NH, winter stratosphere (Coustenis and Bezard, 1995).

Interpretation of the INMS measurements is difficult because there are so few of them for each species, distributed mainly over the NH. Cui *et al.*

(2008) have conducted a comprehensive analysis of all available Cassini INMS data. For meridional and zonal variation however, their findings were somewhat inconclusive, perhaps because of their approach of extrapolating all VMRs to a common altitude via an assumed power law. While the authors did find signs of polar depletion at the NP for some species like C_4H_2, they did not provide absolute values. Furthermore, they rejected zonal variability on the basis of a statistical significance test. Later (J. Cui, pers. comm.) it was acknowledged that signficant zonal variations might exist if analyzed in terms of Local Solar Time (LST). An alternative analysis of the Cassini INMS data will be presented in conjunction with the Control run results in section 3.1.

1.4 Modeling efforts and open scientific questions

Different chemistry schemes have been proposed for Titan's atmosphere, starting with the work by Carl Sagan in the 1970's and Yuk Yung's seminal 1984 paper. The differences lie in such things as whether oxygen is included as a chemical element, whether ions are part of the scheme, and the extent to which parameter tuning has influenced the selection of reaction rates. Also, the complete chemistry models may contain different temperature and eddy diffusion profiles, microphysics, and species that are fixed at the surface or top of the model (or, where there is no fixing at the top, escape fluxes may have been described). However, the single most important factor influencing model results may simply be if a given reaction has been included in the scheme or not. In that sense creating a chemistry scheme is somewhat dangerous, because, as with all other models, the assumptions that go into its creation influence the results and may lead to somewhat circular reasoning. If for example one experimenter includes many ion-neutral reactions in his scheme, he may draw from the model results the conclusion that ions are a major factor for neutral species concentrations, whereas another experimenter may leave ions almost completely out of his scheme and will therefore not find an important influence on neutrals.

Also, tuning reaction rates very far from laboratory measurements may be justified in that many of these measurements exhibit significant uncertainty and often need to be extrapolated to lower temperatures, which increases the error. An uncertainty of a factor of 10 is not uncommon for reaction rates for Titan as Hebrard *et al.* (2007) demonstrated. Still, there are different approaches regarding tuning, with some modelers resorting to a tuning of eddy diffusion profiles and microphysics, and others using more aggressive reaction rate-based tuning. As with all tuning, given the uncertainty of the Cassini INMS measurements, the possibility exists for “tuning away” differences between the model and observations that are actually scientifically significant and highlight an issue with data retrieval from observational data, rather than a weakness of the model.

First models of Titan’s chemistry were more qualitative, e.g. Strobel (1982) realized that the presence of molecular nitrogen means that acetylene is produced at high altitudes due to the quenching of $^1CH_2$ (excited methylene) by N_2.

1–D models

The earliest attempt to model Titan’s photochemistry was undertaken by Yung *et al.* (1984), based on the earlier Strobel study. The eddy diffusion profile adopted in that study caused sharp bends in many species’ VMRs at around 600 km altitude that were later felt to be somewhat unrealistic.

In 1995, Toublanc *et al.* developed a model where the photolysis coefficients were computed with a Monte Carlo scheme, thus allowing the inclusion of scattering and bringing improvements in the stratosphere. But where e.g. the Yung *et al.* model had predicted C_2N_2 100 times larger than measurements, their value was extremely small, so the improvement was only partial.

Lara *et al.* (1996) constructed a chemistry model that pointed to eddy diffusion as a major issue, because they found it difficult to find an eddy diffusion coefficient that worked similarly well for hydrocarbons and nitriles. CH_3C_2H and HC_3N proved to be particularly problematic species.

In 2004, Wilson and Atreya published another 1–D chemistry model of Titan’s atmosphere, which was based on the idea that ions had an important role in determining neutral species compositions. Other authors (Lavvas *et al.*, 2008a and b) disagreed and formulated a scheme almost without ions.

Liang *et al.* (2007a and b) used a photochemistry model to study the formation of haze particles, which they theorized to begin their life with the condensation of C_6H_2 and adsorption of meteoritic dust, as well as the heavier hydrocarbons and nitriles, and the effect of photochemistry on the $^{14}N/^{15}N$ ratio of nitrogen isotopes. (The paper by Lavvas *et al.*, 2009 claims that in fact there according to HASI data—as opposed to UVIS which Liang *et al.* used for their study—there is a temperature *maximum* at the height of the detached haze layer of 520 km, ruling out this condensation hypothesis. They attribute this maximum to absorption of Solar radiation by the haze and propose that the detached haze layer—if it is indeed not just an optical illusion due to coagulation at that height—is due to the transition from spherical to fractal haze particles at that height.)

Krasnopolsky (2009) presents an updated and tuned version of the Lavvas *et al.* scheme, which was the backbone for the chemistry scheme used in this study. In many respects his model is a major improvement over the Lavvas *et al.* results, especially for heights above 900 km or so, but this comes at the price of some tuning that has gone into the model in terms of adjusted reaction rates, which hopefully laboratory measurements will confirm. However, both the Lavvas *et al.* and Krasnopolsky studies clearly show that some amount of tuning, whether its is of microphysics, reaction rates, or the introduction of other loss rates are essential for reproducing measurements.

An important refinement of the Krasnopolsky scheme over Lavvas *et al.* is the inclusion of updated reaction rates for C_2, as previous experiments with the model in this study have also shown C_2 VMR to be crucial for many hydrocarbons, with C_2 production in the Lavvas *et al.* scheme generally being too low. The rather striking C_6C_6 profile in the Krasnopolsky paper, which is almost perfectly in agreement with observations, is one feature of his model which could not be reproduced here.

2–D models

Lebonnois and Toublanc (1999) considered latitudinal variations in composition based on column models at various altitudes, with photolysis coefficients that took haze and the three-dimensionality properly into account. However, the found they could not reproduce the observed stratospheric NP enrichment and speculated that a 2–D or 3–D model would be required to do that.

Rannou *et al.* (2004) presented a coupled dynamics-microphysics model to explain cloud and haze formation in Titan's atmosphere. Results from this model have also been made public in the form of a database (Rannou *et al.*, 2005).

3–D models

An early GCM for Titan's atmosphere was presented in Hourdin *et al.*, 1995. It was characterized by an extremely long spin-up time of decades, in fact the simulation presented in the paper did not bring the model to a fully spun up state. This was explained to be the consequence of very low vertical momentum transport.

More recent GCMs for the tropo- and stratosphere include the one developed by Tokano (1999) and Newman (Richardson *et al.*, 2007).

Dynamical modeling of the thermosphere is made more complicated by effects such as ion drag and non-LTE (Yelle, 1991) effects. But in addition to these difficulties, which also exist for Earth's thermosphere, the large vertical extent and curvature of the atmosphere must be taken into account.

Mueller-Wodarg (2000, 2002, 2003) constructed the premier model of this kind and used it to make predictions about the distribution of long-lived species such as methane in the thermosphere, based on a strong effect of meridional overturning in his model.

An updated version of his model (Mueller-Wodarg *et al.*, 2008) endeavors to explain the observed low methane VMR variations in a purely dynamical way.

Bell (2008) adapted the GITM model for use as a Titan (T-GITM) and Mars model, and includes a very simple chemistry scheme in T-GITM because the radiatively important HCN cannot simply be assumed to be infinitely long-lived but has to have chemical sources and sinks. Knowing that measurements of methane VMR by Cassini showed much lower spatial variation than predicted by the Mueller-Wodarg model, Bell assumes that an additional loss mechanism for methane must exist, which he identifies as haze. Bell also studied the effect of solar variability on general circulation, which results are used as model input fields in section 4.1.

Friedson *et al.* (2009) introduced a coupled dynamical-radiative-chemical model for the lowest 400 km of Titan's atmosphere, which was derived from NCAR's CAM3 GCM. However, despite its complexity it fails to reproduce the observed enrichment of e.g. HCN in the winter stratosphere satisfactorily.

Motivation for this thesis

Given the previous modeling work about Titan's chemistry that has been conducted and the Cassini INMS data that has recently become available, the question is whether the proposed chemistry schemes, combined with wind fields as predicted by GCMs, can reproduce the spatio-temporal distributions of trace gases in Titan's thermosphere. As photolysis is highly important there (and relatively well understood in terms of modeling, e.g. the photolysis cross-sections) and the winds are weak, and also the horizontal (and even vertical) temperature gradients are small, one would expect models do be more succesful there than e.g. in the stratosphere where haze and microphysics can alter the tracer distributions considerably. At the same time, it is clear that the Cassini measurements have inherent difficulties themselves, arriving at concentrations in the free atmosphere based on measurements in the INMS spectrometer chamber being difficult because there are uncertainties about the wall chemistry. Therefore, the first step is to compare the model to measurements and try to identify the problems in the model (such as reaction rate coefficients) and the measurements (such as insufficient compensation for wall chemistry), which is done in chapter 3.

Next, the influence of the Solar cycle is considered (chapter 4), because the Cassini measurements cover mainly average-to-minimum Solar activity. Therefore, it is particularly of interest to compare the changes for Solar minimum conditions to Solar average. The main problem for those conditions is that the rate coefficients are even less certain for temperatures below 150 K, so the Solar activity runs should be considered more as sensitivity experiments than predictions.

Finally, the impact of short-term temperature fluctuations caused by upward-propagating gravitational tidal waves is studied (also chapter 4), which have been observed (in temperature) in Huygens descent measurements. It is conceivable that these fluctuations could be powerful enough to influence chemistry via the dependence of reaction rates on temperature.

Chapter 5 then provides a summary and outlook on further research possibilities.

The basic aim of these experiments is to find out to which extent 3–D chemistry models can reproduce the observed chemical species distributions and whether these models can be used as tools to aid interpretation of the very limited (both in time and space) Cassini INMS data.

Chapter 2

Model description

2.1 The MOZART Chemistry Transport Model

MOZART-2 (**M**odel of **Oz**one **a**nd **R**elated **T**racers; Horowitz *et al.*, 2003) is a chemistry transport model (CTM) developed in cooperation between the Atmospheric Chemistry Division (ACD) of the National Center for Atmospheric Research (NCAR), the Geophysical Fluid Dynamics Laboratory (GFDL) at the National and Oceanic and Atmospheric Administration (NOAA), the Max Planck Institute for Meteorology, and Princeton University. MOZART is being used in both research and forecasting, and is distinguished by its high performance through code generation by a preprocessor as well as the comparative ease with which the chemistry scheme and model resolution can be modified via the preprocessor input file. It can be used either on-line (i.e., coupled to a GCM) or off-line, that is, *not* coupled to a GCM, in which case data such as winds, temperatures, surface fluxes of heat and momentum, specific humidity, and surface pressure are read from a "dynamics file" that has typically been directly converted from GCM output files (but which can also be created by the user directly). These fields—which are provided at 3-hour intervals for Earth (and 24-hour intervals for Titan)—are then linearly interpolated to obtain current values for each time step.

First introduced in 1998 (Brasseur *et al.*, 1998), MOZART has undergone several upgrades, notably code changes such as a different advection scheme between v2 and v1, while the changes from v2 to v4 focused on refinements to the chemistry and inclusion of tropospheric aerosols. MOZART-3 is a separate model based on MOZART-2 that extends the vertical domain into the stratosphere and mesosphere (Kinnison *et al.*, 2007). Typical resolution parameters for MOZART when applied to Earth are a horizontal resolution of 2.8°, 34 levels (with the model top at around 40 km altitude), and a time step of 20 minutes (Horowitz

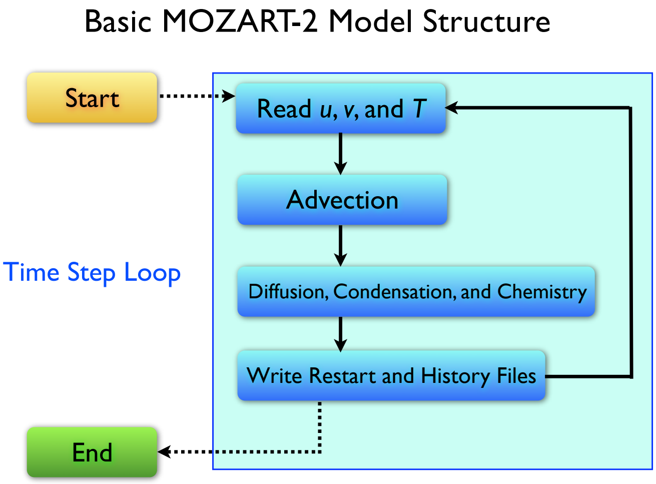
Basic MOZART-2 Model Structure
Start
Read *u*, *v*, and *T*
Advection
Time Step Loop
Diffusion, Condensation, and Chemistry
Write Restart and History Files
End

Figure 2.1: Basic structure of the MOZART Chemistry Transport Model (CTM).

et al., 2003).

In addition to the normal single-CPU mode, MOZART can also be run on multiple CPUs/cores simultaneously, either using OpenMP threading, or separate processes using the Message Passing Interface (MPI), or a hybrid mode where both methods are used—typically MPI to spread the work by assigning certain ranges of latitude circles to the available MPI processes, which then further subdivide the workload by splitting each latitude circle according to the number of OpenMP threads. As a 3–D chemistry transport model can be thought of as a collection of 1–D (i.e., column) models linked to each other at each time step by advection, this distribution of computation is quite effective, because most of the computations can be done for each column separately (e.g., chemistry and vertical diffusion) and only for doing advection results from the individual columns need to be gathered.

The main loop

The model computes a new volume mixing ratio (VMR) for species i at time step t_n using (eq. 1 from Brasseur et al., 1998)

$$q_i(t_{n+1}) = D \cdot K \cdot C \cdot A \;\; q_i(t_n)$$

where A, C, K, and D are the operators for advection, chemistry, convection, and diffusion, respectively. Implicit and explicit solvers are available, such as fully-implicit backward Euler with Newton-Raphson iteration and an implicit

Runge-Kutta solver. Solving all species with the backward Euler method is recommended for complex, possibly unstable chemistry schemes such as Titan's atmospheric chemistry (S. Walters, MOZART documentation).

When started (Fig. 2.1), MOZART first reads initial values for the concentrations, either from the initial value file, or in the case of a restart run, from a history file. Zonal and meridional wind as well as temperature fields are read from the dynamics files and interpolated for the current time step.

The time loop first performs Lin and Rood (1997) advection, where the vertical mass flux is computed from the u and v wind components and the continuity equation. This advection scheme is slightly diffusive, so that adding further horizontal diffusion is not necessary.

Next, molecular and eddy diffusion are applied explicitly, also species over their saturation vapor pressure condense out as in the Lavvas *et al.* (2008) scheme. Boundary conditions for CH_4 and H_2 are also adjusted here, and the dissociation by galactic cosmic rays (GCRs) in the lower atmosphere is added.

The chemistry routines come after that, where first the given J table is used with the computed zenith angle for each grid point to get the photolysis rates. Then the iterative solver uses the photo rates and other reaction rates to compute the concentrations at the next time step.

Finally, concentrations and production and loss rates are written to the history file and a new restart file is created if the given intervals for history and restart file creation have been reached. Then the loop proceeds to the next time step.

2.2 The basic MOZART setup for Titan

While the latest tropospheric MOZART version for Earth is version 4, in this work MOZART-2 has been used, because the chemistry solver—which is the primary component of MOZART of interest here—has not changed between versions 2 and 4, while the other improvements only apply to Earth.

Adapting MOZART from its Earth configuration for use as a Titan model involved disabling processes such as wet and dry deposition, emission of NO_x by lightning and airplanes, or cloud effects on photolysis that do not exist on Titan—or at least not in the mesosphere and thermosphere (see preceding part). The vertical grid was changed to cover about the lowest 1,200 km of Titan's atmosphere, the gas constants were updated according to the average chemical composition of Titan with its atmosphere of mostly molecular nitrogen, molecular diffusion and condensation of several species were added follwing McEwan and Philips (1975) as well as Lavvas *et al.* (2008), and the photolysis routine was updated to include photolysis above the night side of Titan.

A new table with photolysis coefficients for each reaction, height, and Solar zenith angle was computed and user-defined reactions added to the MOZART code where the standard expressions for reaction rates in the MOZART preprocessor were not sufficient. New dynamics and initial value files in NetCDF format also had to be created based on wind and temperature fields from existing Titan general circulation models (GCMs) as described later.

Radiation

One of the tables that MOZART relies upon is the photolysis table, which for each species gives the photolysis rate as a function of zenith angle and altitude. As for the Earth configuration, the Titan model uses such a table of pre-computed coefficients based on global-mean species profiles from previous model runs.

The solar spectrum (Woods and Rottman, 2002) used for the J computations is based on UARS SOLSTICE measurements, which observed the Solar UV spectrum from 1991 to 2005 (with its followup instrument being SORCE), as well as a CU LASP rocket measurement from 1994 and data from YOHKOH, GOES, and TIMED. It provides solar irradiance in photons per second per square centimeter between 1 and 420 nm for Solar minimum along with factors for 27-day and Solar cycle variabiliy for each 1 nm wavelength bin (see Fig. 2.2). Fig. 2.3 shows that radiation with a wavelength below about 100 nm is absorbed mainly in the thermosphere, where it drives production of chemical species by photolysis of methane and nitrogen.

The photolysis coefficients were computed under the assumption that absorption occurs only by atmospheric gases, not haze—a reasonable simplification for the thermosphere, except for extremely large zenith angles. The resulting J's for Solar average conditions (Fig. 2.4) show that photolysis is very dominant in the thermosphere above about 800 km height or so for many species, with J's that are vertically almost constant except for molecular nitrogen, which is really only significantly photolyized above 1,000 km heigt due to its absorption cross section being mainly receptive to very short-wavelenth UV photons.

Sensitivity of the J's to the Solar cycle (Fig. 2.5) is between about 10 and 60% for most species. As shorter wavelengths are absorbed more strongly, the highest sensitivity is at the top, because Solar output changes most in that spectral region (Fig. 2.2). At lower altitudes, sensitivity in the J's mirrors Solar variability at longer wavelengths.

Because the vertical extent of Titan's atmosphere is so enormous in relation to the moon's radius, photolysis at zenith angles larger than 90°has to be included in the model. Even if the J's for such large zenith angles become very small, because the light travels through lower and lower layers of the atmosphere, it still

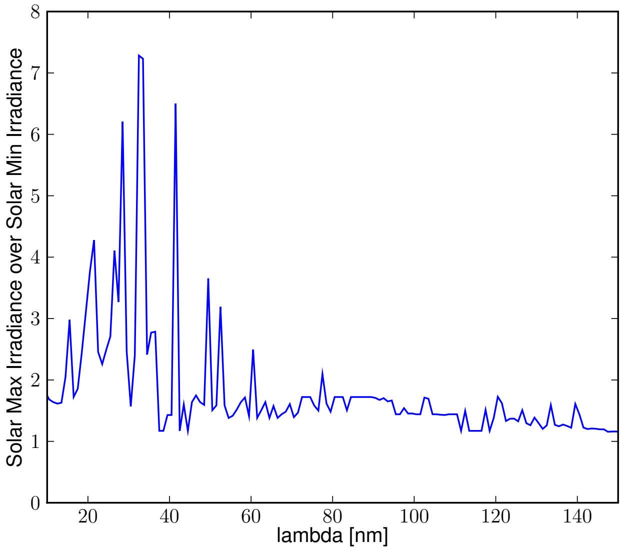

Figure 2.2: Variability of the Solar spectrum between Solar maximum and Solar minimum, i.e. Solar maximum irradiance divided by Solar minimum irradiance. The strongest variability exists in the most energetic part of extreme ultraviolet (i.e., wavelengths below about 70 nm), while the variation for larger wavelengths is below a factor of two.

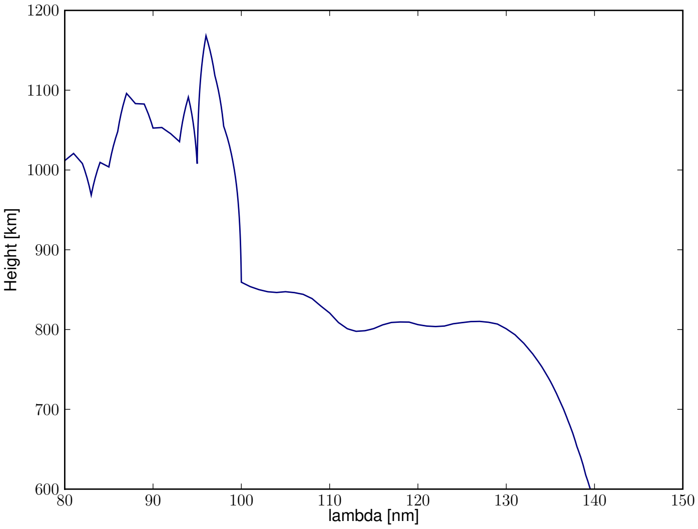

Figure 2.3: Level of maximum radiation absorption (optical depth $\tau = 1$) in Titan's atmosphere as a function of wavelength.

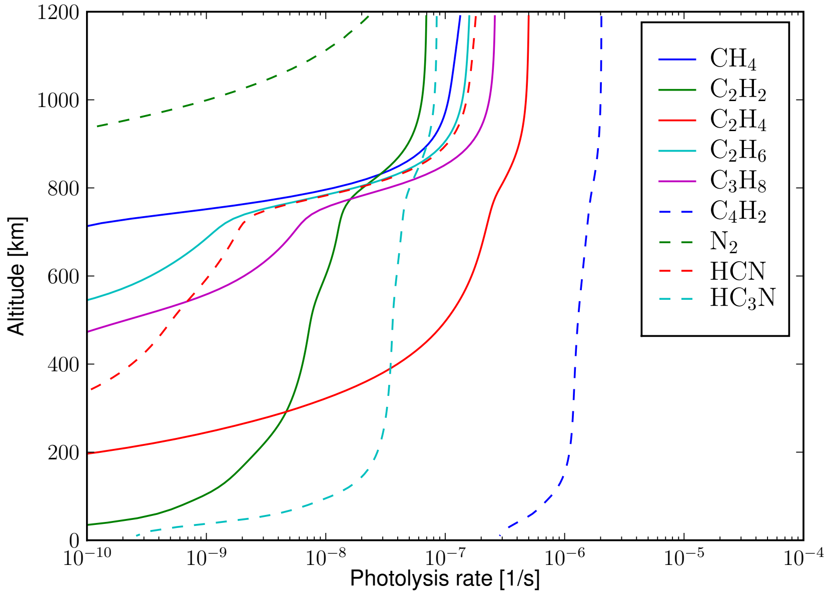

Figure 2.4: Photolysis coefficients for Solar average conditions for selected species and a zenith angle of 30°.

makes a difference for the chemistry whether there is very minor photochemistry going on over Titan's night side or whether it is completely turned off. For this model, J's were tabulated for up to 135°zenith angle, and for zenith angles above that it was assumed that no photolysis takes place. Fig. 2.6 shows how the photolysis coefficients wrap around Titan to zenith angle far above 90°: C_2H_2 photolysis is comparatively uniform wherever there is Sun, C_3H_8 exhibits a stronger drop in the night-side J, while methane photolysis could be assumed to be confined to zenith angles $< 90°$without making a big error.

Dynamics

Wind fields were obtained from the TitanWRF GCM (Richardson *et al.*, 2007) for the tropo- and stratosphere and from T-GITM (Bell, 2008) for the upper mesosphere and thermosphere. The Bell GCM incorporates the observed super-rotation (Achterberg *et al.*, 2008) as its lower boundary condition, so the two models have closely matching winds at their interfaces, and those interfaces are close enough together that only minimal column interpolation between the model fields is required. The sponge levels from TitanWRF are neglected, because they are damped artificially. As shown in Fig. 2.7, the interface between the two model domains is at around 500 km height and no additional levels had to be

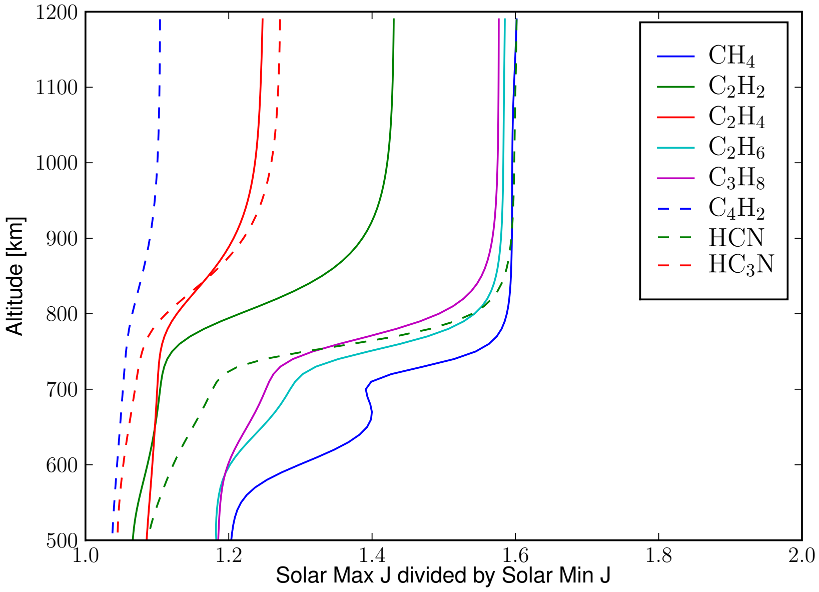

Figure 2.5: Factor between Solar max and Solar min photolysis coefficients for selected species and a zenith angle of 30°.

introduced between existing model levels, so that interpolation was confined to the sponge layer.

As the main region of interest in this study is the thermosphere, the winds obtained from T-GITM are of primary importance. The slower circulation in the tropo- and stratosphere still allows some vertical and horizontal transport to take place, which makes the model more realistic than if e.g. a lower boundary at 600 km height had been assumed, because the stratosphere can act as a chemical sink for the heavier species such as benzene and diacetylene.

T-GITM has evolved from the Global Ionosphere–Thermosphere Model (GITM) model (Ridley *et al.*, 2006). Some of the distinguishing feaures of GITM are that it is non-hydrostatic, that advection and chemistry are solved explicitly (necessitating a relatively small time step of only a few seconds), that the grid can be non-uniformly spaced in latitude and altitude, and finally that it uses altitude instead of atmospheric pressure as its vertical coordinate.

The very basic chemistry scheme chosen for T-GITM is necessary to ensure that HCN is both produced and destroyed in the model. I.e., as opposed to methane and molecular nitrogen, where meaningful results can be obtained just by using diffusion and advection, the chemistry of HCN is non-negligible, so a purely advective model would fail. HCN feeds back into the dynamics of the GCM through its rotational spectral lines in IR, which cool the thermosphere.

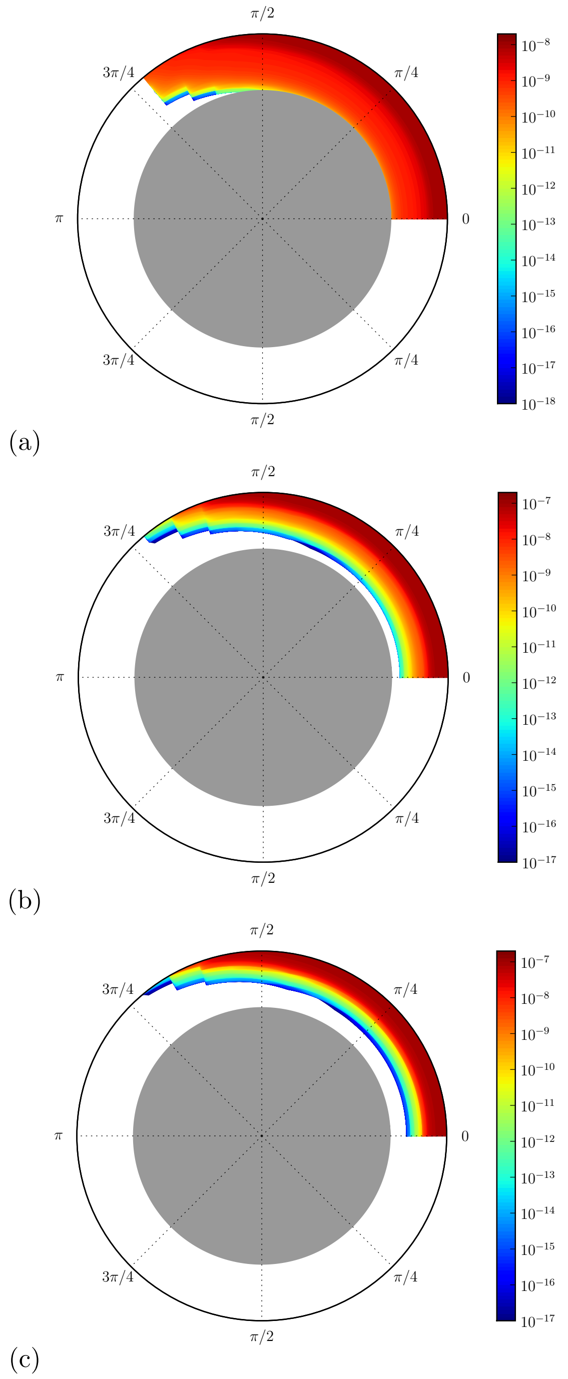

Figure 2.6: Photolysis coefficients around Titan (shown in gray) for (a) C_2H_2, (b) C_3H_8, and (c) CH_4, with the Solar rays coming from the right (3 o'clock) side of the plot and the atmosphere being shown between the surface and 1,200 km altitude.

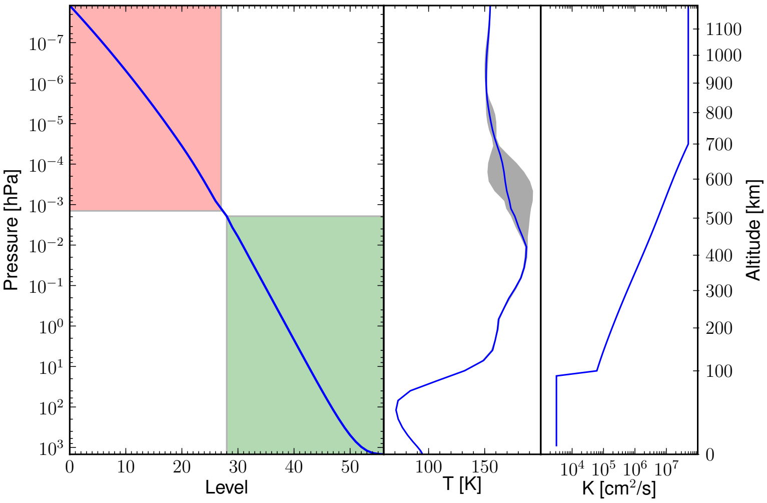

Figure 2.7: Combined grid with pressure levels from the T-GITM (red area) and TitanWRF (green area) GCMs (left panel), global-average temperature profile with shaded range of minima and maxima (center panel), and eddy-diffusion profile used by MOZART.

Therefore, a GCM of the thermosphere in general needs to incorporate at least as much chemistry that the HCN concentrations are valid. (On the other hand, both in MOZART and T-GITM HCN concentrations do not vary very strongly globally, so it remains to be seen whether a simpler approach, e.g. a prescribed HCN VMR based on Solar zenith angle, could not also yield acceptable results in the absence of a full chemistry scheme.) T-GITM only allows a species to deplete by a maximum 25% during a time step, otherwise multiple chemistry time steps are performed.

The continuity equation for T-GITM is

$$\frac{\partial N_s}{\partial t} + N_s \nabla \cdot \mathbf{u} + \mathbf{u} \cdot \nabla N_s = 0$$

where $\mathbf{u}$ is neutral velocity, t is time, and the N_s are the species number densities. The momentum and energy equations are, respectively:

$$\frac{\partial \mathbf{u}}{\partial t} + \mathbf{u} \cdot \nabla \mathbf{u} + \nabla T + \frac{T}{\rho} \nabla \rho = 0$$

and

$$\frac{\partial T}{\partial t} + \mathbf{u} \cdot \nabla T + (\gamma - 1) T \nabla \cdot \mathbf{u} = 0$$

where γ is the ratio of specific heats and T is the normalized neutral temperature, defined as the fraction of total neutral pressure p and density ρ: $T = p/\rho$.

Instead of the number density of each species, the logarithm of number density is used: $\mathcal{N}_s = ln(N_s)$. Some possible limitations—or at least simplifications—of the T-GITM Titan model include the assumption of LTE (local thermodynamic equilibrium) and that HCN cooling is computed on a plane-parallel instead of spherical grid.

The combined temperature profile (Fig. 2.7) can be compared to HASI measurements (Fulchignoni *et al.*, 2005). In those measurements, strong temperature fluctuations between about 1,000 and 500 km altitude were apparent, presumably caused by upward-propagating gravitational tidal waves, and also the average temperature in that range was up to 30 K higher than assumed in the Titan engineering model. This is also true for T-GITM, although T-GITM does exhibit a certain amount of variability between 500 and 700 km altitude. But if the measurements give a fairly accurate idea of average conditions, the atmosphere should be closer to isothermal between 500 and 1,000 km height than model results suggest.

The wind fields (Fig. 2.9) show two Hadley cells, one in the tropo- and stratosphere, and the other one above about 700 km height. In the TEM view (center panel in Fig. 2.9), a smaller cell above 1,000 km on the SH is also apparent. The profile (Fig. 2.10) for TEM vertical wind, w^*, shows that there is a region of probably exaggerated vertical transport in the model interpolation region between about 400 and 600 km altitude, caused by a zone of very strong (in excess of 25 m/s) northward transport at the T-GITM bottom layers. Interpolation creates strongly compressed streamfunction isolines around 600 km height. Therefore, species with a strong dependence on vertical wind will probably exhbibit an overly large influence from advection in that region. This is also a vertical range of Titan's atmosphere where measurements are scarce, so it is difficult to say whether the strong northward advection is realistic.

The zonal wind field (Fig. 2.8) is dominated by two westerly jets in the NH, while in the SH at about 350 km altitude a weak easterly jet is visible. However, generally the zonal circulation on Titan is almost exclusively eastward. Above about 700 km altitude, the jet shows relatively little variation with height. While the jet is still weaker than what is inferred from observations, it is approximately in the correct range (measuremenents put peak velocity at around 190 m/s; see Achterberg *et al.*, 2008).

Eddy and molecular diffusion

Estimates of the eddy diffusion coefficient have generally converged during recent years, and a height-independent eddy diffusion coefficient is normally assumed above the mesopause ($\approx$ 600 km height). The eddy diffusion coefficient used

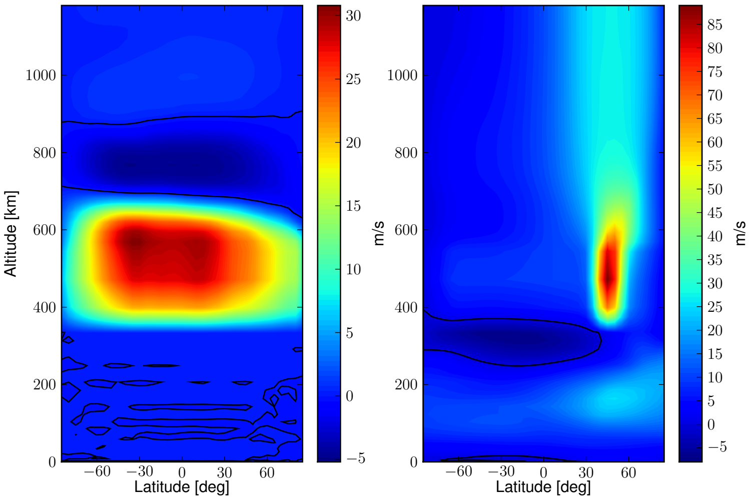

Figure 2.8: Zonal-average, time-average meridional wind v (left panel) and zonal wind u (right panel).

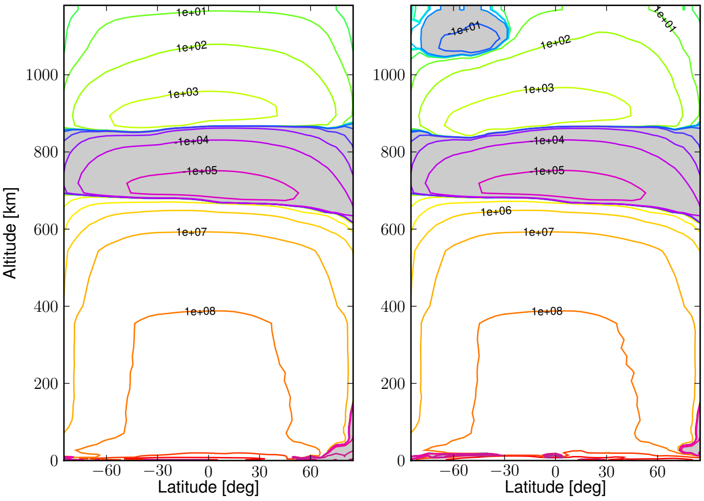

Figure 2.9: Zonal average (left panel) and transformed Eulerian Mean (TEM) circulation (right panel) in kg/s.

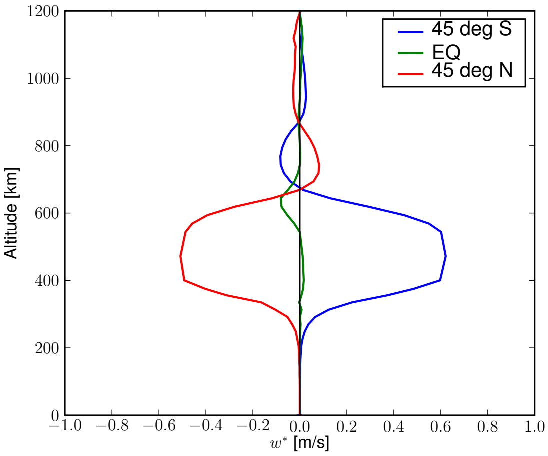

Figure 2.10: Time-average Transformed Eulerian Mean (TEM) vertical wind w^* in mm/s at 45°N/ S and at the equator.

here, 5×10^7 cm^2/s, for the thermosphere is that from Mueller-Wodarg (2003). The homopause, i.e. the height above which molecular diffusion becomes more important than eddy diffusion and therefore mean molecular atmospheric weight becomes height-dependent, is located at about 800 km.

Eddy diffusion is implemented according to the equation given in Banks and Kockarts (1973), even though other authors (Yelle *et al.*, 2006) have pointed out that eddy diffusion based on number density flux balance (as in the Banks and Kockarts formulation) instead of mass flux balance is not quite correct. However, since the Banks and Kockarts formulation is widely used in the other Titan chemistry models, it was deemed advantageous for comparison to use the same, and also because the error in the Banks and Kockarts equation is probably not very significant for this study. McEwan and Phillips (1975) provide a convenient formulation that combines eddy and molecular diffusion (their eq. 4.3)

$$\frac{\partial}{\partial z}([i]V_i) = -(D_i + K)\left[\frac{\partial [i]}{\partial z} + \frac{[i]}{T}\frac{\partial T}{\partial z}\right] - \left(\frac{D_i}{H_i} + \frac{K}{H_{\mathrm{av}}}\right)[i]$$

where V_i is the mean vertical velocity caused by diffusion, $[i]$ is the number density of species i, D_i is the molecular diffusion coefficient, K the eddy diffusion coefficient, T absolute temperature, H_i the scale height of species i, and H_{av} the local average scale height for the gas mixture. The left-hand side of the equation is basically the divergence, if $(\partial/\partial x)V_i[i]$ and $(\partial/\partial y)V_i[i]$ are so small to be negligible.

Diffusive lifetime is defined as (Murray and Phillips, 1975) $\tau = \frac{H}{D^2}$, where H is the scale height and D the diffusion coefficient. The MOZART time step is limited (according to the CFL criterion) to τ^{-1}, i.e. the time constant of molecular diffusion at the top levels, which depends on their absolute height and spacing. A higher top or more closely spaced levels there would therefore necessitate a smaller time step. In practice, MOZART runs have been conducted with either a 600 s time step (for the coarser Mueller-Wodarg-based grid) or 200 s (for the Bell grid).

Horizontal diffusion is generally very small on Titan because of the weak horizontal gradients (Mueller-Wodarg, 2003), but the Lin and Rood (1997) advection routine adds some slight horizontal diffusion of its own to improve numerical stability.

Chemistry scheme

The chemistry scheme is a combination of the Krasnopolsky (2009), Lavvas *et al.* (2008), and Wilson and Atreya (2004) chemistries, with some additional tuning to improve model performance in the thermosphere. The scheme includes 77 solution species (Table 2.1), two of which are ions, and 224 reactions, 40 of which are photolysis reactions. (Rate coefficients are provided in Appendix A).

Absorption cross sections and quantum yields for photolysis reactions are quite similar in the various available models, and more or less the same references are used. These measurements usually date from the 1970s to 1990s and have often been performed at higher temperatures. Generally, the data for the lowest available temperature is used without inter- or extrapolation. Temperature and pressure dependence of photolysis coefficients is neglected.

Rate coefficients differ between models, as sometimes several observations are available, though not necessarily for Titan-like conditions. It is then up to the experimenter to chose the reaction rate that seems most applicable or produces results that are most in agreement with Cassini or Voyager observations. Often, additional tuning of rate constants is required and may signify the need for lab experiments to back the validity of this tuning up experimentally. In some cases, e.g. the reactions involving C_2 (Canosa *et al.*, 2007), reaction rates have been measured specifically for the use in Titan chemistry models, as it was apparent that previous data was unsuitable and produced unrealistic results in models. The effects of rate coefficient uncertainties in chemistry models have been explored in Hebrard *et al.*, 2007. In a later paper (Dobrijevic *et al.*, 2009), photolysis reactions were included in the analysis to compare different approaches for finding the most important chemical reactions in the scheme and to determine the sensitivity of species to errors in reaction rates.

Hydrogen and hydrocarbons	Nitriles	Charged particles
H, H_2, C, CH, $^1CH_2$, $^3CH_2$, CH_3, CH_4, C_2, C_2H, C_2H_2, C_2H_3, C_2H_4, C_2H_5, C_2H_6, C_3H_2, C_3H_3, CH_3C_2H, C_3H_4, C_3H_5, C_3H_6, C_3H_7, C_3H_8, C_4H, $^*C_4H_2$, C_4H_2, C_4H_3, C_4H_4, C_4H_5, C_4H_6, C_4H_8, C_4H_{10}, C_6H, C_6H_2, C_6H_4, C_6H_5, C_6H_6, C_7H_4, C_7H_8, C_8H_2, $C_{10}H_{10}$, $C_{12}H_{10}$	$N(^2D)$, N, NH, NH_2, NH_3, CN, HCN, N_2, H_2CN, N_2H, CH_2NH, N_2H_2, N_2H_3, CH_3NH_2, N_2H_4, C_2N, CHCN, CH_2CN, CH_3CN, C_2H_5N, C_3N, HC_3N, C_2N_2, C_2H_3CN, C_2H_5CN, C_4H_3N, C_4H_5N, C_5HN, HC_5N, C_4N_2, C_5H_5N	N^+, N_2^+, e

Table 2.1: Solution and fixed chemical species in the model.

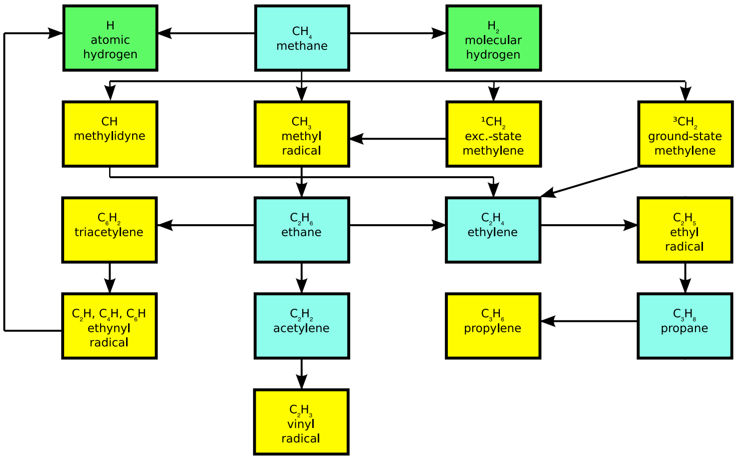
H atomic hydrogen
CH_4 methane
H_2 molecular hydrogen
CH methylidyne
CH_3 methyl radical
$^1CH_2$ exc.-state methylene
$^3CH_2$ ground-state methylene
C_6H_2 triacetylene
C_2H_6 ethane
C_2H_4 ethylene
C_2H_5 ethyl radical
C_2H, C_4H, C_6H ethynyl radical
C_2H_2 acetylene
C_3H_6 propylene
C_3H_8 propane
C_2H_3 vinyl radical

Figure 2.11: Highly simplified Titan chemistry scheme, showing how long-lived heavy species (blue) are produced from methane via shorter-lived intermediate species (yellow). Atomic and molecular hydrogen (green) take part in many reactions of the scheme, therefore their concentrations are crtitical to the overall stability of the chemistry scheme.

2.3 Discussion

In the previous sections, the basic setup of the MOZART model for these Titan simulations has been discussed. Several choices had to be made, including the chemistry scheme, the wind and temperature fields, the eddy diffusion coefficient, and the spatial resolution. The problem with constructing a chemistry model for Titan is generally that many of these choices are, if not entirely arbitrary, at least not particularly well-constrained by probe observations or lab measurements. Although there had been some recent progress (e.g. some indirect conclusions can be drawn from measured concentrations about the local wind field, and also differently derived eddy diffusion profiles are in reasonable agreement now), questions remain about the importance of ions and haze in the atmosphere, particularly the thermosphere. Also, the need to run the model in 3–D over several months and with a relatively short time step necessitates some simplifications, such as tabulated photolysis coefficients, a relatively coarse vertical resolution, at least compared to 1–D models, or the elimination of some reactions which more comprehensive 1–D models might include. Still, it is felt that the model introduced in this part of the thesis represents a good compromise between completeness and numerical performance.

Chapter 3

Model validation

3.1 Control experiment chemical distributions

This section concerns itself the 3–D distributions of chemical species in the unaltered (Control) run, which uses the GCM wind and temperature fields without modification, in comparison to INMS observations.

Global averages

A comparison between the global concentration averages from the Cui *et al.* (2008) paper and MOZART is shown in Table 3.1. The values generally conform to the goal of a deviation of at most factor 10, and for species which are much lower in the model than in measurements (esp. C_4H_2 and NH_3), it must be kept in mind those detections are not very certain in the INMS data and that wall reactions play a rôle in determining the measured concentrations (J. Cui, pers. comm.). It is therefore conceivable that the discrepancy for those species reflects a weakness in the INMS data retrieval procedure and not in the model.

Methane molecular hydrogen are of course artificially driven towards observed values, thus the correspondence with measurements is expected. C_2C_2 and C_2C_4 could not be retrieved separately in the Cui *et al.* study, instead they considered the composite species $0.75n(C_2C_2)+0.25n(C_2C_4)$. For easier comparison this is also done with the model concentrations here.

Heavy species generally exhibit large vertical gradients in the thermosphere, and the model resolution is comparatively coarse there (about 30 km). This means that the vertical uncertainty, coupled with the interpolation procedure, coupled with the low model resolution may impact the quality of model-retrieved values negatively. No sensitivity experiments with a higher vertical resolution were performed, but it should be kept in mind that the model resolution in this

Species	INMS VMR	MOZART VMR	Difference
CH_4	1.78×10^{-2}	2.63×10^{-2}	+47.79%
H_2	3.72×10^{-3}	3.41×10^{-3}	−8.35%
C_2H_2/C_2H_4	1.26×10^{-4}	1.10×10^{-4}	−12.91%
C_2H_6	4.05×10^{-5}	8.52×10^{-5}	+110.45%
CH_3C_2H	9.02×10^{-6}	1.42×10^{-6}	−84.23%
C_3H_8	$< 1.84 \times 10^{-6}$	4.16×10^{-6}	+126.21%
C_4H_2	4.92×10^{-6}	2.45×10^{-8}	−99.50%
C_4H_6	$< 2.63 \times 10^{-7}$	4.58×10^{-8}	−82.60%
C_6H_6	2.42×10^{-6}	9.23×10^{-9}	−99.62%
HC_3N	1.43×10^{-6}	4.09×10^{-7}	−71.40%
CH_3CN	1.51×10^{-6}	5.78×10^{-6}	+282.65%
C_2H_3CN	$< 4.00 \times 10^{-7}$	2.94×10^{-6}	+634.45%
C_2N_2	1.70×10^{-6}	1.41×10^{-6}	−17.15%
NH_3	3.48×10^{-5}	1.02×10^{-5}	−70.77%

Table 3.1: Global averages for a height of about 1,025 km from Cassini measurements and the MOZART Control experiment.

study (two levels per scale height) is comparatively low compared to 1–D models (some of which use levels spaced 1 km apart), and that this introduces a certain amount of additional uncertainty for species with large vertical gradients.

Lifetimes

Average chemical lifetimes (concentration divided by loss rate) are provided for selected species at 1,025 km altitude in Table 3.2. Lifetimes vary from the extremely long-lived, like HCN, to the very short-lived, like C_2. Of course lifetimes in the thermosphere mainly reflect photolytic destruction at that altitude—for example, methane has a lifetime of millions of years, if total column concentration is divided by column loss rate (as in Krasnopolsky 2009, Table 6), because photolytic destruction of methane is high in the thermosphere, but negligible below the thermosphere, where the most atmospheric mass is concentrated.

The relative importance of the various processes (chemistry, transport, and eddy and molecular diffusion) depending on height and Solar incidence angle can be shown in a plot when then respective lifetimes for each species at a given point are used (in the form of their logarithm) to arrive at a red-green-blue (RGB) color. The diffusion lifetime is computed as (McEwan and Philips, 1975)

$$\tau_{\text{diffusion}} = \frac{H^2}{D}$$

and the lifetime for vertical motion is

Species	Lifetime [s]
C_3H_8	7.8×10^{11}
HCN	5.3×10^{10}
HC_3N	2.9×10^{9}
C_4H_6	1.3×10^{9}
C_4H_2	1.4×10^{8}
C_2H_4	1.3×10^{8}
CH_4	5.2×10^{7}
C_2H_2	1.1×10^{7}
C_2H_6	5.9×10^{6}
$^3CH_2$	$1,244$
C_2	215
$^*C_4H_2$	0.1

Table 3.2: Global-average chemical lifetimes for selected species at 1,025 km altitude.

$$\tau_{\text{advection}} = \frac{H}{w^*}$$

where D is the diffusion coefficient and w^* is the Transformed Eulerian Mean (TEM) vertical wind. Shorter lifetimes mean the respective process is more important for determining the chemical concentration of a species, and therefore the respective color will be more or less dominant in the resulting image. If two processes are of roughly equal importance, the usual rules of additive color mixing apply.

Fig. 3.1a shows such a plot for acetyelene. Above 900 km, diffusion and chemistry are most important on the day side (pink color), while on the night side, diffusion is dominant (red), because photolysis is almost negligible. Between 600 and 800 km height, advection increases in importance (yellow), because the diffusion timescale grows longer and photochemistry is less active. Between 350 and 600 km, vertical transport is dominant (green), except close to the equator where there is little vertical motion. Below 300 km altitude, chemistry is the main determinant of species concentration.

Fig. 3.1b depicts the average lifetime profiles for the same species at the equator. The strength of advection fluctuates with height, and furthermore vertical motion at the EQ is somwhat diminished compared to the mid-latitudes.

Note that the advection and diffusion lifetime profiles even though they look relatively similar in the following figures, are actually slightly different because they depend on the scale height and diffusion coefficient for each species, which in turn vary based on the molar mass of the species. These differences would become even more apparent when comparing with a lighter species such as H_2.

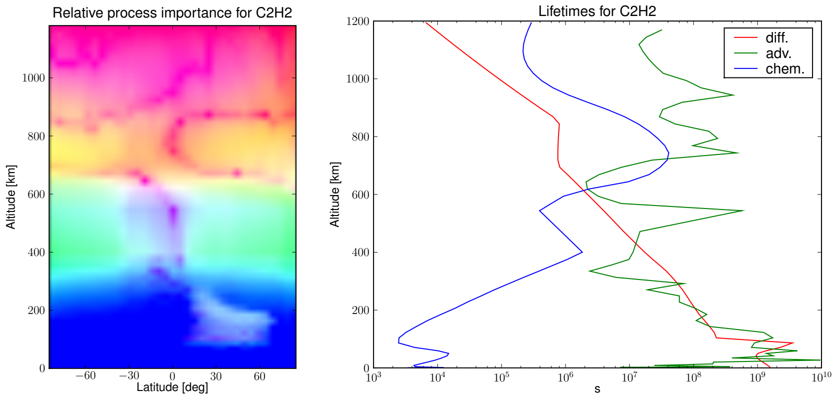

Figure 3.1: 2–D and 1–D views of acetylene lifetime: on the left, colored related to the logarithm of lifetime and on the right, average profiles at the equator. If the base-10 logarithms of the various lifetimes are l_1, l_2, and l_3, and m is their minimum value, then the colors in the first plot are computed as Red $= \max(0, 1 - 0.3(l_1 - m))$, and analogously for Green (with l_2) and Blue (with l_3).

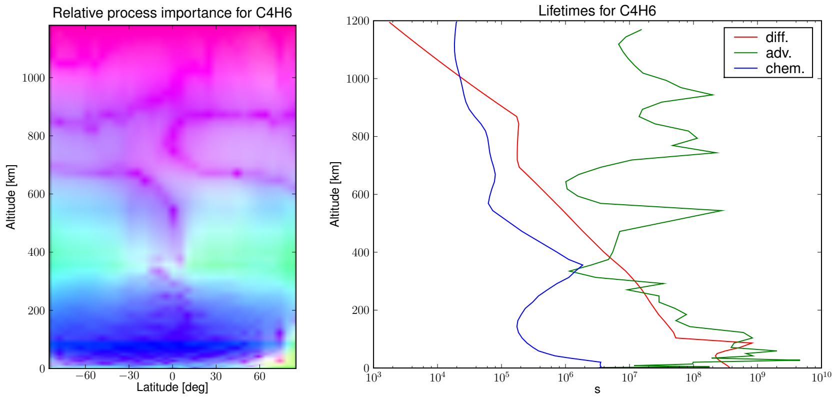

Figure 3.2: Like Fig. 3.1, but for C_4H_6.

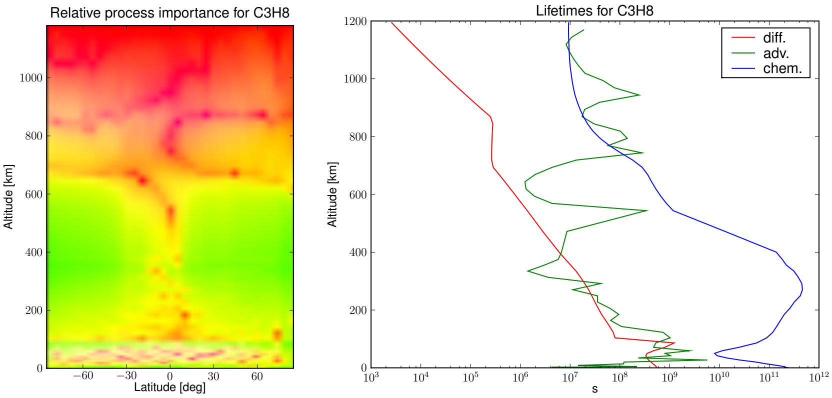

Figure 3.3: Like Fig. 3.1, but for C_3H_8.

In the case of C_4H_6 (Fig. 3.2), vertical motion is considerably less important than for C_2H_2. Instead, strong diffusion at the top and chemistry, at around 800 km altitude and predominantly in the SH, are the determining factors.

The final example is propane (Fig. 3.3), where the chemistry is very slow everwhere, so that molecular and eddy diffusion are almost solely responsible for observed VMRs in the thermosphere, while below 600 km height the species is mainly advected and diffused.

Zonal-mean and horizontal distributions

Figures 3.4 to 3.13 show production–loss rates, zonal averages, and horizontal fields for selected species.

Methane CH_4 (Fig. 3.4)

Methane shows depletion in the Southern (summer) hemisphere by photolysis as expected, but the variation in VMR is quite low (between 2.3 and 2.8% around 1,000 km height). Of course it must be kept in mind that this low concentration is achieved artificially by limiting methane concentration, but despite that the model produces (up to 1,050 km height or so) quite realistic methane distributions. As methane is the source of the hydrocarbons in the atmosphere, it is desirable to have a broadly correct methane distribution in the model. Advection does not influense methane concentration as strongly as in previous experiments with other thermospheric wind fields (Doege *et al.*, 2008)—the increased concentrations around the North Pole could be due to either downwelling or simply the lack of photolytic destruction. One therefore needs to look at the run without advection (see section 3.2) to ascertain that it is indeed mostly a chemical as opposed to dynamical effect.

Methyl radical CH_3(Fig. 3.5)

The methyl radical is very short-lived and depleted during the day by photolysis. At the same time, if its production by photolysis ceases there is a drop in concentration, as can been seen near the NP. This pattern is typical for such short-lived species.

Acetylene C_2H_2 (Fig. 3.6)

Acetylene does not show much diurnal variation in this experiment, but near the NP its VMR drops to 10% and less of the maximum value. Even though Acetylene is a long-lived species, northward transport by winds is insufficient to even out this equator-to-pole gradient.

Ethylene C_2H_4 (Fig. 3.7)

The global variation of ethylene is extremely low (about a factor of 2). There is a hint of striated maxima in the zonal-average view, with maxima at the SP, around $-30°$, and $+55°$.

Ethane C_2H_6 (Fig. 3.8)

Ethane exhibits strong vertical variation, with a zonal-mean maximum at around 750 km altitude at the SP and a broad photochemically-induced minimum above 1,000 km.

Propane C_3H_8 (Fig. 3.9)

Propane production peaks during the day ($C_2H_5 + CH_3 + M \rightarrow C_3H_8 + M$), while loss is dominated by photolytic destruction, creating C_3H_6, C_2H_4, and C_2H_6.

Diacetylene C_4H_2 (Fig. 3.10)

The horizontal distribution of diacetylene looks very similar to the of C_2H_2, as the main production reaction is $C_2H + C_2H_2 \rightarrow C_4H_2 + H$.

Benzene C_6H_6 (Fig. 3.11)

Benzene generally shows low variation, with the exception of the SP, where it is considerably higher in concentration. The large vertical gradient in the thermosphere is due to its high molecular mass and the resulting downward molecular diffusion.

Hydrogen Cyanide HCN and Cyanoacetylene HC_3N (Figures 3.12 and 3.13)

HCN and HC_3N are primarily distinguished in their vertical profiles: HC_3N is much heavier than HCN, therefore molecular diffusion causes its peak of concentration to be shifted downwards in comparison to HCN. Horzontally, HCN peaks in the southern middle latitudes, while HC_3N peaks at the SP.

Vertical structure of the diurnal cycle

The effect of the diurnal cycle, due to photolysis and advection caused by heating, can be visualized for each species when the amplitude and phase for the diurnal variation are plotted. What this means is that for each altitude-latitude point, the *maximum* VMR along the latitude circle is divided by the *mean* VMR along that latitude circle, then 1 is subtracted and the difference is expressed as percent. For the phase, first the peak concentration is found and the corresponding longitude is then transformed into Local Solar Time.

One complication for making that plots for the phase is that the scale wraps, i.e. 24 h is the same as 0 h. When using contours, this leads to an unsighly stacking of countour lines around midnight points. Therefore, colored rectangles were used here instead of contours, with each rectangle representing the phase at the point at its center.

As the longitudinal resolution of the model is comparative low, 1–D spline interpolation is used to determine the most likely location of the concentration maximum for each latitude and height. This spline-based retrieval has also been used for earlier investigations with this model (Doege *et al.*, 2008) and has proven to be a sucessful method to overcome the limitations of a low resolution in longitude. Since at model equilibrium the VMR pattern travels with the diurnal cycle around Titan without change, the high temporal resolution is essentially used to replace the lack of horizontal resolution, because at equilibrium longitude and time are simply related to each other, so that a shift in longitude corresponds to a shift in time and vice versa. Doege *et al.*, 2008 demonstrated that e.g. for methane, for which a previous modeling study existed (Mueller-Wodarg *et al.*, 2003), in which methane was advected as a passive tracer, time-averaged spline-based retrievals from this relatively low-resolution model are almost indistinguishable from higher-resolution runs that just use grid point-based averaging.

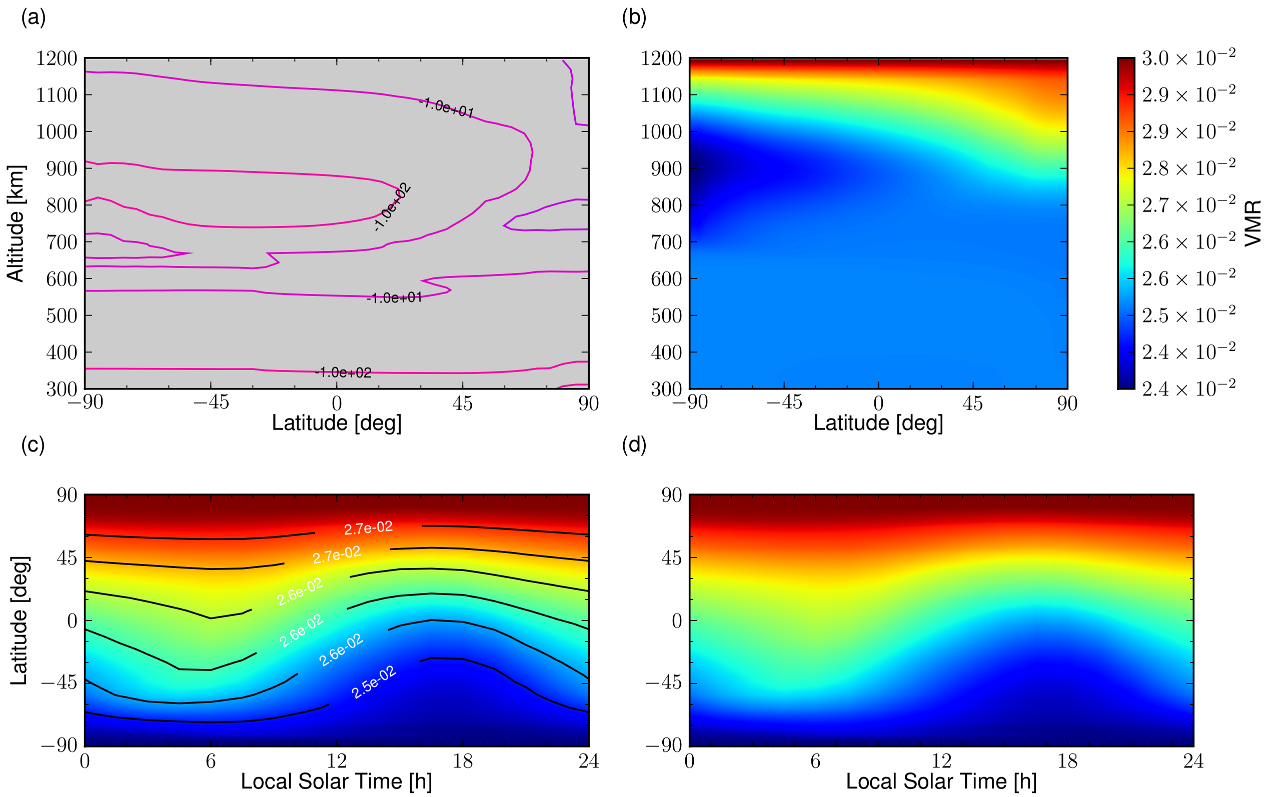

Figure 3.4: Methane (a) zonal-mean production-minus-loss rate [cm^{-3}s^{-1}], (b) zonal-mean VMR, and VMR at about 1,019 km altitude, (c) colored the same as in (b) and with contours labeled in VMR, and (d) as a fraction of the VMR maximum on that level to show the horizontal distribution more clearly.

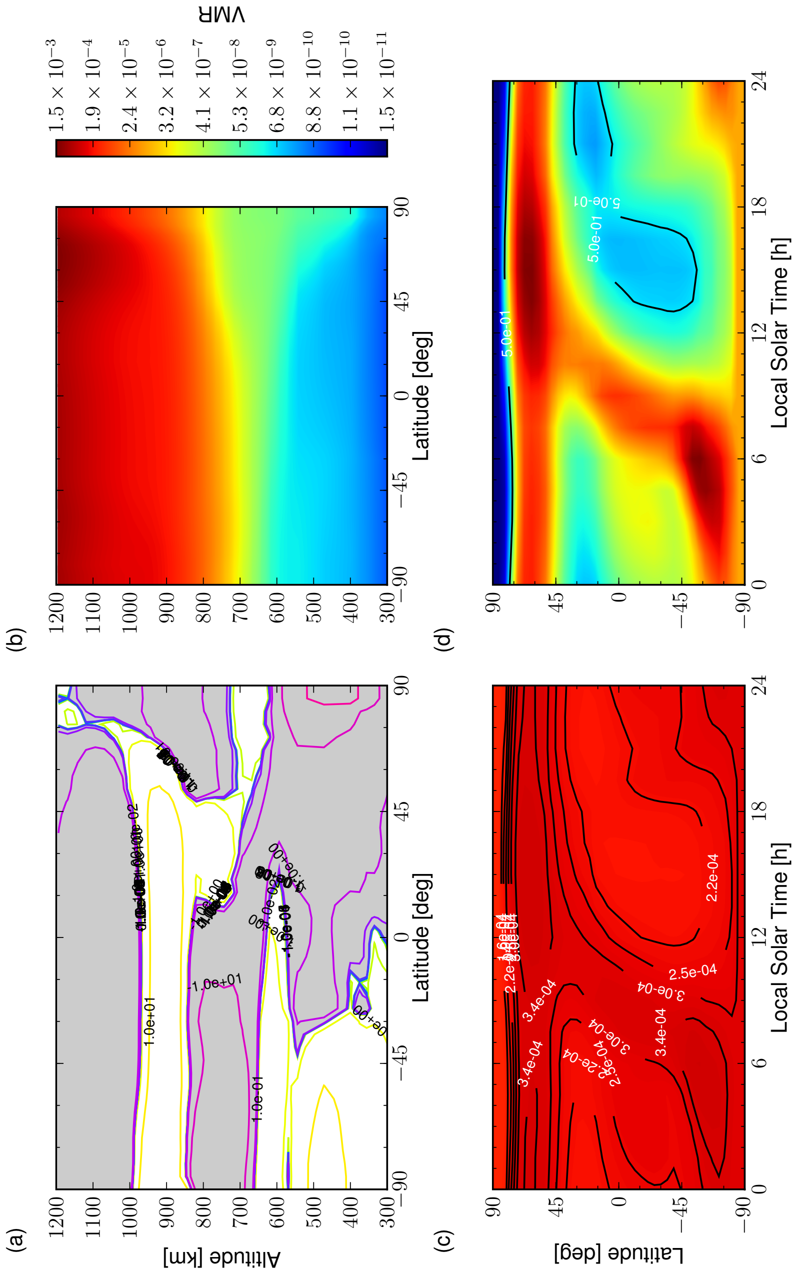

Figure 3.5: Same as Fig. 3.4, but for CH_3.

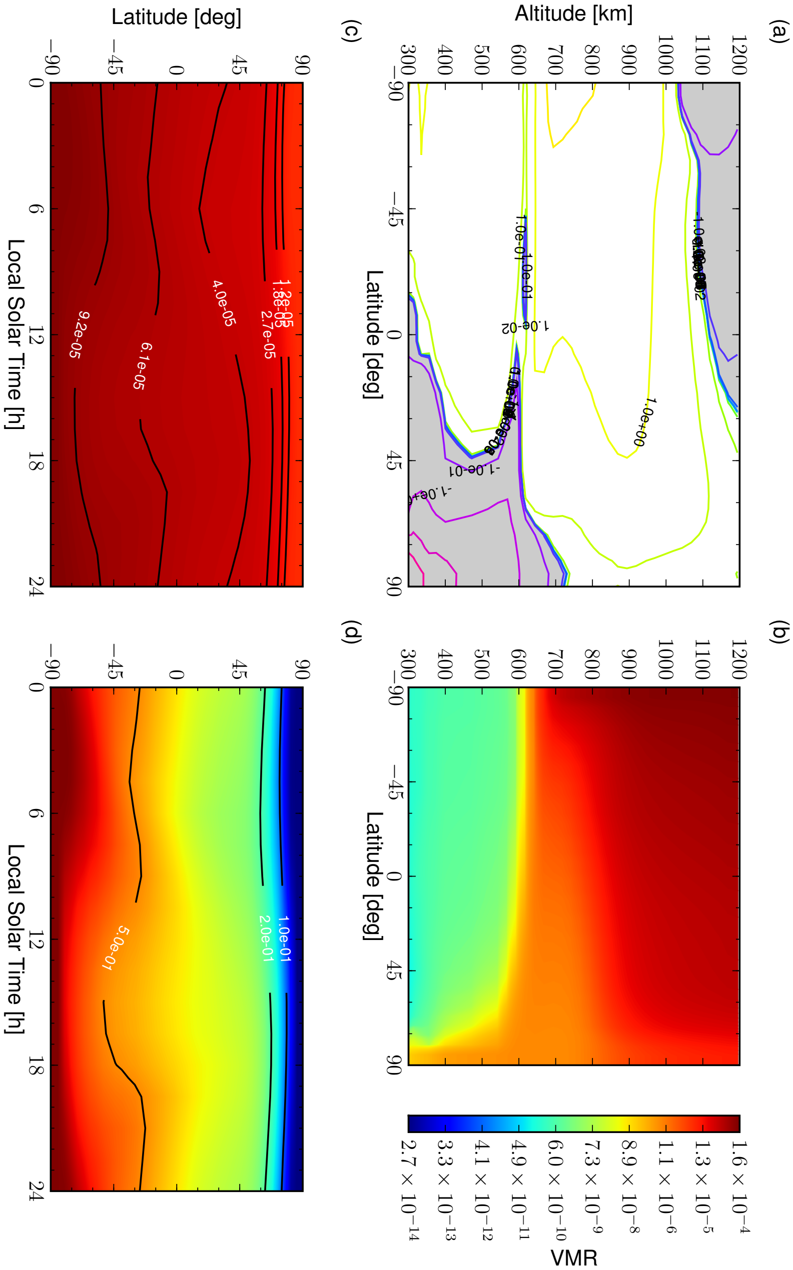

Figure 3.6: Same as Fig. 3.4, but for C_2H_2.

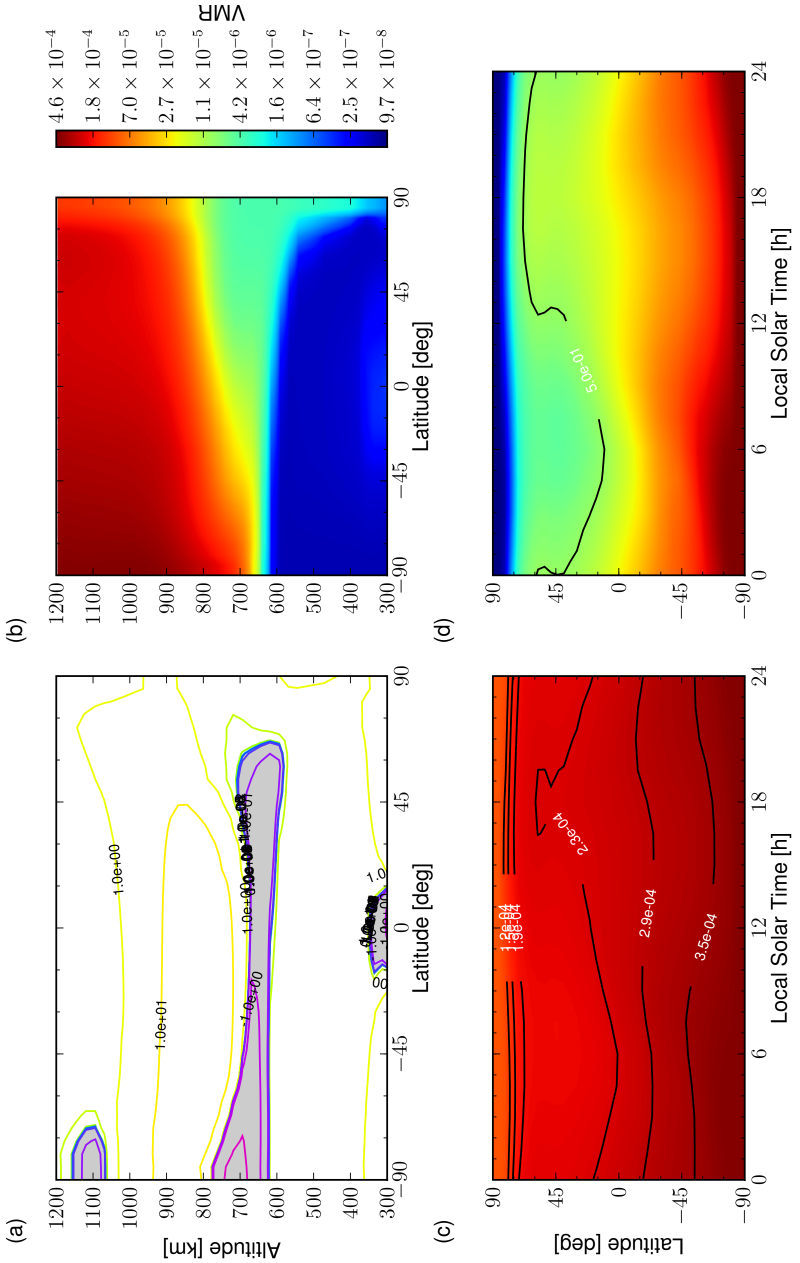

Figure 3.7: Same as Fig. 3.4, but for C_2H_4.

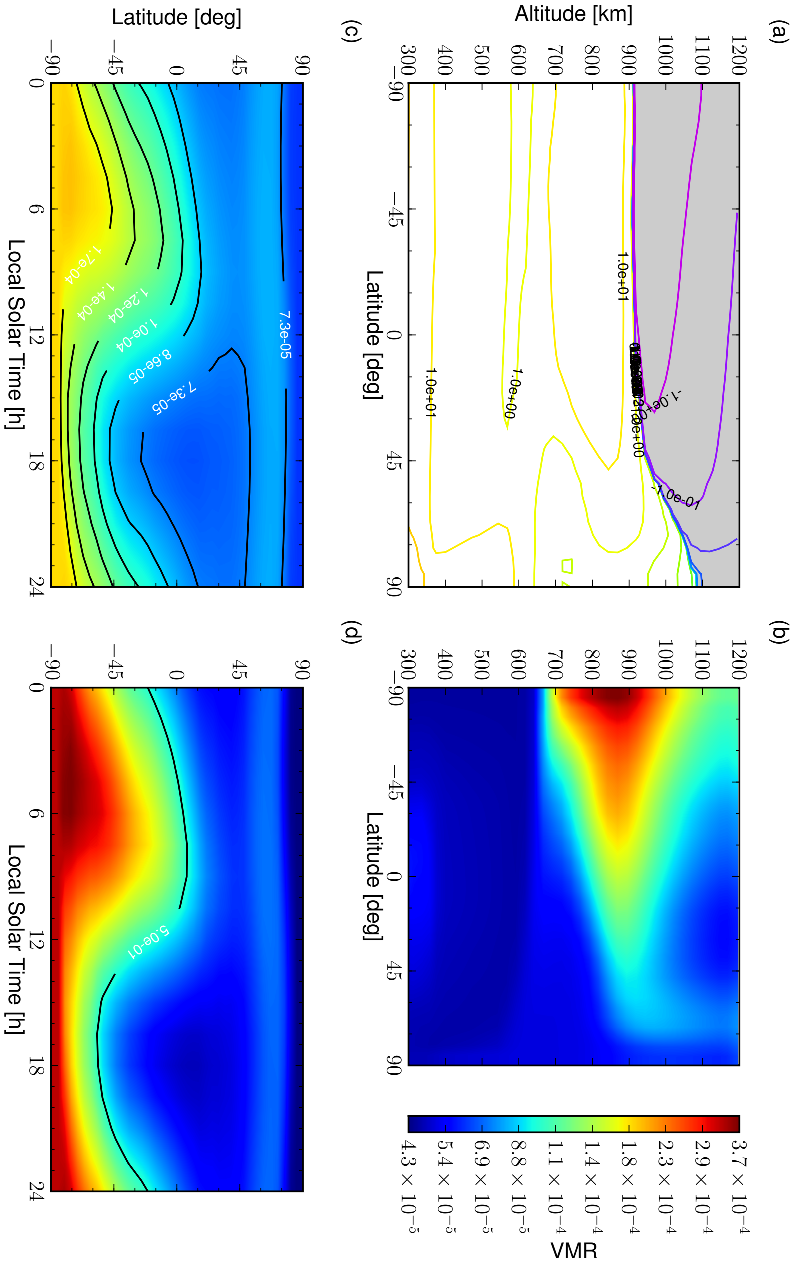

Figure 3.8: Same as Fig. 3.4, but for C_2H_6.

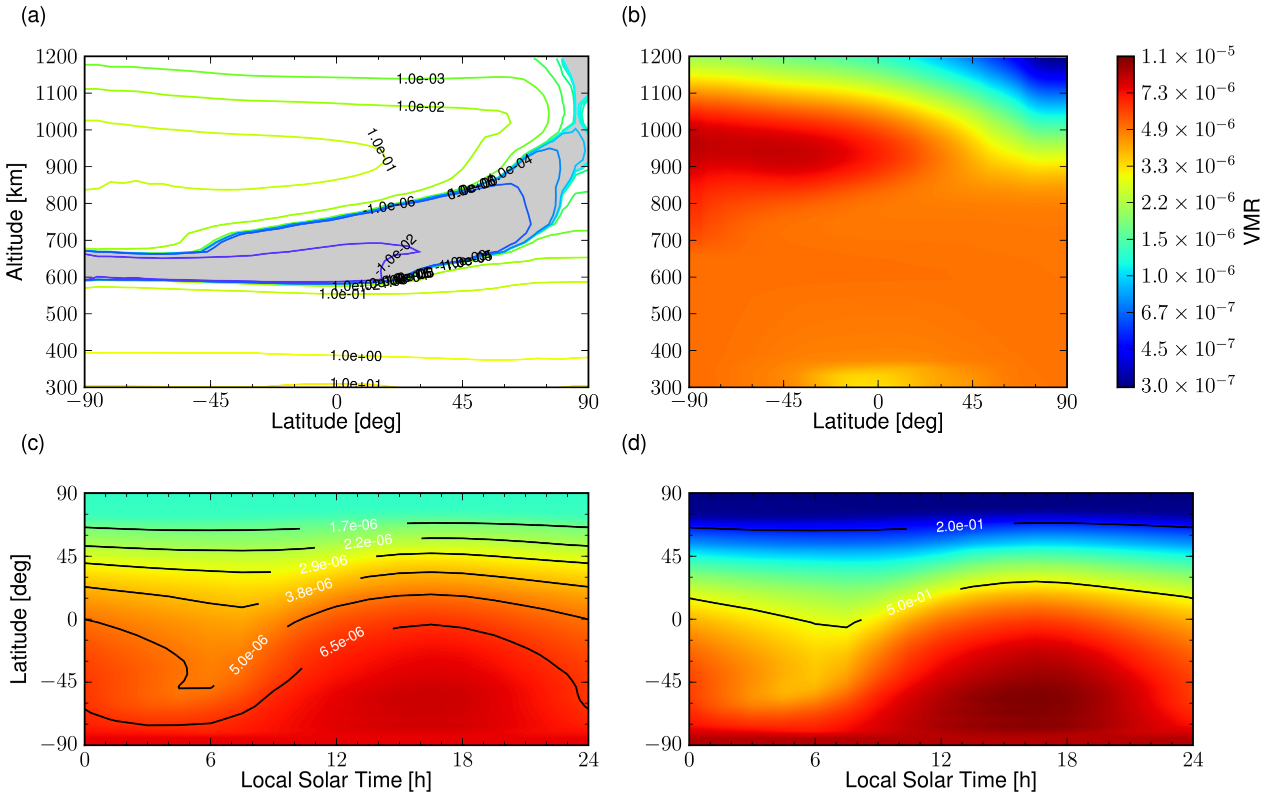

Figure 3.9: Same as Fig. 3.4, but for C_3H_8.

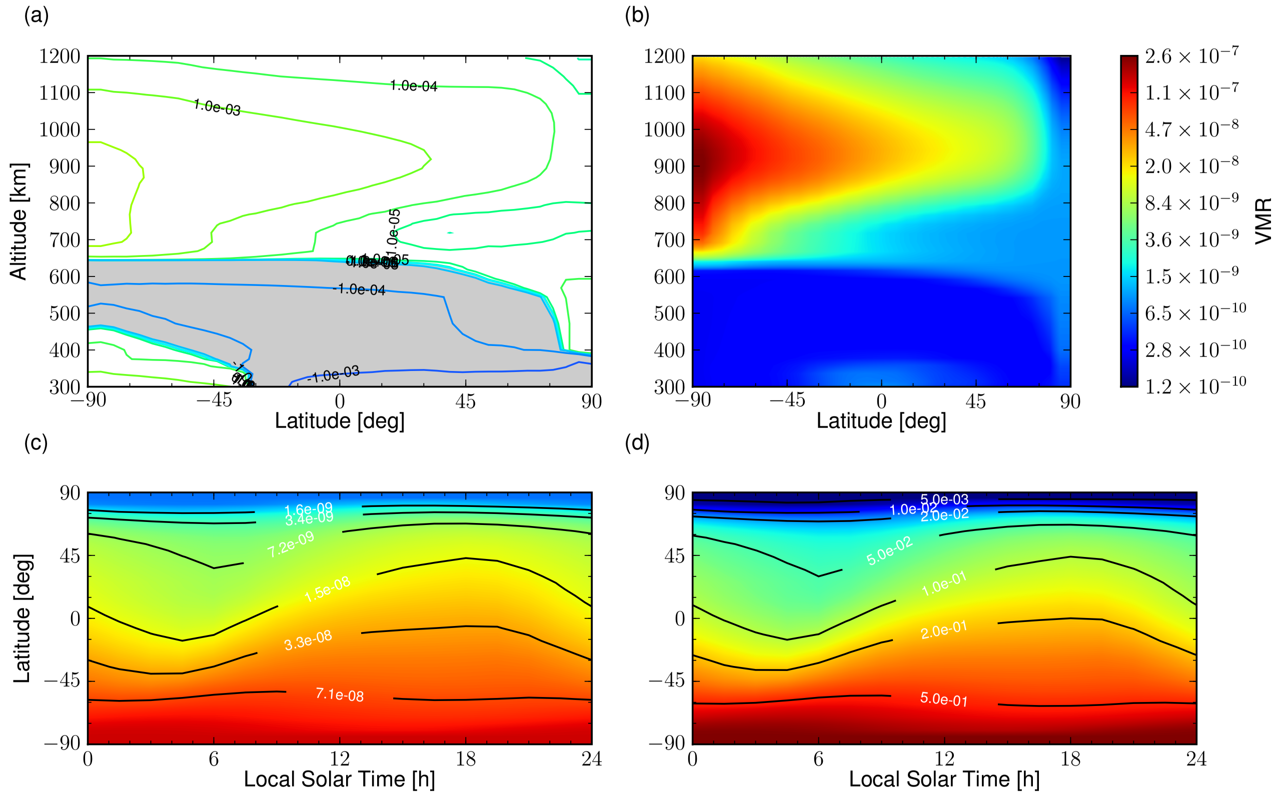

Figure 3.10: Same as Fig. 3.4, but for C_4H_2.

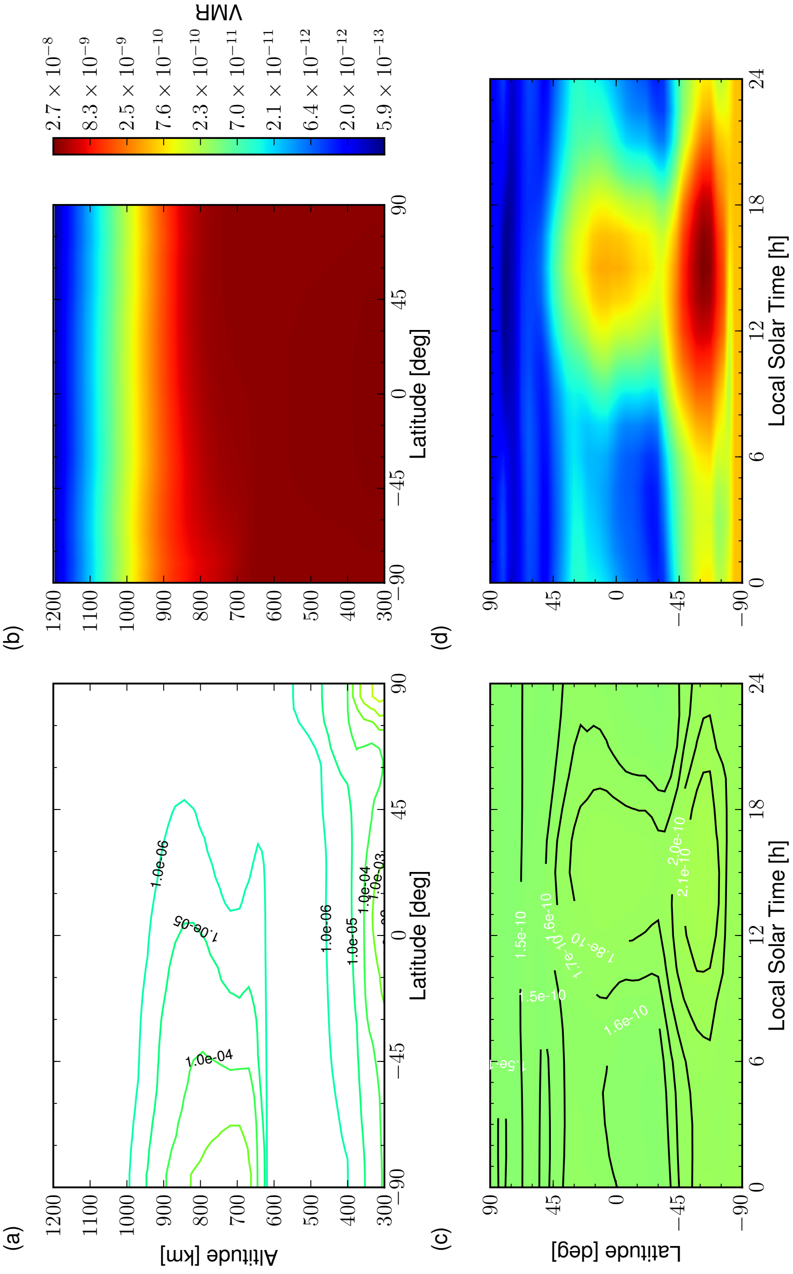

Figure 3.11: Same as Fig. 3.4, but for C_6H_6.

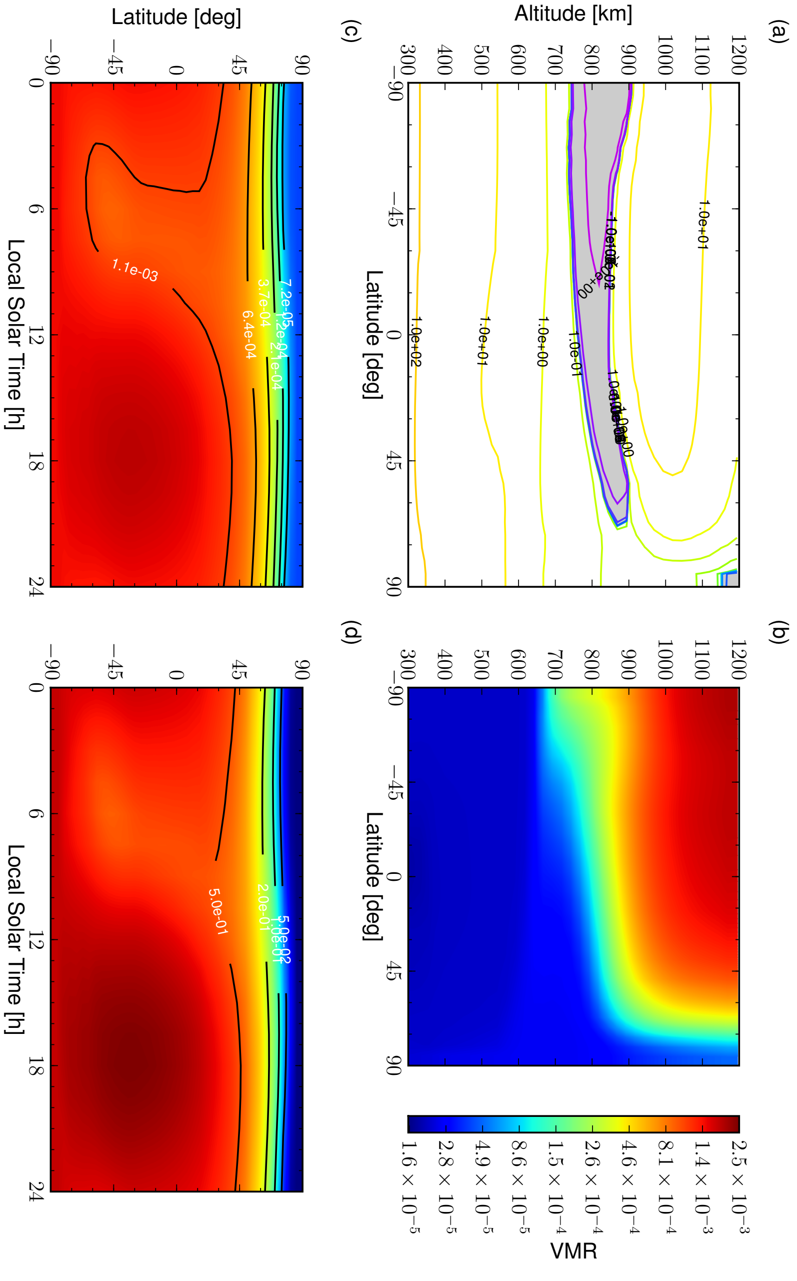

Figure 3.12: Same as Fig. 3.4, but for HCN.

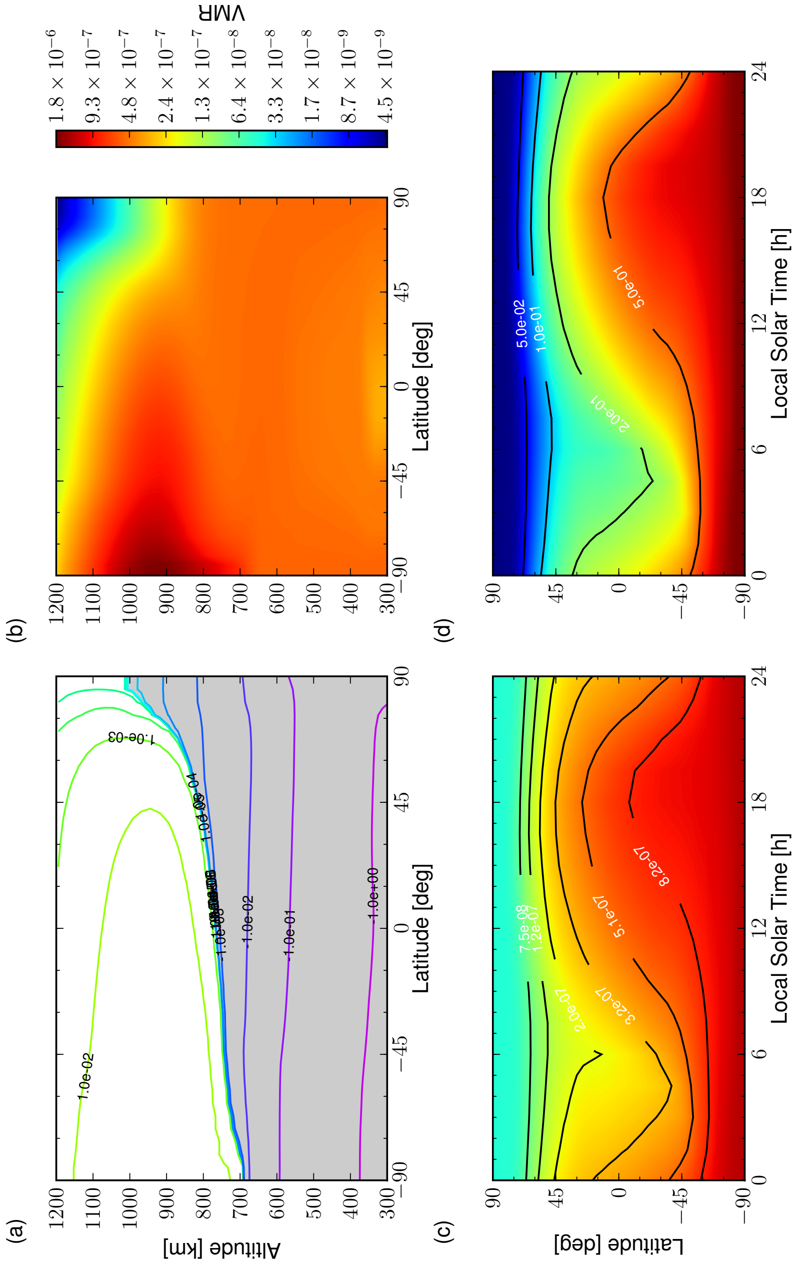

Figure 3.13: Same as Fig. 3.4, but for HC_3N.

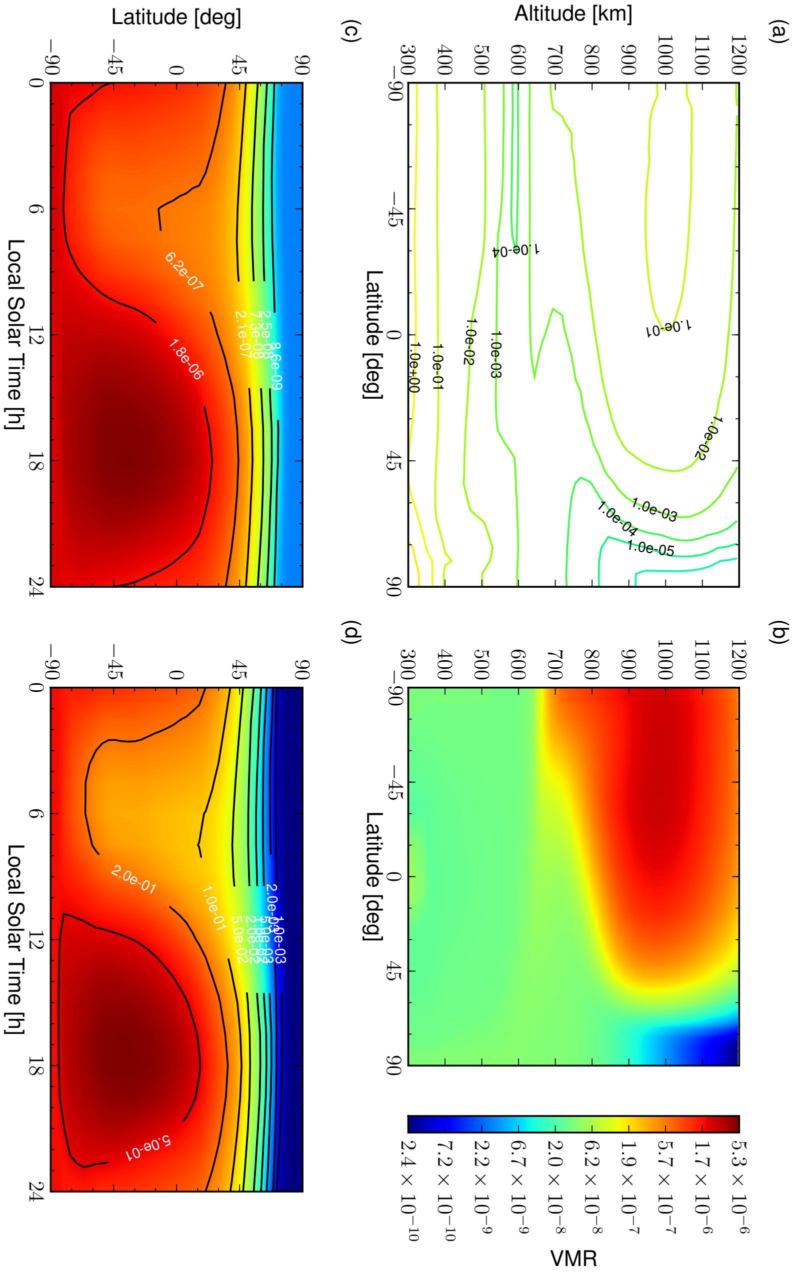

Figure 3.14: Same as Fig. 3.4, but for C_2N_2.

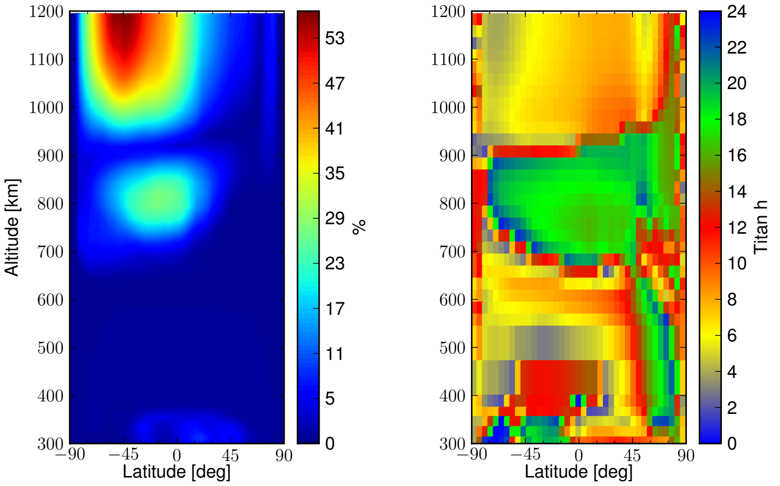

Figure 3.15: Maximum diurnal amplitude of VMR in percentage of mean VMR (left) and Local Solar Time (in Titan hours) of maximum concentration, both for ethane.

Retrieval of data from the model output

The idea of this model output retrieval is to sample the model data at the location which corresponds to the most likely height, latitude, and local Solar time of Cassini when it made the measurement. Possible problems can then arise from the relatively coarse grid resolution in the horizontal and vertical, uncertainty about the altitude (both in the Cassini observations and MOZART), and also from the fact that the MOZART runs use a time-slice constant subsolar latitude of $-20°$, which has to be compensated for by the retrieval. The interpolation is best performed on the logarithm of VMR.

In the scatter plots, linear regression lines for the logarithm of VMR are included and also the respective rank correlations. When doing a linear regression for a scatter plot, the commonly-used linear regression, which minimizes only the Δy's, can give unexpected results for the case when the points almost fall on a vertical line in the plot. Since both model values *and* observations contain an error, the regression has to minimize the orthogonal distance of the points to the regression line, instead of just the vertical distance. This approach is equivalent to fitting an ellipsoid to the data points and choosing the major axis of that ellipsoid as the regression line. That method is called Orthogonal Distance Regression (ODR) and was employed here to obtain the line fits, based on the Fortran library ODRPACK (Boggs, Byrd, and Schnabel, 1985).

The chemical concentrations usually span many orders of magnitude. To conduct statistics on them, they can either be considered to follow a log-normal distribution, which simply means that the data will be normally distributed when transformed logarithmically (Wilks, 1995). This allows the use of standard statistical testing methods like the *t*-test. The alternative to use non-parametric tests based on rank on them, such as the Spearman rank correlation and statistical tests based on the ranks of the data instead of the data itself.

Point-by-point comparison with observations

Figures 3.16 and 3.17 show the model vs observations scatter plots for heights above 1,000 km, where photolysis is fast and dominant, and where therefore the best correlation between measured and simulated values is expected. Figures 3.18 and 3.19 are similar plots for *all* available INMS data.

Ethane C_2H_6 (Fig. 3.16a and 3.18a)

Ethane generally presents a problem for chemistry schemes for the thermosphere, as it is mainly formed by the three-body reaction 2 CH_3 + M → C_2H_6, for which no measurements at Titan conditions exist. This is an issue because CH_3 is important for controlling the concentrations of the other hydrocarbons and the loss of CH_3 by this reaction is important in the lower thermosphere (solid blue line in Fig. 3.20). The existing photochemistry models tend to use an additional amount of tuning on the low-pressure limit rate coefficient of the reaction. When evaluated for a temperature T of 150 K, the Troe rate coefficients for the various models are:

- Wilson and Atreya (2004; their reaction #21): $k_0 = 4.2 \times 10^{-25}$ and $k_\infty = 4.5 \times 10^{-10}$
- Lavvas *et al.* (2008; their reaction #238): $k_0 = 3.6 \times 10^{-25}$ and $k_\infty = 7.4 \times 10^{-11}$
- Krasnopolsky (2009; his reaction #121): $k_0 = 3.7 \times 10^{-25}$ and $k_\infty = 10^{14}$

It is recognized that the uncertainty about this rate (also found in the review of Titan chemistry reactions in Hébrard *et al.*, 2006) constant is one of the major issues with Titan chemistry schemes. Here, it was tried to find a rate coefficient that gives a good fit to measurements. The Lavvas *et al.* rate coefficient was found to produce ethane concentrations that were too low in the SH (due to low production of ethane from CH_3), while the Wilson and Atreya value gave ethane VMRs far above measurements. As a compomise, the expressions $k_0 = 8.4 \times 10^{-27} T^{-8.749}$ and $k_\infty = 7.4 \times 10^{-10}$ were adopted for the rate coefficient, giving a relatively satisfactory positive correlation with

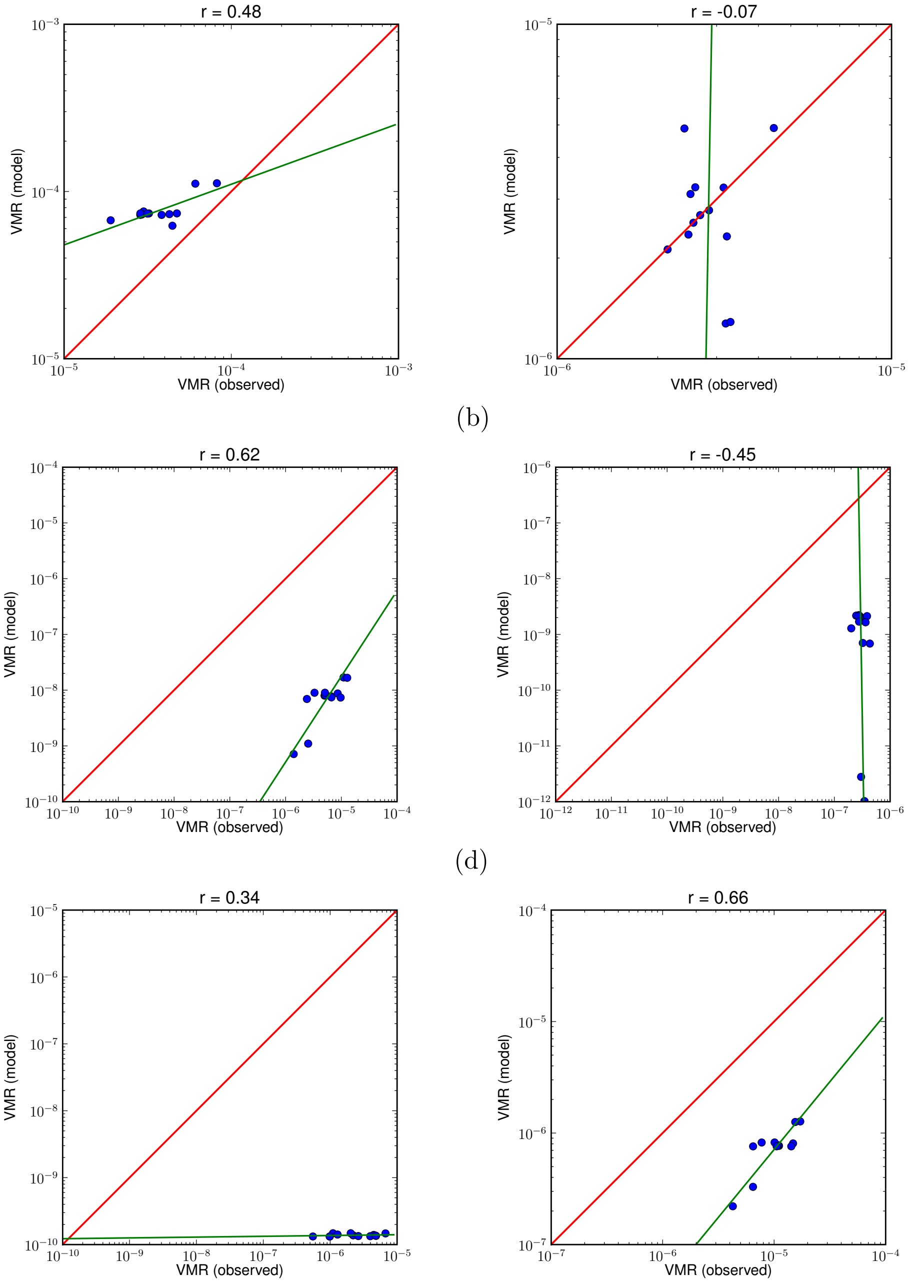

(a) (b) (c) (d) (e) (f)

Figure 3.16: Scatter plots comparing INMS measurements above 1,000 km altitude (horizontal axis) and corresponding MOZART values (vertical axis) from the Control run for (a) C_2H_6, (b) C_3H_8, (c) C_4H_2, (d) C_4H_6, (e) C_6H_6, and (f) CH_3C_2H. The Spearman rank correlation and best-fit line (green) as well as the slope-one line (red) are also shown.

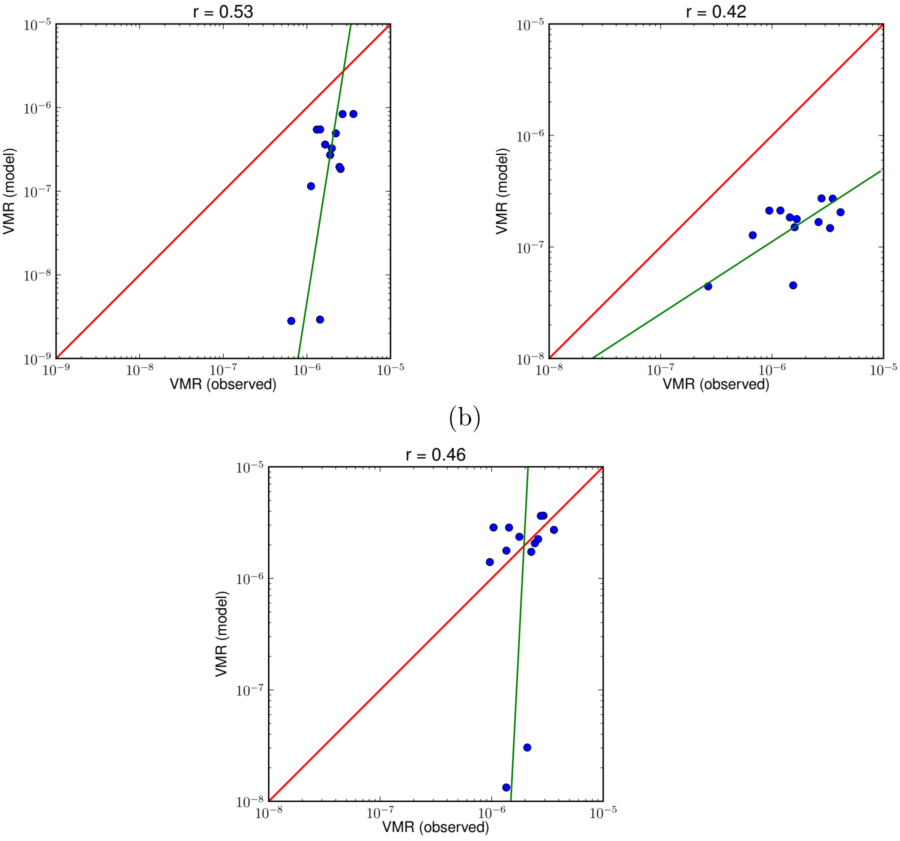

(a)

(b)

(c)

Figure 3.17: Same as Fig. 3.16, but for (a) C_2N_2, (b) HC_3N, and (c) CH_3CN.

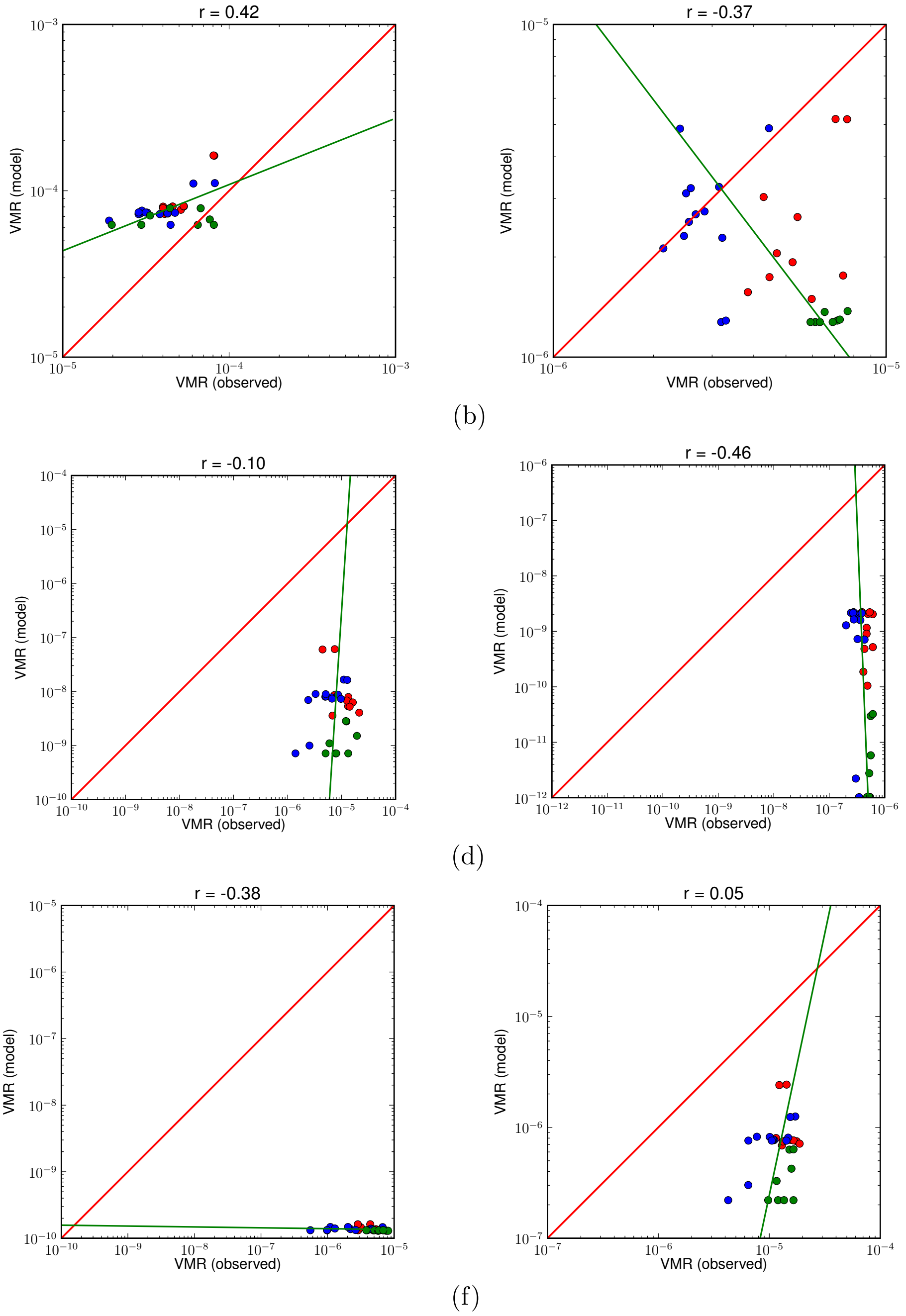

(a) (b) (c) (d) (e) (f)

Figure 3.18: Scatter plots comparing all INMS measurements (horizontal axis) and corresponding MOZART values (vertical axis) from the Control run for (a) C_2H_6, (b) C_3H_8, (c) C_4H_2, (d) C_4H_6, (e) C_6H_6, and (f) CH_3C_2H. The Spearman rank correlation and best-fit line (green) as well as the slope-one line (red) are also shown. Data for heights above 1,000 km is colored blue, data for 975 km and below green, and data in between red.

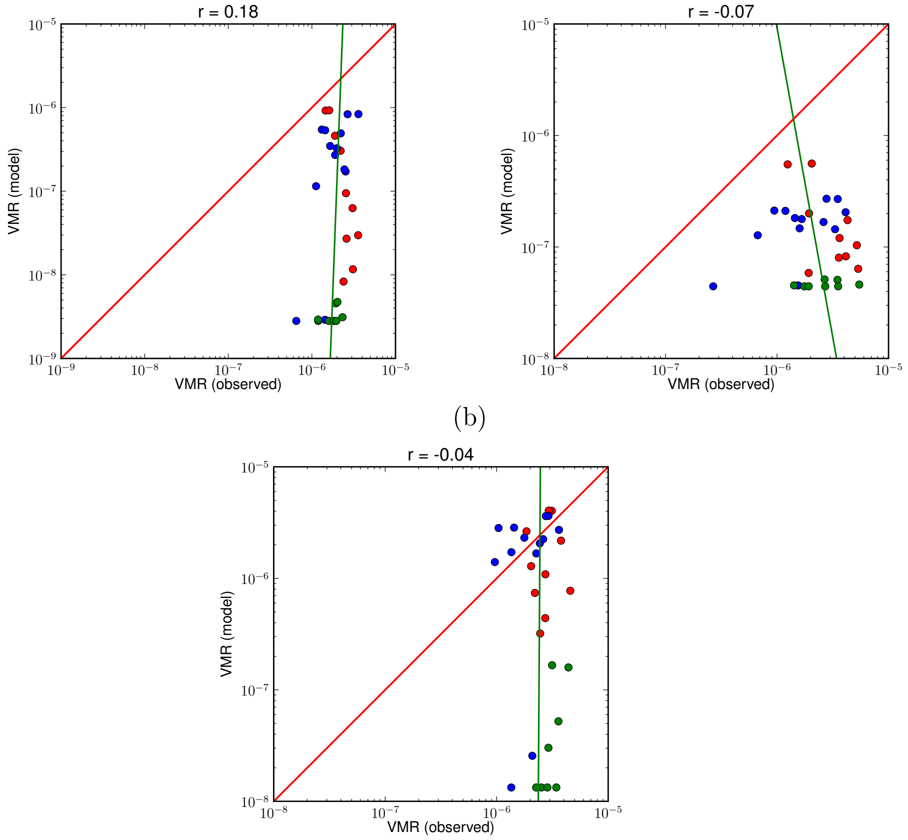

(a)

(b)

(c)

Figure 3.19: Same as Fig. 3.18, but for (a) C_2N_2, (b) HC_3N, and (c) CH_3CN.

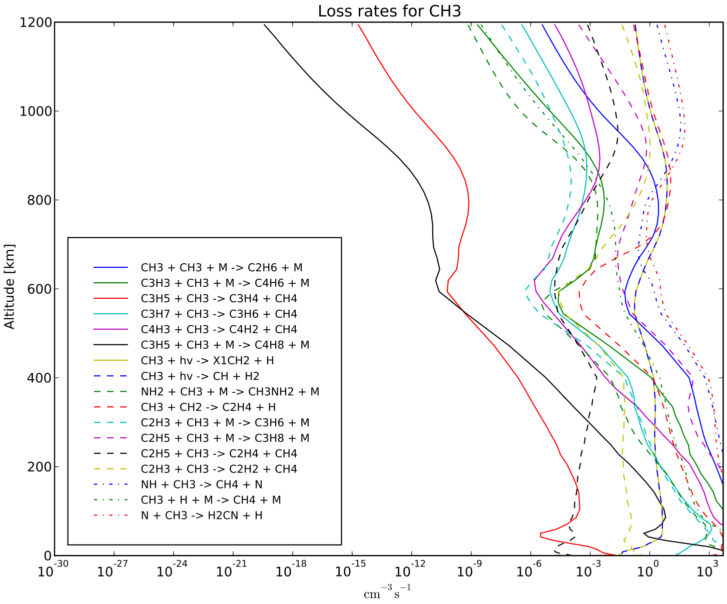

Figure 3.20: CH_3 loss rates for the equator with the Sun at the zenith.

measurements. It is clear however that it would be desirable for this rate to be measured in the lab under Titan conditions, i.e. for about 150 K and with molecular nitrogen as a bath gas, as setting an arbitray rate that conforms with measurements is problematic when lab measurements seem to indicate the rate should be lower. Then again, since lab measurements so far have not been done for Titan conditions, one could infer that the reaction rate is indeed higher on Titan than thought, because otherwise the meridional concentration gradient as measured by Cassini could not be reproduced.

For ethane the two pole points appear to be a better fit with observations than the rest of the data, but of course this depends on the rate constant chosen. Generally VMR variation in the model is somewhat weaker than in measurements, but the overall fit is quite good.

Propane C_3H_8 (Fig. 3.16b and 3.18b)

If the two pole points (which show string depletion in the model) are ignored, the fit to observations is actually quite reasonable for propane. The best-fit line is strongly affected by inclusion of the pole points, however. The very low concentration of propane near the North Pole might likewise respond to an increase in meridional wind.

When lower-altitude points are included, the points in the scatter plot are distributed almost in a rectangle, making it difficult to ascribe to them any particular correlation. The ORD algorithm calls them anticorrelated due to the two conspicuous clusters of points, namely the blue cluster at the center and the green cluster on the lower right, but that seems somewhat arbitrary. A relatively clear height-dependence is apparent: The top layer (blue) is best, then the middle layer (red) has an increase in VMRs in the INMS data and a decrease in the model, more so the bottom (green) layer. So the model VMR generally decreases with height, while the measurements appear to favor higher VMRs at lower altitudes.

In Lavvas *et al.* (2008), the vertical maximum is very broad and low, between about 400 and 800 km height. In this model (Fig. 3.21), the maximum lies somewhat higher at around 950 km altitude, while in Krasnopolsky (2009), the maximum can be found at 400 km altitude. With the limited number of previously available data points, such profiles seemed to be a good fit, but the full Cassini data set makes it clear that the VMR maximum should probably be even higher in the atmosphere to conform with observations. On the other hand, these measurements (Cui *et al.*, 2009) for propane represent an upper bound, so it should then not be surprising that the measured VMRs are higher than the concentrations in the model. Especially for lower thermospheric altitudes, the MOZART models suggests that the measured C_3H_8 VMRs might be unreliable and too high. On the other hand, Fig. 3.21 might suggest that the global values computed from measurements are too low. Certainly inferring a global average from a very limited number of observations is difficult without also using a model and in the case of propane there is a definite possibility that Cui's global average upper bound value is a bit too low.

Species can also be partitioned based on the number of carbon atoms per molecule; Fig. 3.22 shows the resulting global-average total profiles for each class. (Species with 7, 8, 10, and 12 carbon atoms are also present in the chemistry scheme but have been omitted here.) Class 1 is of course mostly the methane profile and higher-order classes have for the most part consecutively lower concentrations. The exceptions to this rule are that C_4X has a slightly higher total VMR than C_3X betwen about 700 and 1,000 km height and that C_6X (dominated by benzene) has higher concentrations than C_5X throughout the vertical domain.

The different carbon classes are for the most part clearly dominated by a certain species, as shown in Table 3.3. C_3X is the only species class in which the dominant species, propane, accounts for slightly less than 50% in the global average, with C_2H_3CN being the other strong contender at about 27% of the global average in that class.

With the exceptions of C_1X and C_2X, all classes exhibit fairly strong vertical

Class #	Dominant species	Dominant species maximum VMR divided by max. class-total VMR
1	CH_4	92%
2	C_2H_4	60%
3	C_3H_8	49%
4	C_4H_3N	99%
5	C_5HN	98%
6	C_6H_6	99.998%

Table 3.3: Dominant species for each class, based on number of carbon atoms.

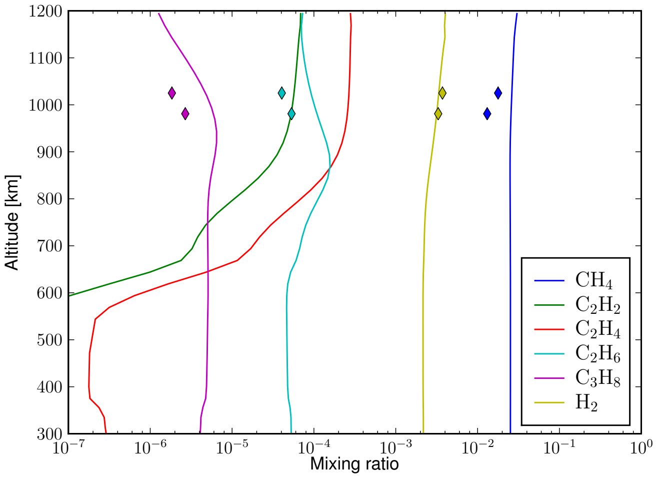

Figure 3.21: Global-average VMR profiles for selected species from the Control run with measurements from Cui *et al.* (2009). (The measured value for propane is meant to represent an upper bound.)

VMR gradients in the upper thermosphere, i.e. above about 800 km height—an important feature when comparing model results to measurements, because vertical uncertainty in either model results or observations can lead to major discrepancies for species with large vertical gradients.

Diacetylene C_4H_2 (Fig. 3.16c and 3.18c)

Overall diacetylene concentration is much lower in the model (by about a factor of 100), but the correlation with measurements is quite satisfactory. If a species shows a good correlation to measurements, even if the global averages do not match, it is still a successful example of 3–D modeling. The Krasnopolsky (2009) model does feature somewhat higher diacetylene concentrations, presumably because of higher production by

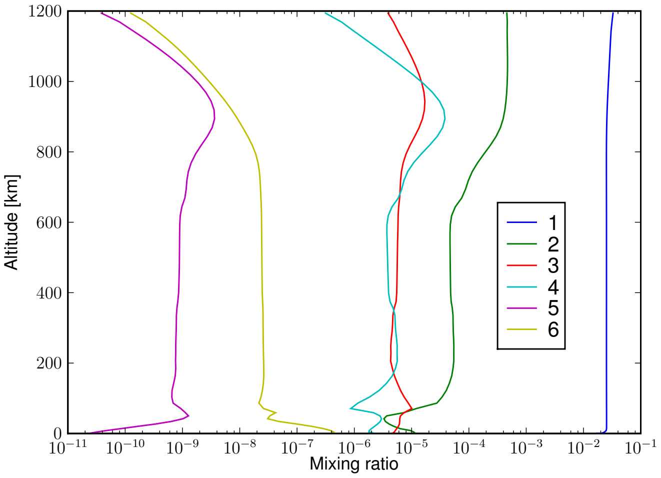

Figure 3.22: Global-average total VMR profiles for each class of species, where the class number corresponds to the number of carbon atoms in the molecule.

$$C_2H + C_2H_2 \rightarrow C_4H_2 + H$$

which is the main production mechanism for diacetylene. C_2H is formed by photolysis of C_2H_2, so the adopted cross sections and quantum yields determine its concentration. Krasnopolsky appears to use a constant quantum yield of 0.3 for all wavelenths, while here the branching ratios from Lavvas *et al.* (2008) are employed, which vary between 0.06 and 0.3, so it is not surprising that C_2H production in this model would be lower. No measurements for C_2H exist, highlighting once more the dilemma for Titan chemistry modeling that some of the very important photolytic products like C_2 and C_2H can really only be discussed in terms of their effect on other, measured species. Direct measurements of e.g. C_2 would be extremely helpful for sorting out these discrepancies between models, insasmuch as they are caused by uncertainty about these "hidden" species.

The correlation with measurements becomes somewhat worse when using all available data, although the layer below 975 km altitude taken alone actually shows a very similar behavior in the scatter plot as the one above 1,000 km height. So the main problem seems to be the region between 975 and 1,000 km altitude, where especially the two pole points show high VMR in the model and relatively low VMR in the INMS data. Again, the possibility that this reflects an issue with the retrieval should not be ruled out, although it is thought that the Cassini measurements of diacetylene are amongst the more reliable data points (J. Cui, pers. comm.).

1,3-Butadiene C_4H_6 (Fig. 3.16d and 3.18d)

Comparison with observations is made more difficult in the case of 1,3-butadiene by the fact that its INMS detections are not very firm and only represent upper boundaries (Cui *et al.*, 2008 and J. Cui, pers. comm.). It is therefore not very surprising that the measurements show almost no variation compared to the factor-1000 differences found in the model.

A heavy species such as C_4H_6 would generally be assumed to exhibit a strong vertical gradient due to molecular diffusion. These INMS measurements appear not to be very trustworthy and the model may be closer to reality in this case than currently available retrievals.

Benzene C_6H_6 (Fig. 3.16e and 3.18e)

Benzene shows a similarly good correlation as C_4H_2 with observations, but the concentrations in the model are about a factor of 1,000 lower than observations. Boosting the production of benzene, especially in the thermosphere, to get a better match with observations has long been a goal of Titan chemistry models, and while the e.g. Lavvas *et al.* (2008) generally has realistic benzene VMRs at lower altitudes, their concentrations in the thermosphere are much too low. The Krasnopolsky (2009) model seems to provide an improvement, but although large parts of its chemistry scheme have been adopted here, benzene is still very low here. The reason for this discrepancy is not obvious. Benzene production is dominated by

$$C_3H_3 + C_3H_3 + M \rightarrow C_6H_6 + M$$

Production of the propargyl radical (C_3H_3) in turn involves many different reactions of roughly equal importance (Fig. 3.23a), making it difficult to find out the difference to other models when no production rates per chemical process are given. Atomic hydrogen is needed for the dominant loss reactions, therefore differences in the assumed H distributions might increase C_3H_3 destruction and thereby decrease benzene formation. However, this hypothesis has not been tested with the model. Also, atomic hydrogen takes part in many chemical reactions, so it seems unlikely that it would not also change many other concentrations in the model. Finally, the assumed atomic hydrogen profile (Lavvas *et al.*, 2008) appears to be quite well-constrained by the few available observations.

But while the model does not represent global-averages of benzene VMRs very well, it does achieve a slight positive correlation with measurements in the high thermosphere. Inclusion of the additional data reveals problems in the form of two model outliers in the middle (red) layer and an anti-correlation in the lower (green) layer.

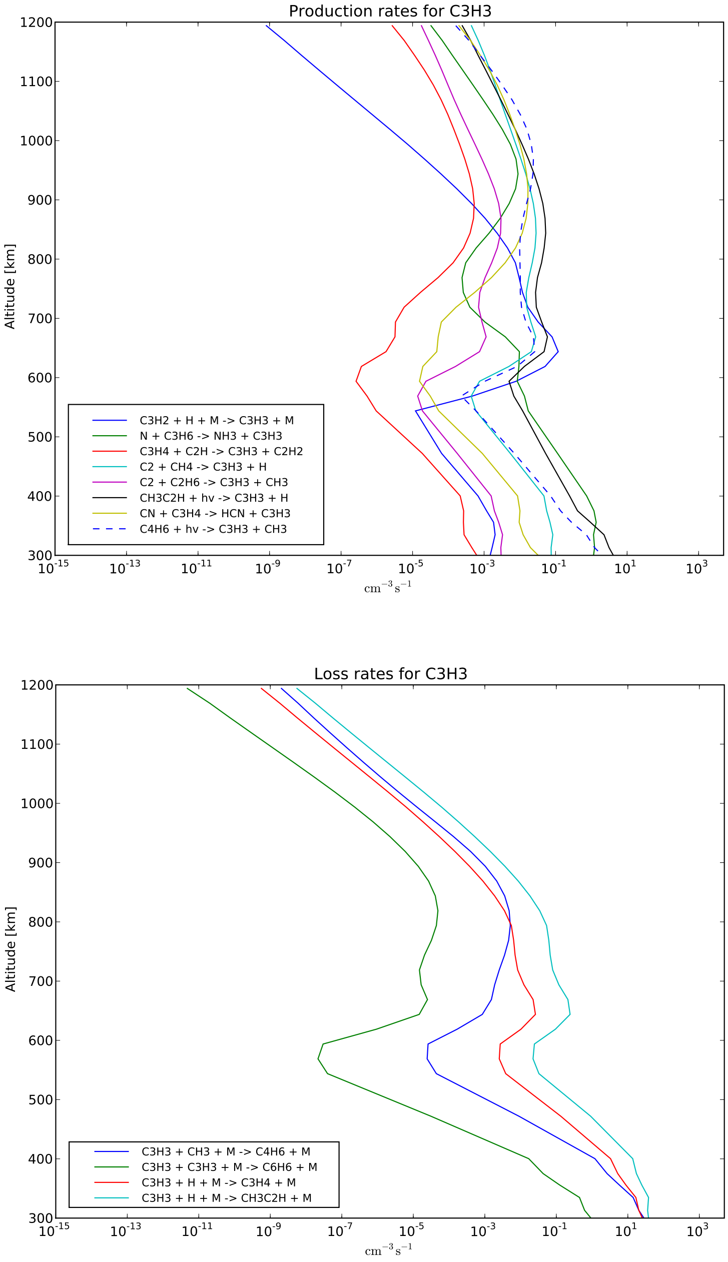

(a)

(b)

Figure 3.23: Propargyl radical (a) production and (b) loss rates for the equator with the Sun at the zenith.

Methylacetylene CH_3C_2H (Fig. 3.16f and 3.18f)

CH_3C_2H is an interesting species in that models generally seem to have problems with it. Krasnopolsky (2009) for example does not show plots of that species, so it is particularly welcome that this species is looking quite resonable, both in terms of correlation and of absolute values. The only issue seems to be the lower (green) region, where modeled VMRs are considerably too low. Then again, CH_3C_2H is not counted among the species which have been detected by Cassini INMS with high certainty (J. Cui, pers. comm.), therefore it is conceivable that the observed VMRs in the lower layer are somewhat too high.

Cyanogen C_2N_2 (Fig. 3.17a and 3.19a)

Cynaogen concentrations look quite realistic above 1,000 km height, with simulated values exhibiting even greater variability than measurements. Things become somewhat too variable below that. For a relatively heavy species, C_2N_2 show conspicuously little variability in the Cassini INMS data. Then again, the cyanogen profile given in Krasnopolky (2009) shows only a slow drop in VMR with altitude that is relatively well in line with measurements.

The zonal-mean distribution (Fig. 3.14) shows that the vertical gradient is realistic in the SH, but that there is either too little local production of C_2N_2 or transport from the SH, resulting in a sharp drop in concentrations towards the NP.

Cyanoacetylene HC_3N (Fig. 3.17b and 3.19b)

In the case of HC_3N, there is a good fit above 1,000 km height, but too much VMR variation in the lower layers in the model. VMR variation in the observations is quite low, and the data seens to indicate there is little concentration difference between the higher and lower thermosphere. Again, stronger northward transport might be a way to get the model more in line with observations.

Acetonitrile CH_3CN (Fig. 3.17c and 3.19c)

Acetonitrile, with the exception of the pole points, shows a decent fit with observations above 1,000 km height, but as in the case of the other nitriles, variation below 975 km altitude is too strong in the model. The zonal-mean VMR (not shown) has a maximum at about 1,050 km altitude, with a steep drop in VMR below 950 km height. This might be related to the lower availability of atomic nitrogen at these levels.

Validation summary

The Cassini measurements show generally low variability, which is particularly surprising for heavier species like C_4H_6. In Cui *et al.* (2009) it is acknowledged that several of these species have not been detected very securely, so model VMRs below the detected upper bound concentrations are not a problem. Besides the issue of the statistical certainty of the Cassini measurements, there might also still be remaining issues with chemical reactions on the detector chamber wall that would contribute to increased concentrations of hydrocarbons and nitriles. Accounting for these extra reaction in the INMS chamber and compensating for them in the retrieved concentrations is difficult and may not have been entirely succesful.

Generally, the fit of the measured species between model and observations is for the most part quite acceptable, with the model having the highest skill in the upper thermosphere as expected. At lower levels, factors such as the precise strength meridional transport become more important and impact the match between model and observations. The following section will take a closer look at these dynamical influences.

3.2 Sensitivity to the strength of circulation

As the previous section has shown, comparison between model predictions and data suggest that the GCM-based meridional wind field might be too weak. The two measurements close to Titan's North Pole tend to show concentrations that are closer to the other observations, while in MOZART output the difference is larger. Therefore, it is investigated here whether increasing the meridional wind from its GCM control run values improves the fit.

The approach was to multiply the v wind with a factor of two above a height of 350 km, chosen so that winds in the lower stratosphere and troposphere would be unaffected. Similar sensitivity experiments (Doege *et al.*, 2008) with a previous version of this model that included stronger GCM wind fields (Wodarg *et al.*, 2000 and 2003) had shown that several species, notably ethane, are highly sensitive to a doubling of meridional wind. Since ethane was a species that was anticorrelated with measurements in the control run, it was theorized that such an increase in meridional wind might be sufficient to reverse that gradient and bring it in line with observations.

Comparison to a run without advection

To ascertain the effect of advection in the model, in particular in the thermosphere, a restart run without advection ("Zero") was conducted. (This is also useful as a reference for the later Solar Min and Max experiments, as in those runs the wind field falls about in the middle between the Control and Zero runs.)

Figures 3.24 to 3.27 are scatter plots for the zero-wind experiment and observations. Ethane VMR is generally higher than in Control, and the correlation is improved because there is more variability in the model. So at least in the case of ethane, the circulation seems to have the effect of evening out VMR gradients, and based on ethane alone it might be assumed that the v wind in the Control run is still somewhat too high.

Propane has somewhat higher VMR at the NP, which will be shown in more detail in Fig. 3.29 below. The same is true for C_4H_2, while C_4H_6 concentration at the NP further decreases. The correlation of benzene with measurements is improved from 0.34 to 0.54, while for CH_3C_2H depletion at the NP is stronger without advection to compensate for it. The remaining three species plotted here do not experience any significant change in their concentrations. The lifetime of HC_3N is relatively high as shown in Table 3.2, so it is somewhat surprising that it is not more strongly affected by the circulation. But while its maximum and minimum VMR are almost unchanged from Control, the points between the extreme in the scatter plot shift somewhat towards lower concentrations.

When all available data points are included in the analysis, ethane (Fig. 3.26a) exhibits a clear vertical stratification in the scatter plot, with the highest concentrations in the higher thermosphere above 1,000 km height (shown in blue), and the lowest below 975 km. Therefore, the increased variability in the model seems to mainly come about because of a stronger vertical gradient, not because of differences in horizontal distributions. By comparison, in the Control run (Fig. 3.18a) the VMRs at different layers more or less coincided in the scatter plot.

All in all, this experiment shows that many species are only weakly affected by advection–C_2H_6, C_6H_6, and CH_3C_2H stand out as being more sensitive to wind, while others show little dependence, especially in terms of their rank correlation with measurements, which at any rate is not sensitive enough to register the effect of subtle changes in the distributions. Also, many species span many orders of magnitude in concentration so that e.g. a factor of two difference does not show up readily.

Therefore it is useful to look at the changes in VMRs in terms of percentages from Control to Zero. The ethane zonal mean (Fig. 3.8b) has a VMR maximum at the SP between 800 and 900 km altitude, and a broader VMR minimum between 1,100 and 1,200 km height at about 30°N. In the Zero run, ethane VMR increases very strongly at the EQ and slightly at the NP around 800 km height, while there is a drop in concentrations at the poles (Fig. 3.28).

Propane (Fig. 3.29) looks quite similar to ethane in its response to the lack

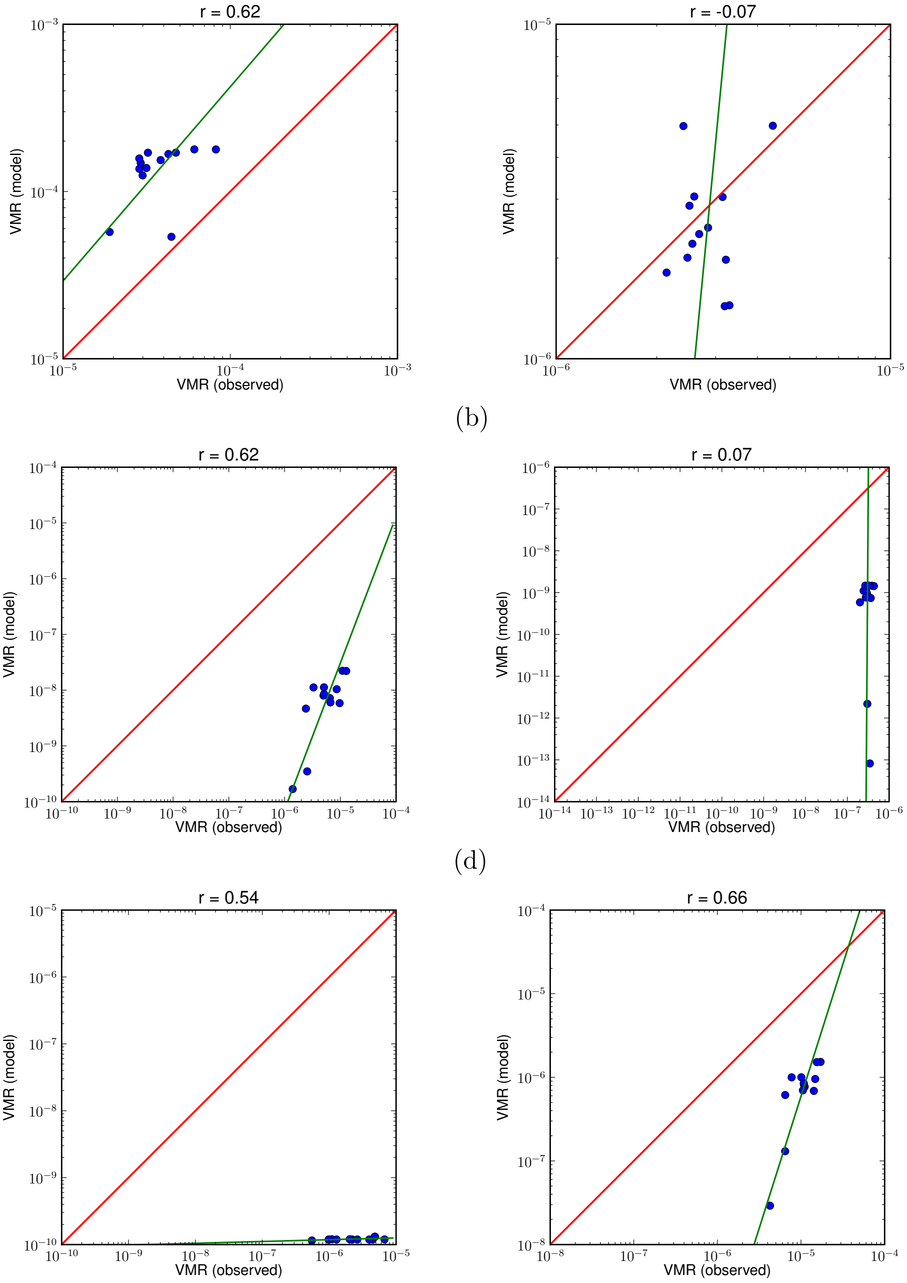

(a) (b) (c) (d) (e) (f)

Figure 3.24: Scatter plots comparing INMS measurements above 1,000 km altitude (horizontal axis) and corresponding MOZART values (vertical axis) from the Zero run for (a) C_2H_6, (b) C_3H_8, (c) C_4H_2, (d) C_4H_6, (e) C_6H_6, and (f) CH_3C_2H. The Spearman rank correlation and best-fit line (green) as well as the slope-one line (red) are also shown.

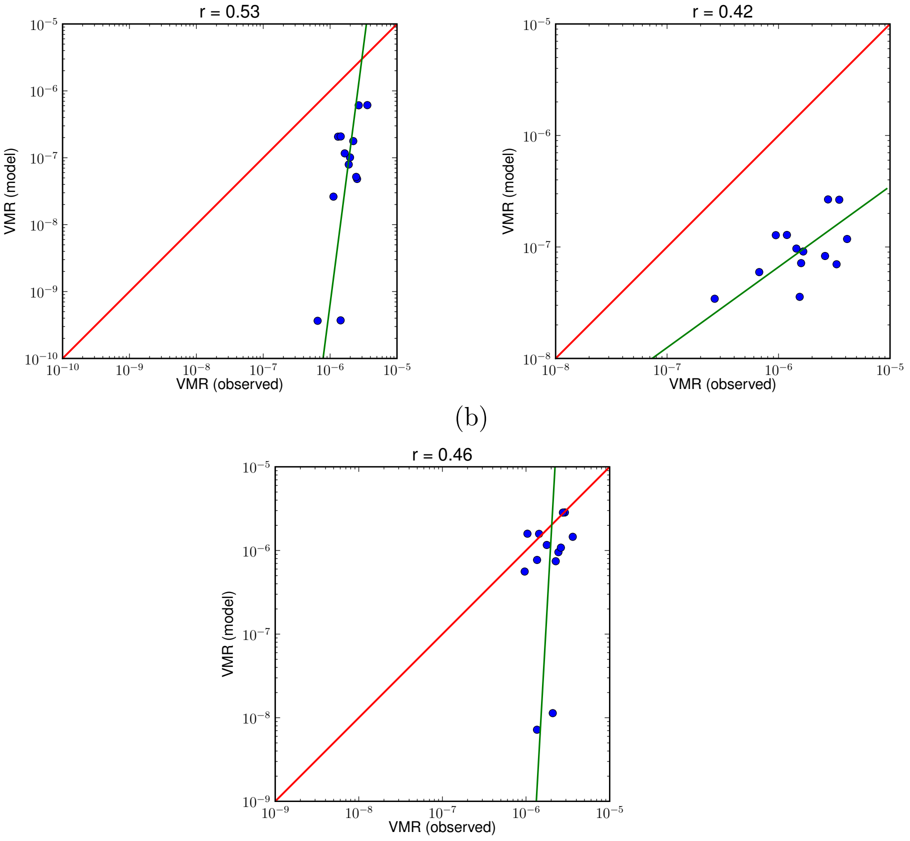

(a)

(b)

(c)

Figure 3.25: Same as Fig. 3.24, but for (a) C_2N_2, (b) HC_3N, and (c) CH_3CN.

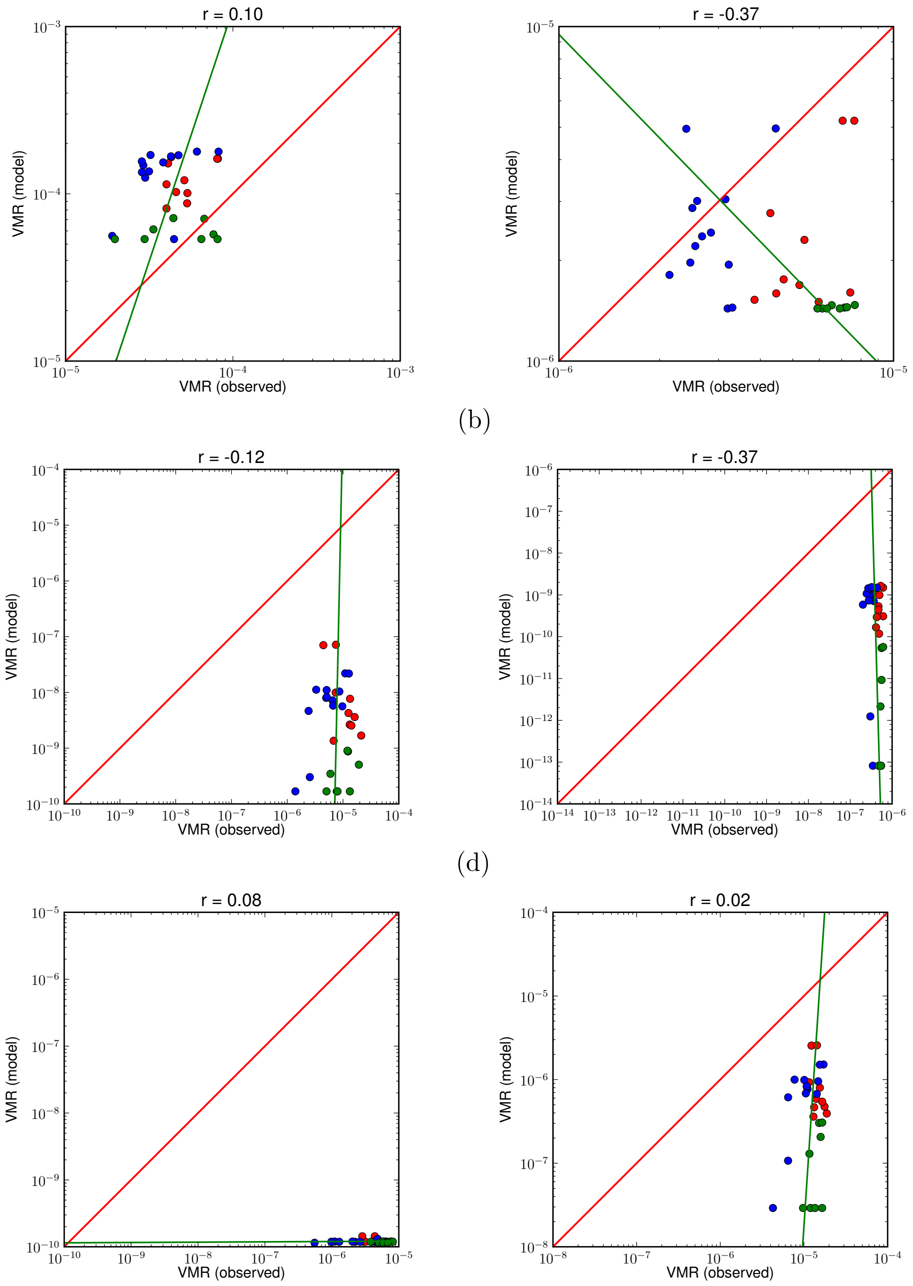

(a) (b) (c) (d) (e) (f)

Figure 3.26: Scatter plots comparing all INMS measurements (horizontal axis) and corresponding MOZART values (vertical axis) from the Zero run for (a) C_2H_6, (b) C_3H_8, (c) C_4H_2, (d) C_4H_6, (e) C_6H_6, and (f) CH_3C_2H. The Spearman rank correlation and best-fit line (green) as well as the slope-one line (red) are also shown. Data for heights above 1,000 km is colored blue, data for 975 km and below green, and data in between red.

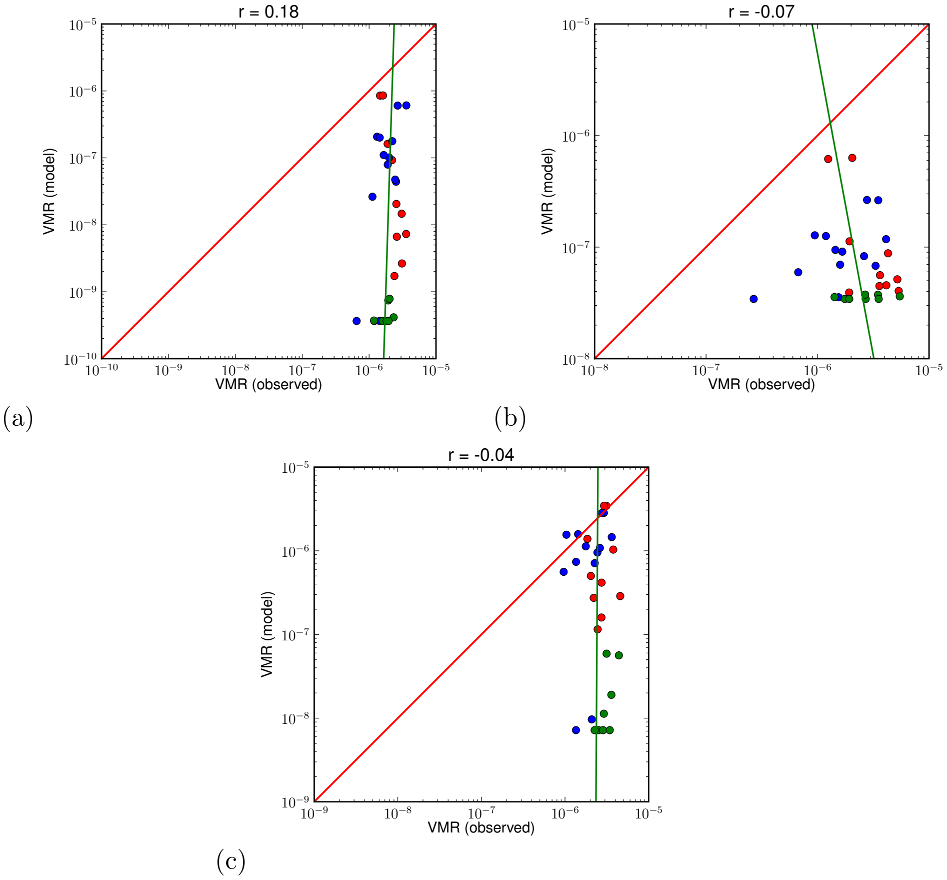

(a)

(b)

(c)

Figure 3.27: Same as Fig. 3.26, but for (a) C_2N_2, (b) HC_3N, and (c) CH_3CN.

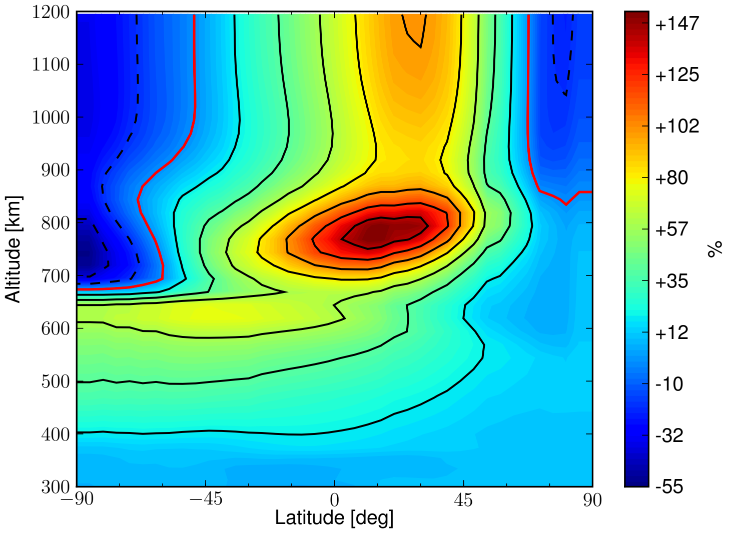

Figure 3.28: Relative differences for C_2H_6 VMR (Zero/Control -1). The red contour corresponds to no change in concentration.

of meridional circulation, except its VMR increases at the NP in the Zero run. This is also apparent in the scatter plot (Fig. 3.24b), where the lowest two points in the diagram, which represent measurements close to the NP, shift upwards towards to slope 1 line.

Finally, HC_3N increases in the SH and decreases North of 45°N, as shown in Fig. 3.30. All three species show a strong sensitivity around 800 to 900 km altitude, with a more muted response above. This is consistent with the lifetime plots, which made it clear that advection is most likely to have a significant effect on concentrations in that height range.

The dependence of concentrations on meridional wind can also be numerically investigated with a statistical significance test, to show in which areas the zonal mean concentrations differ significantly between Control and Zero. Up to now the implicit assumption has been made that the differences are significant, at least above 600 km height, which is the primary vertical range of interest here. The provided GCM wind field is extremely smooth without noise in that range and the horizontal distributions of chemical species stay fixed after the model has found a stable solution and only circle Titan's globe with the diurnal cycle. In Doege *et al.* (2008), it was found that e.g. for methane, fluctuations in the instantaneous zonal-mean VMR come about because of grid-point aliasing the zonal direction (i.e., the maximum value will appear to be higher when the

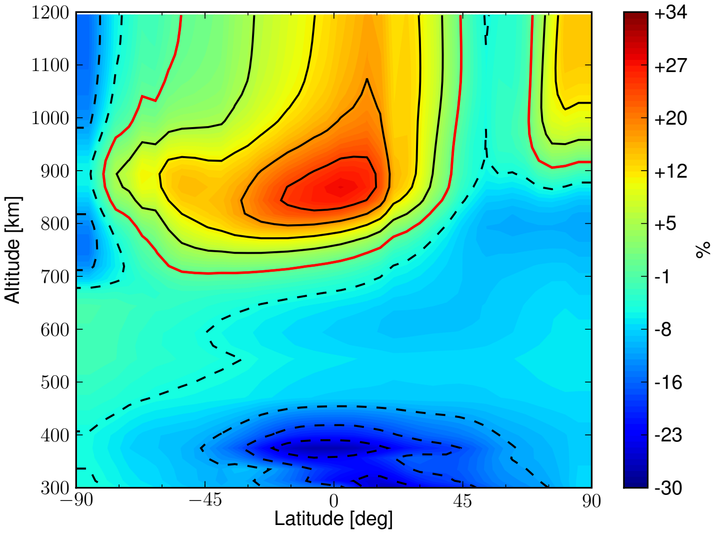

Figure 3.29: Same as 3.28, but for C_3H_8.

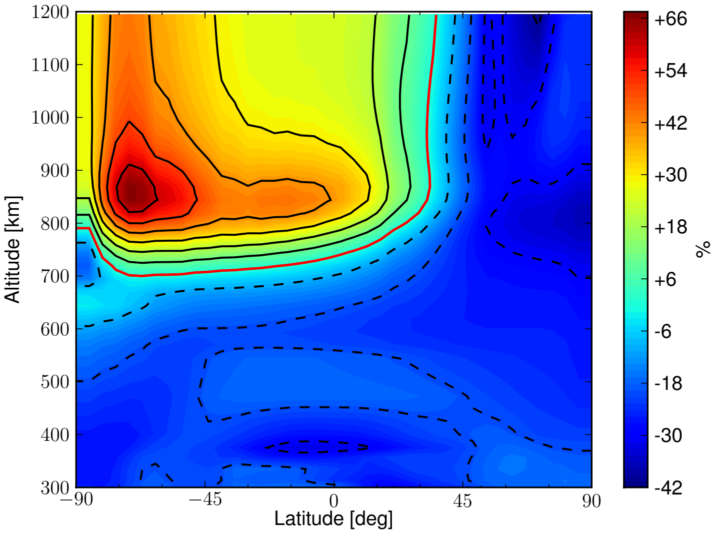

Figure 3.30: Same as 3.28, but for HC_3N.

location of the maximum happens to be at the meridian where the model has grid points, and will seem diminished if it falls in the middle between grid lines.) Time-averaging and spline interpolation were shown there to give very stable results for the zonal means of each species, removing the aliasing noise in the instantaneous fields.

However, even if these facts suggest that, in the absense of appreciable noise in the model, even minute differences in VMR should be highly significant (because the differences are so large compared to the magitude of the noise), it is advisable to perform a statistical test to confirm that assumption. A suitable test because of its high resistance to outliers is the non-parametric Wilcoxon-Mann-Whitney signed-rank test (Wilks, 1995). The application of this test to time series of zonal-mean concentrations reveals that e.g. the differences between Control and Zero are indeed all highly significant (i.e., they pass at the 1% level very easily), even though (as mentioned above) the shifts in the scatter plots do not look very dramatic. But due to the low standard deviations for the zonal mean fluctuations, VMRs that appear quite close in the scatter plots are in fact clearly drawn from different distributions as far as the test is concerned. Therefore, plots of the p values for these tests have not been shown here, because as far as the WMW test is concerned, all time series from the various runs are clearly different from each other.

Run with doubled meridional wind in the thermosphere

Figures 3.31 to 3.34 are scatter plots corresponding to Figures 3.16 to 3.19, except for a run with doubled meridional wind ("V-Sens"). This experimental setup should increase exchange of mass between the NH and SH and therefore tend to diminish meridional gradients.

Previous experiments (Doege *et al.*, 2008) with stronger wind fields than predicted by the GCMs had demonstrated that the meridional wind can reverse a VMR gradient if it is strong enough. In that study, C_2H_2, C_2H_4, and C_2H_6 in particular had their concentration maximum moved from where it would be purely because of photochemistry (in the Summer, SH) to the downwelling branch of the thermospheric circulation in the NH, which is not found in this study, where the meridional winds are about an order of magnitude less than previously assumed.

In general, VMR correlations with measurements decrease across-the-board when only the data for heights above 1,000 km is used. As expected, ethane is quite sensitive to v and the correlation becomes somewhat weaker. Propane shows a little more spread between the points close to the NP (the two lowest dots in Fig. 3.31b)—one measurement is on the day side, the other on the night side, so the effect of increasing v is more Northward transport on the day side and the reverse on the night side, thus the two points become more dissimilar in their VMRs in the V-Sens run.

For C_4H_2, a weakening of the meridional gradient is obvious, due to in increase in concentration at the NP by advection.

CH_3C_2H looks noticeably worse in this run than in Control, with the distribution becoming much too uniform globally. This is a strong indication that the relatively high wind speeds, which are still significantly less than those in Mueller-Wodarg (2003), in this experiment are clearly unrealistic.

For the remaining INMS-measured species, the differences are relatively subtle. Thus the main effects of increasing v appear to be a slight improvement of C_2H_6, but at the same time problems with CH_3C_2H. Consequently, the GCM-derived wind fields as they are implemented in the Control experiment will be treated as the basis for the later runs, as increasing v does not improve results sufficiently to warrant adjustments.

In this V-Sens run the meridional winds are still too low to effect major changes, compared to the significant, overriding impact of advection in the earlier study. The aim of this run is therefore more to serve as an upper bound for the circulation strength and to demonstrate that not all discrepancies between measurements and observations can be attributed to the uncertainty in the wind field, and that in fact a stronger meridional wind tends to make the correlations with measurements worse. As two very different GCMs for Titan's thermosphere exist at the time of writing (namely T-GITM by Bell, used here, and a GCM by Mueller-Wodarg), in which the meridional wind is either relatively weak (T-GITM) or quite strong (Mueller-Wodarg, 2008), Cassini INMS measurements can then be used to decide which model is more realistic. Based on the results in this study, it would seem that the T-GITM winds produce results better in line with observations. Mueller-Wodarg predicted strong winds above about 1,100 km height and vertical range of his model is 1,000 to 1,600 km, therefore his results are difficult to apply to his model. But it would seem that even the zonal-mean meridional wind of 20 m/s would still be too strong not to have an adverse effect on the distributions of species which are sensitive to the circulation.

3.3 Fitting observational data to a distribution function

One of the advantages of having a chemistry model of the thermosphere, however imperfect, is that it can help to understand the observations better. The relatively scarce Cassini INMS data points can be fitted to a function of one's choice, but

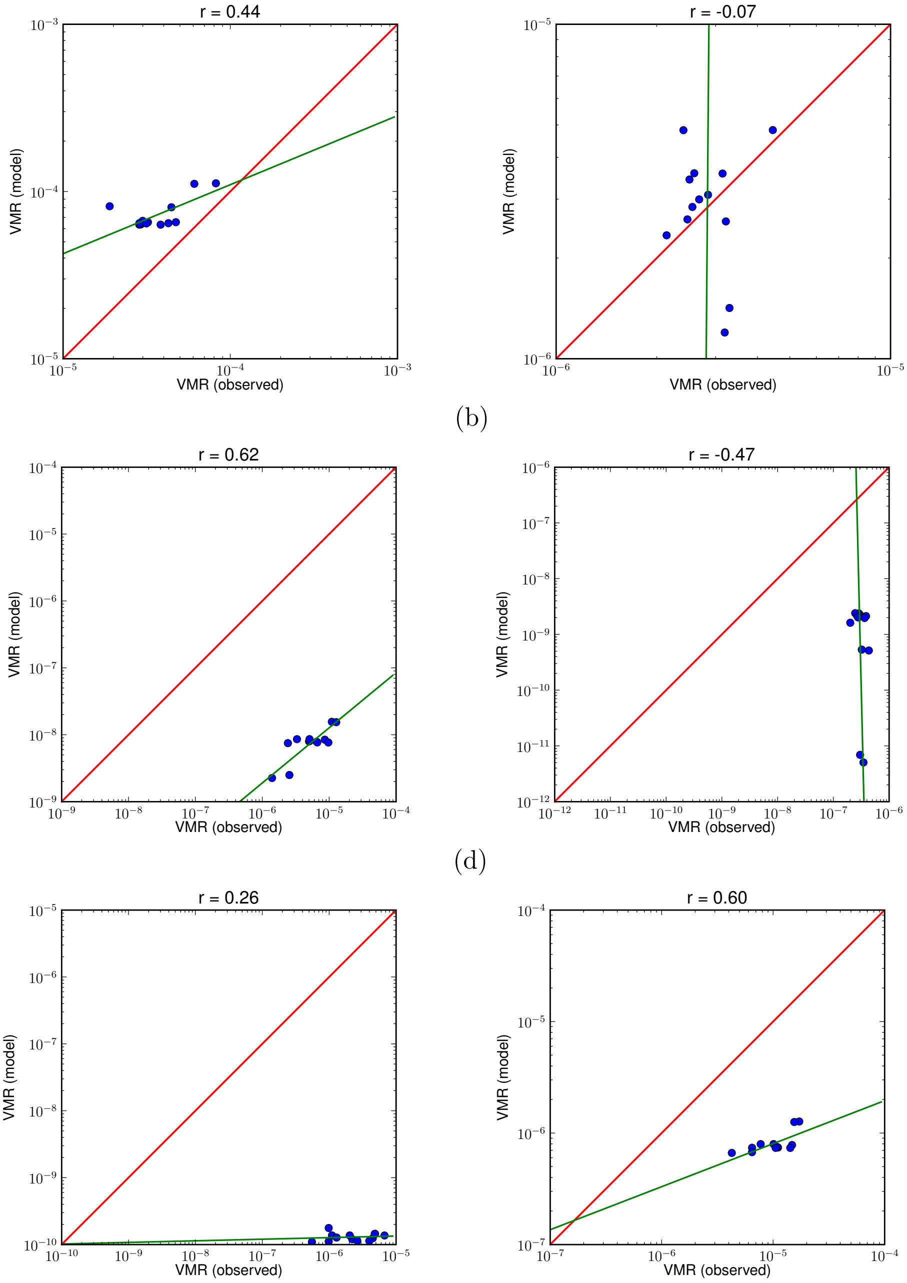

(a) (b)

(c) (d)

(e) (f)

Figure 3.31: Scatter plots comparing INMS measurements above 1,000 km altitude (horizontal axis) and corresponding MOZART values (vertical axis) from the V-Sens run for (a) C_2H_6, (b) C_3H_8, (c) C_4H_2, (d) C_4H_6, (e) C_6H_6, and (f) CH_3C_2H. The Spearman rank correlation and best-fit line (green) as well as the slope-one line (red) are also shown.

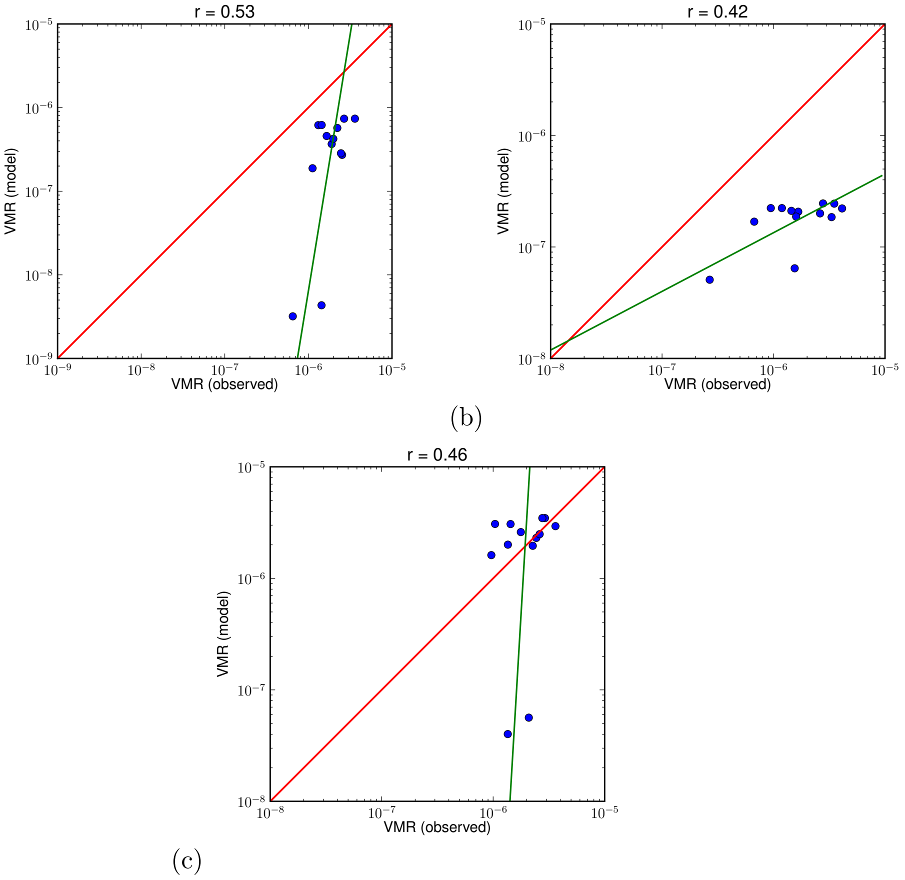

(a) (b)

(c)

Figure 3.32: Same as Fig. 3.31, but for (a) C_2N_2, (b) HC_3N, and (c) CH_3CN.

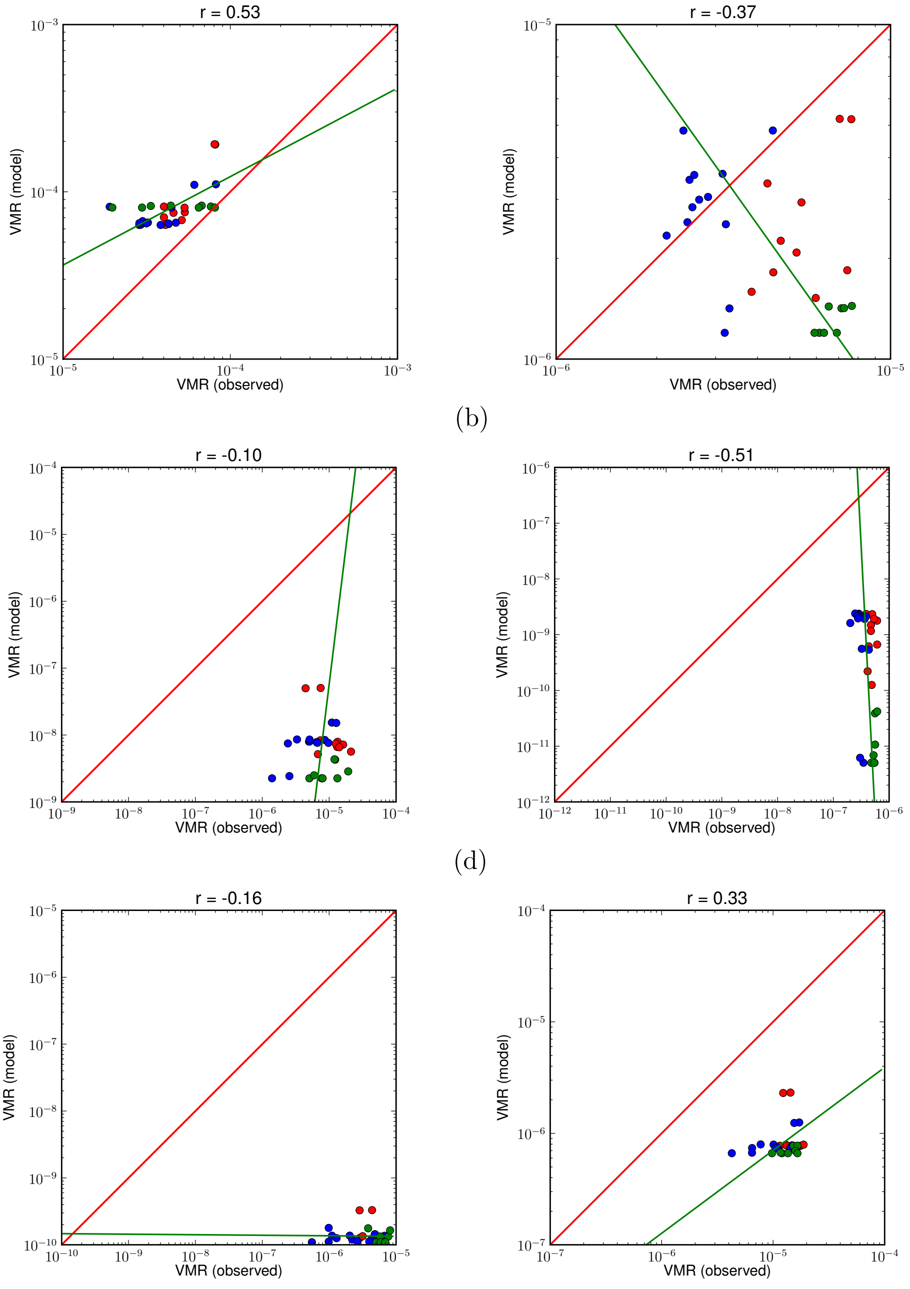

(a) (b) (c) (d) (e) (f)

Figure 3.33: Scatter plots comparing all INMS measurements (horizontal axis) and corresponding MOZART values (vertical axis) from the V-Sens run for (a) C_2H_6, (b) C_3H_8, (c) C_4H_2, (d) C_4H_6, (e) C_6H_6, and (f) CH_3C_2H. The Spearman rank correlation and best-fit line (green) as well as the slope-one line (red) are also shown. Data for heights above 1,000 km is colored blue, data for 975 km and below green, and data in between red.

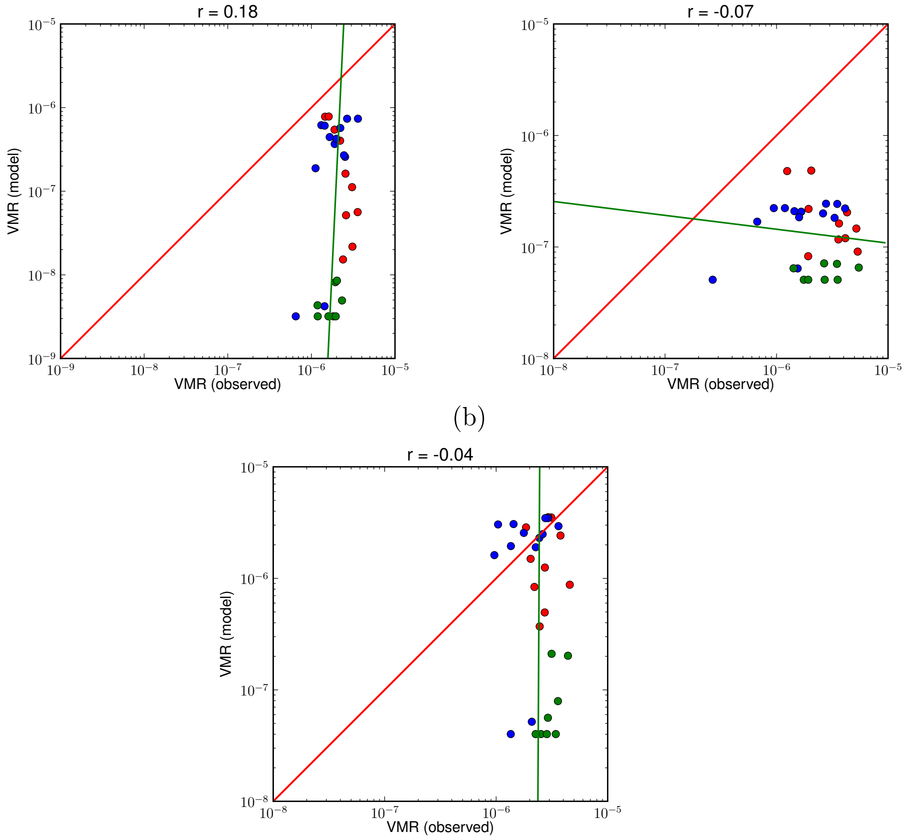

(a) (b) (c)

Figure 3.34: Same as Fig. 3.33, but for (a) C_2N_2, (b) HC_3N, and (c) CH_3CN.

without a model it is not clear which function could provide the best fit. Based on the species concentration plots shown in this chapter (Figures 3.4 to 3.14), it is proposed that a suitable function might be:

$$A \exp\left(-\chi^2/B\right) + C\Delta h + D = \log_{10} q$$

The first term is a Gaussian depending on the angle χ, which is defined as

$$\cos\chi = \langle r, r_0 \rangle$$

where r and r_0 are unit vectors pointing from Titan's center to the coordinates of an observation point or a reference point respectively, and the angle brackets denote the inner product. So the angle χ acts much like the Solar zenith angle, except that the location of this reference point (at LST λ_r and latitude ϕ_r) is also optimized for, with a first guess it being at the subsolar surface point. So in total there are six parameters that are fitted to the observations: A, B, C, D, λ_r, and ϕ_r.

The first term is a Gaussian shaped by the parameters A and B. The second term depends on the height anomaly Δh (departure of height from the reference height of 1,020 km), the third is a sinusoidal dependence on latitude ϕ, the fourth on Local Solar Time t to account for the effect of meridional transport, which goes towards the poles at daytime and back at nighttime. This fitting is done for the base-10 logarithm of VMR (which is called q here).

Fitting is done via conventional least-squares fit routines, with only data for heights above 1,000 km being used, as the effect of dynamics is least there. The observations can then be correlated with the values obtained from the simplified, fitted function, to see if such a simple distribution can approximate the observations reasonably well. The Spearman rank correlation is used again for its resilience. The respective p value for each correlation is also shown in the plots, although as mentioned before such statistical measures should not be considered overly reliable when the number of available data points is relatively small.

Table 3.4 gives some of the fitted parameters and Fig. 3.35 shows horizontal distributions for 1,000 km height. Unsurprisingly, the function fitting favors VMR maxima in the SH, where of course according to the MOZART results they would be expected to be. However, the fitted maxima are all situated before noon between 7am and 11am, whereas MOZART generally predicts maximum concentrations in the afternoon.

In general when fitting, there is always a risk of over-fitting, i.e. choosing so many terms in the fitting function that one gets a more or less perfect fit. In the

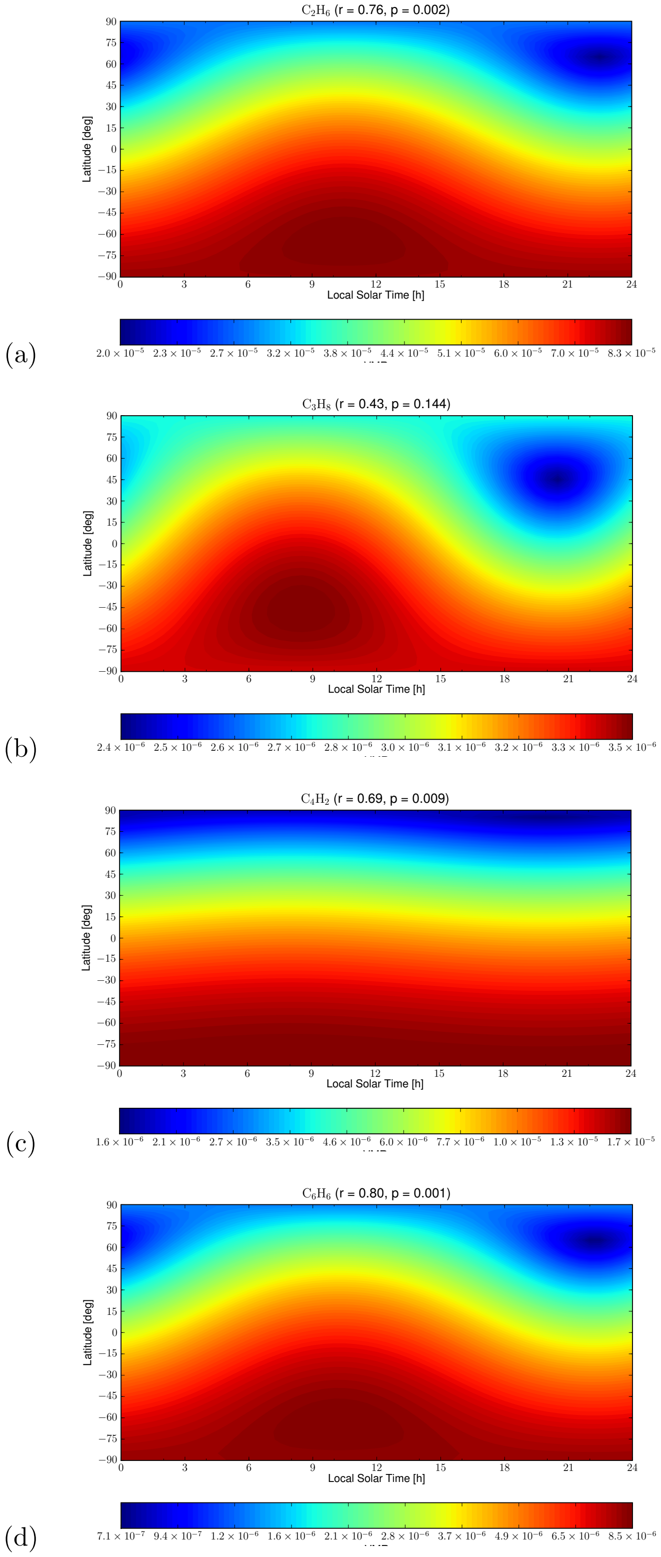

Figure 3.35: Least-squares best-fit horizontal distributions at 1,020 km height for (a) C_2H_6, (b) C_3H_8, (c) C_4H_2, and (d) C_6H_6 using data points for 1,000 km altitude and above.

Species	ϕ_r [°]	λ_r[h]
C_2H_6	-64	10.5
C_3H_8	-45	8.4
C_4H_2	-71	7.1
C_4H_6	-47	8.7
C_6H_6	-63	10.3
HC_3N	-73	10.5

Table 3.4: Best-fit VMR maxima locations for selected species.

case of N random data points, it is for example possible to perfectly represent them with a polynomial of degree $N - 1$ (i.e., a polynomial with N terms) or alternatively with N Fourier coefficients. The Fourier transform and the polynomial fit use terms that are orthogonal, that is, integrating the products of different terms over the entire domain gives zero. This makes them very efficient for approximation. If, as in this case, one devises a different fitting function, its terms are not necessarily orthogonal, but it is still a good idea to use fewer fitted parameters (N_p) than there are data points in the series (N), especially when of course the data is not random but somehow correlated. Here we use $N_p = 6$ for $N = 13$ samples, which still seems acceptable. But naturally including more data would be desirable. Therefore this analysis was repeated with all inbound observations ($N = 31$) to get a little more certainty about how much results depend on the N_p/N ratio and if there is over-fitting. The results for ethane proved to be quite reliable, but several of the other species showed an extreme drop in night-side concentrations.

The analysis was therefore redone with the familiar ODR technique (Fig. 3.36) instead of least-squares fitting. The rationale is that the main problem for fitting the the strong vertical gradient of the heavy species, coupled with the comparatively large uncertainty about Cassini's vertical position. Thus, ODR with its ability to deal more successfully with larger errors in more than one variable is also a good approach here. The ODR analysis confirmed that finding a good fit is more difficult if values below 1,000 km height are considered. Ethane and CH_3C_2H show very stable results that confirm the least-squares-based results, the other species are more problematic. The problem for the ODR analysis might be that the errors for the height and VMR are quite large, while the horizontal position is relatively well-known. Thus the ODR in trying to achieve a fit might "smear out" the horizontal information too much, while in reality it should mainly optimize for h and q. Thus it would be ideal to employ an optimization technique that allows more fine-tuning in this respect.

This section attempted to use the MOZART results to help in the interpretation of the Cassini observations. While the number of samples is quite small, it is

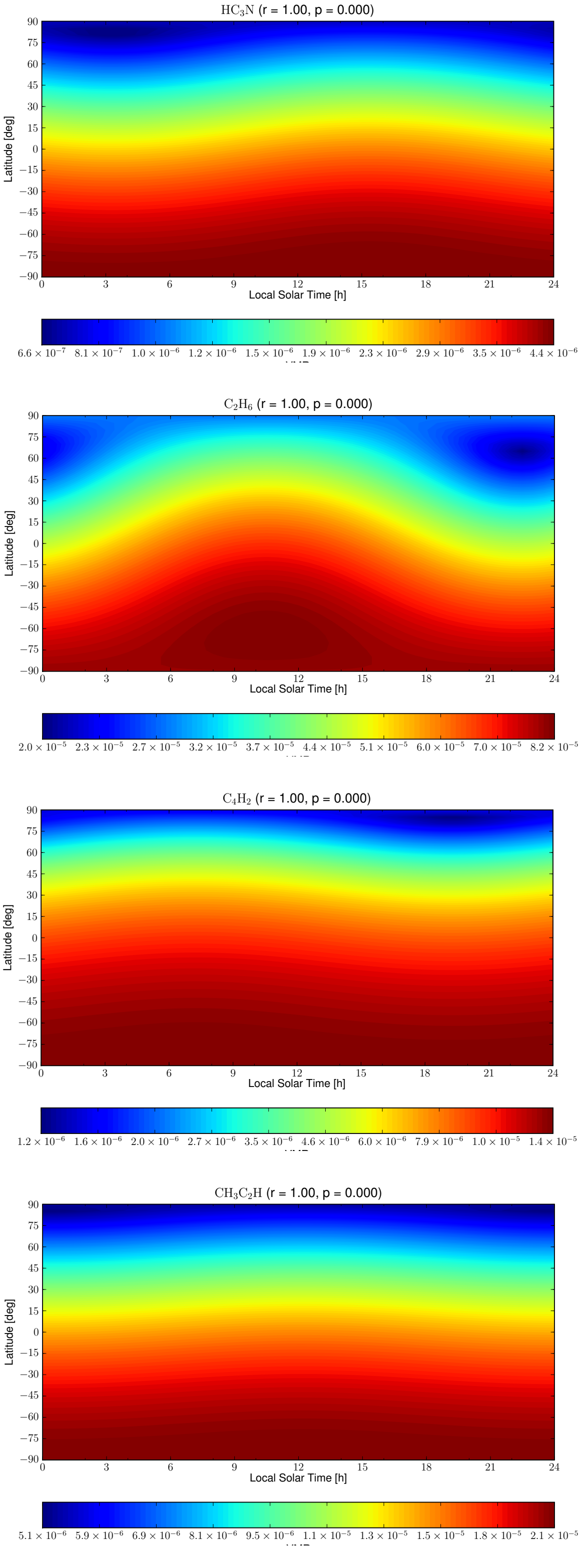

(a)

(b)

(c)

(d)

Figure 3.36: ODR best-fit horizontal distributions at 1,020 km height for (a) HC_3N, (b) C_2H_6, (c) C_4H_2, and (d) CH_3C_2H using data points for 1,000 km altitude and above.

still interesting if the optimization creates distributions that are broadly in line with model results. Better coverage of the SH with Cassini data might make this task considerably easier, as the fit would then be constrained in an area where most species have concentration maxima. But even the present limited data base allows to see that fit for the region above 1,000 km height are quite reasonable and provide some interesting results (e.g., the placement of the maxima before noon and the apparenly high agreement in the ethane distribution—specifically the location of the VMR maximum—between model and observations that was not evident from the previously-shown scatter plots) that are worth mentioning. All in all these Cassini retrieval analyses and the MOZART results tend to boost confidence in each other. It certainly demonstrates the usefulness of even an imperfect model (and ultimately *all* models are imperfect to some degree) for making conclusions from scarce measurements, especially in the case of Titan, where the few available measurements tend to also have large uncertainties.

3.4 Discussion

As the previous sections have demonstrated, the MOZART-based Titan model reproduces the 3–D distributions of the measured chemical species relatively well. The correlations are generally best for data above 1,000 km altitude, as photolysis and molecular diffusion are very dominant processes there, while meridional transport is too slow to affect most species strongly. Below 1,000 km altitude, the GCM wind field, particularly in the meridional direction, becomes more relevant and an over- or underprediction of v affects the distributions more strongly. Some species like ethane are more sensitive to v, while e.g. HCN shows very low sensitiviy there.

Major discrepancies between model and observations could also be observed where problems and uncertainties with the INMS retrievals existed (esp. for C_4H_6). Besides uncertainty about the measurements for some species, the very limited number of measured species also presents a problem for modeling Titan's chemistry. Knowledge of photochemically important intermediate species, like CH and CN, would be extremely helpful for a better understanding of the differences between model and observations. Unfortunately, measurements tend to be limited to the heavier species, so that in effect only the end products of Titan's complex chemical chain have been observed, and it is somewhat up to speculation which chemical pathway exactly was taken to form e.g. benzene.

Similar problems exist for the wind field—while the magnitude of the thermospheric jet stream is known, the meridional circulation can only be inferred indirectly. In that sense the T-GITM model also has been validated by these results, because the chemical distributions seem to be in best alignment with observations for relatively low v winds, as predicted by T-GITM.

All in all, the model is considered to be correct enough in comparison to observations to allow tackling additional scientitic questions with it, which will be addressed in the following chapter.

Chapter 4

Science questions

4.1 What is the influence of solar variability on chemistry?

The Solar cycle (see Fig. 2.2) can affect chemistry in three ways:

Firstly, via the considerable variation in ultraviolet radiation output, since ultraviolet radiation drives photochemistry. At Solar maximum, photolysis rates are therefore higher than at Solar minimum, leading to increased production of methane and molecular nitrogen photolysis products. However, photolysis of these products is also increased, and that is why it is not a priori clear whether a given species VMR would be correlated or anticorrelated with Solar UV output.

Secondly, Solar input drives the dynamics of Titan's atmosphere, as it does those of Earth. Larger equator-to-pole temperature gradients would create a stronger jet stream and Hadley circulation.

Thirdly, many reaction rates are highly temperature-dependent, so an increase in thermospheric temperature in the case of Solar maximum (and the reverse for Solar minimum) can shift the importance between reactions, so that a chemistry pathway that is very dominant at high temperatures will be relatively unimportant at lower temperatures. Since photolysis is assumed not to be impacted by temperature, it is generally expected that lower temperatures will make photolysis reactions more dominant and extend the zone in the upper thermosphere where photolysis is the primary avenue for chemistry.

Estimating the impact of the Solar cycle on winds and temperatures is more complicated, as the available measurements only cover a small part of the Solar cycle and as thermospheric temperatures are strongly influenced by upward-propagating gravitational tidal waves. It is therefore necessary to rely on GCM simulations as a guide (Bell, 2008). The less controversial feature of those simulations is the expected dependence of zonal-average temperature with Solar radiation output. The amplitude is expected to be about 15–20 K in the cited work.

More questionable is whether the GCM correctly simulates the trend in meridional circulation: Both the Solar minimum and the Solar maximum case show a breakdown of meridional overturning, particularly for Solar maximum conditions. Bell considers the idea that this trend could simply be an artifact of zonal averaging, but the TEM circulation mirrors the trend, so it is concluded that this breakdown is real within the confines of the GCM, which does not necessarily mean it corresponds to the real behavior of Titan's atmosphere. However, since the impact of meridional circulation is not particulary big, this is not seen as a major problem.

For these studies, the control run wind and temperature fields were modified as follows: The v winds above 350 km altitude were multiplied with a factor derived from zonal means of the GCM, while temperatures were increased and decreased using global-average models profiles. The temperature increase between Solar Min and Solar Max is shown in Fig. 4.3 and the wind fields in Figures 4.1 and 4.2.

One possible explanation would be that at Solar maximum, ion drag in the thermosphere becomes so strong that it acts as a brake on the meridional circulation. The Solar minimum drop in the strenth of overturning on the other hand would simply be a result of a lower temperature contrast between EQ and pole due to less Solar UV output. But in the absence of a detailed analysis of the GCM output by the experimenter, this is hard to say. But since these simulations are so far the only study on the impact of Solar output on thermospheric circulation, they must be taken as the truth for now, as competing model studies do not exist at this point.

As the circulation at Solar max and Solar min, according to T-GITM, is weaker than in the Control case, the behavior should be similar to a mix of the Control and Zero runs, except that the changed photolysis coefficients and raised or lowered temperatures, through their effect on reaction rates, will have an impact on chemistry.

One issue with the chemistry reaction rates for Titan is that many of them are extrapolated based on lab measurements at much higher temperatures. So going to even lower temperatures may exacerbate the problems with these rates by introducing much larger changes in the rate constant than would be realistic and even de-stabilizing the chemistry scheme.

The impact of the Solar cycle on Titan's thermospheric temperatures might be overpredicted, or at least so far a Solar cycle-based trend in available Cassini temperature measurements has not been identified yet. Therefore, in these

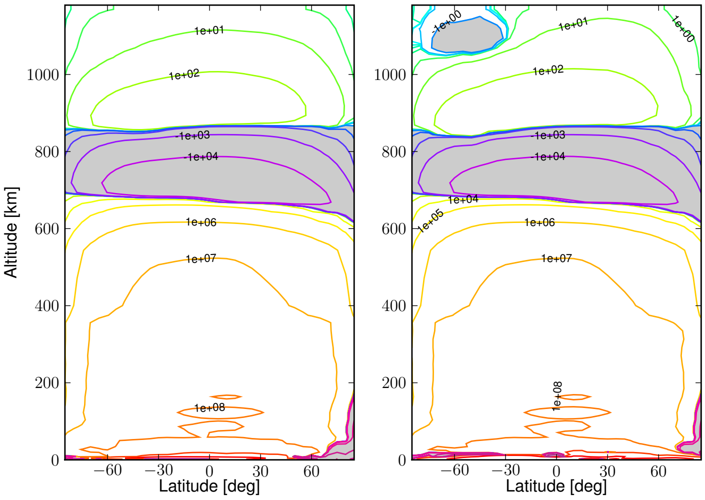

Figure 4.1: Zonal average (left panel) and transformed Eulerian Mean (TEM) circulation (right) for Solar maximum, both in kg/s.

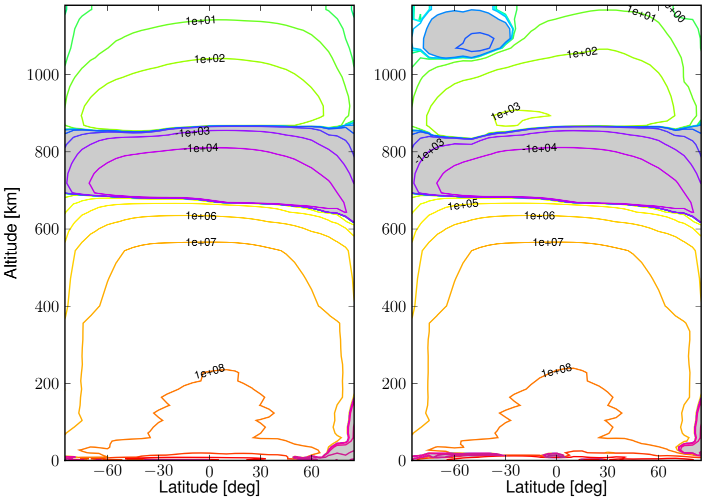

Figure 4.2: Zonal average (left panel) and transformed Eulerian Mean (TEM) circulation (right) for Solar minimum, both in kg/s.

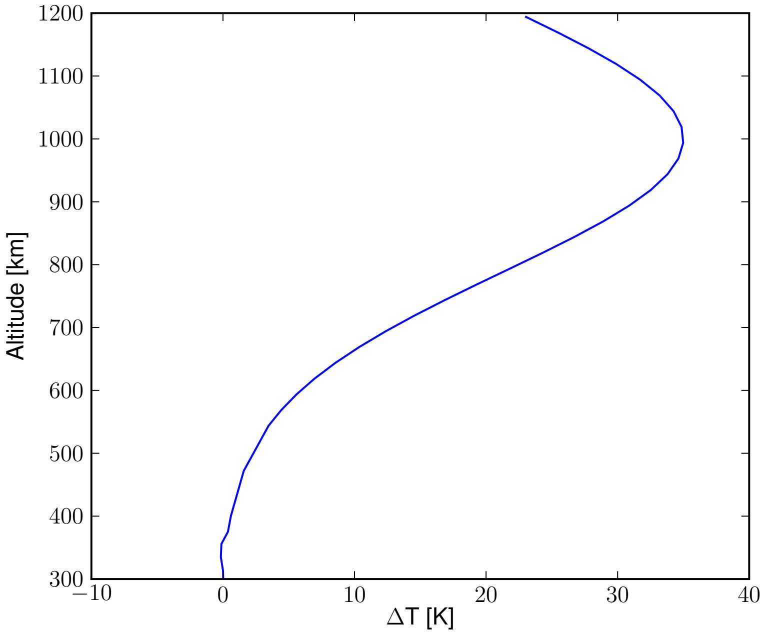

Figure 4.3: Average change in temperature from Solar Min to Solar Max. Maximum warming occurs at around 1,000 km height.

experiments the effect of the Solar cycle will mainly come from temperature dependence and photolysis rates, while the changes in advection will be secondary.

The Cassini measurements span a time period from about Solar average to Solar minimum (see Introduction), thus the Solar minimum case is of particular importance here, as it could provide a better fit to observations than Solar average (i.e., Control).

4.1.1 Solar minimum run ("SolMin")

First, the familiar scatter plots are shown as in the previous chapter to allow easy comparison between model results and measurements. Obviously, several of the measured species are very strongly affected by the changed experimental conditions, others negligibly. In the former group are C_2H_6, C_3H_8, C_4H_2, and CH_3C_2H.

Ethane (C_2H_6, Fig. 4.4a)

Ethane shows a relatively strong (-0.62) anti-correlation with measurements, although most points in the scatter plot are clustered so tightly that the best-fit line is strongly influenced by the four outlier points. Compared to the Control experiment, the model now produces much higher ethane concentrations in excess of the measured maximum VMR of 10^{-4} as obtained from measurements.

Propane (C_3H_8, Fig. 4.4b)

Propane is changed strikingly, with its VMR being about a factor of ten higher on the day side than measurements in SolarMin. This overall increase in concentration also means that the previous polar outliers are now very much in line with measurements, but clearly less VMR variability in the model would be desirable, which is not the case in SolarMin. Propane's primary thermospheric production reaction, $C_2H_5 + CH_3 + M \rightarrow C_3H_8 + M$, increases about tenfold, therefore the similar increase in propane concentrations. Both ethane and propane are influenced by the same mechanism, an increase in CH_3 VMR above about 900 km height in SolarMin. CH_3 chemistry is quite complex in the model, with many reactions determining its production and loss, so it is difficult to pinpoint a specific mechanism, however the main thermospheric loss reaction $N + CH_3 \rightarrow H_2CN + H$ does decrease slightly at SolarMin, which could explain a resulting higher CH_3 VMR, being then ultimately due to lower availability of the photolysis product atomic nitrogen N.

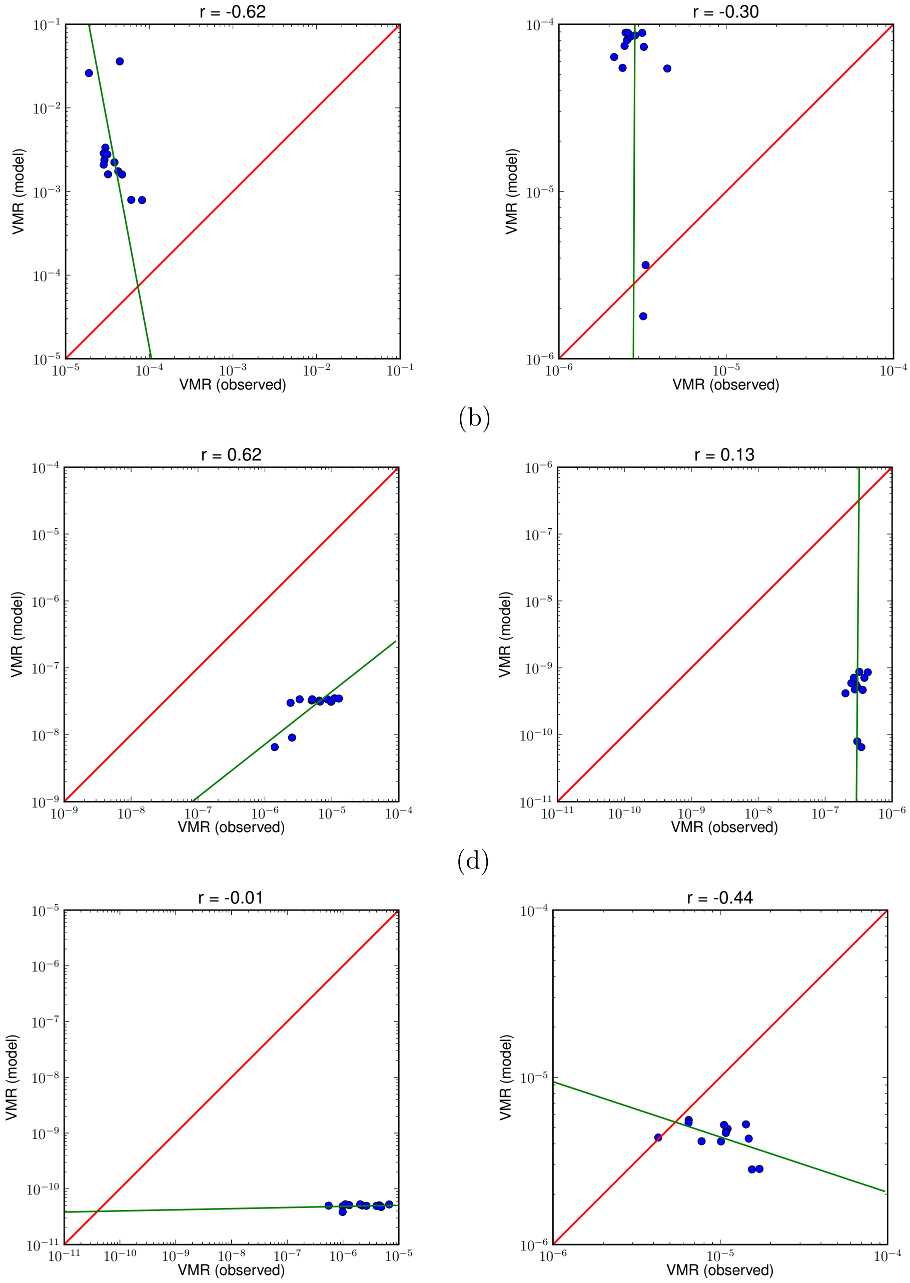

(a) (b) (c) (d) (e) (f)

Figure 4.4: Scatter plots comparing INMS measurements above 1,000 km altitude (horizontal axis) and corresponding MOZART values (vertical axis) from the SolMin run for (a) C_2H_6, (b) C_3H_8, (c) C_4H_2, (d) C_4H_6, (e) C_6H_6, and (f) CH_3C_2H. The Spearman rank correlation and best-fit line (green) as well as the slope-one line (red) are also shown.

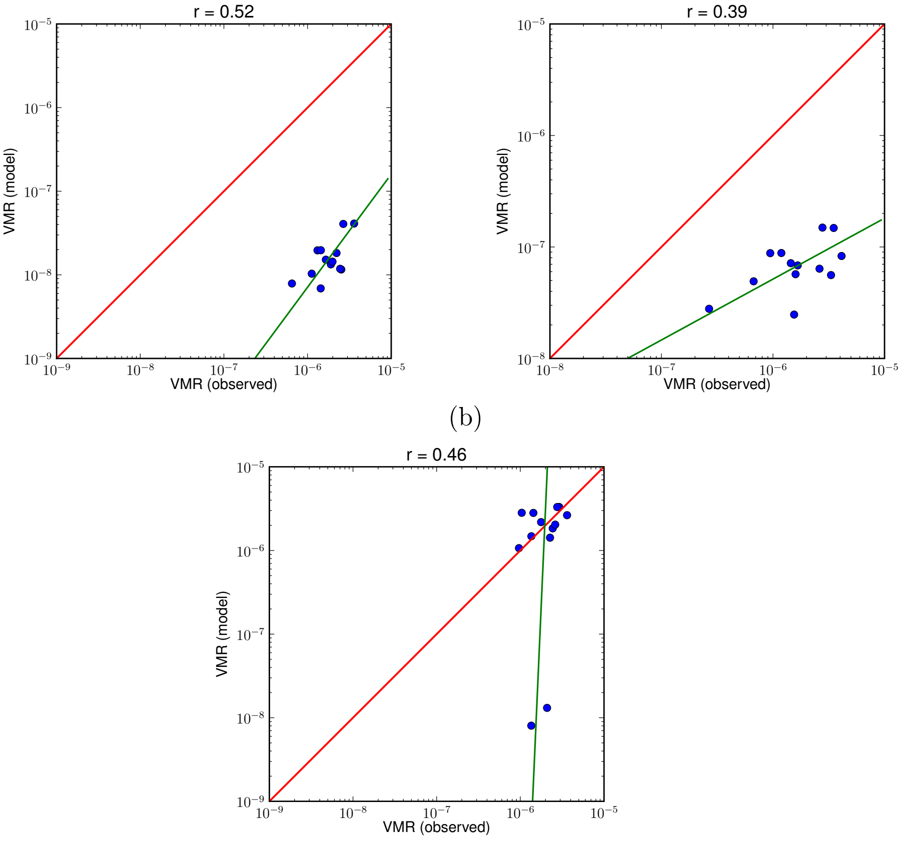

(a)

(b)

(c)

Figure 4.5: Same as Fig. 4.4, but for (a) C_2N_2, (b) HC_3N, and (c) CH_3CN.

Diacetylene (C_4H_2, Fig. 4.4c)

Diactylene concentrations are slighty improved under Solar Min conditions—the correlation stays the same at 0.62 but VMR increases by about a factor of 3 to 4 which brings model values closer to observations. Still, the change is not dramatic and model values still fall somewhat short of measurements.

1,3-butadiene (C_4H_6, Fig. 4.4d)

The overall variability of this species decreases in this experiment. This is of interest because the measurements show very low variability, and although those INMS retrievals only represent relatively uncertain upper bounds on C_4H_6 VMR, it is possible that this heavy species should indeed have considerably smaller differences in thermospheric VMRs than the Control run indicates.

Benzene (C_6H_6, Fig. 4.4e)

Benzene concentrations diverge from the measured concentrations more strongly than in the Control experiment and variability in the model is even lower. Clearly benzene production is even lower during Solar minmum conditions and the resulting concentration is affected by that. Low variability in the model is the reason that correlation decreases from 0.26 in the Control experiment to -0.01 in this run.

Methylacetylene (CH_3C_2H, Fig. 4.4f)

CH_3C_2H concentration is slightly surprising—a species strongly associated with Titan's summer pole, which makes it not immediately clear why its VMR would *increase* in concentration in response to less Solar EUV input. CH_3C_2H is mainly formed in the thermosphere by $CH + C_2H_4$ and destroyed by photolysis. Comparison of production and loss profile for Control and Solar Min shows that the production reaction increases above a height of about 900 km. Both CH and C_2H_4 are more abundant at Solar minimum conditions, leading to increased production of methylacetylene.

Cyanogen (C_2N_2, Fig. 4.5a)

Cyanogen VMR is different from Control in the sense that the low-VMR outliers no longer exist; instead all values are now clustered together at a lower concentration. Correlation stays almost the same (0.52 vs 0.53). While elimination of polar outliers is in itself desirable, clearly the lower Solar output leads to less production of cyanogen. The two outliers in Control could be improved by higher cyanogen produciton near the NP which is not affected by Solar output but by enhanced mixing from the middle latitudes.

Cyanoacetylene (HC_3N, Fig. 4.5b)

Cyanoacetylene VMR also drops slightly, which removes the outliers which were clearly separate from the main cluster of data points in Control. Correlation decreases slightly from 0.42 to 0.39.

Acetonitrile (CH_3CN, Fig. 4.5c)

Aceteonitrile shows very little dependence on Solar outpout. Concentrations decrease slightly which does seem to provide a slightly improved fit with observations, although the rounded correlation coefficient stays at 0.46. It is interesting to note that acetonitrile is almost unaffected by Solar output. Production and loss rate profiles show that loss through $CN + CH_3CN \rightarrow C_2N_2 + CH_3$, which is slightly dominant above 1,100 km height in Control, does decrease substantially, while the major production reaction, $N(^2D) + C_2H_4 \rightarrow CH_3CN + H$ shows very little change. But the most important loss reaction, $CH_3CN + H \rightarrow CN + CH_4$, is hampered by the fact that the atomic hydrogen profile is kept fixed. Therefore, the fact that acetonitrile changes so little might be mainly the result of model assumptions.

Overall, the Solar Minimum run produced mixed results. Some species, particularly those that were already quite well in line with measurements in the Control experiment, improved further, while problem species in the Control run showed either little change or even less similarity to Cassini data. Propane and ethane increased in concentrations, driven by higher availability of CH_3, but particularly in the case of propane overall VMR variability in the model remained higher than measured. This suggests that while consideration of the Solar cycle can improve the fit with measurements, it does little to counteract problems caused by the underlying chemistry scheme. As with tuning the chemistry scheme itself, changing Solar irradiance may improve some parts of the model while at the same time leading to problems elsewhere in the chemistry.

4.1.2 Solar maxium run ("SolMax")

The Solar maximum is more speculative because no corresponding Cassini measurements exist for those conditions. On the other hand, rate constants here are actually closer to lab measurements, because the temperature is higher, so at least as far as rate constants are concerned, one is generally on safer ground here than when lowering temperatures even further.

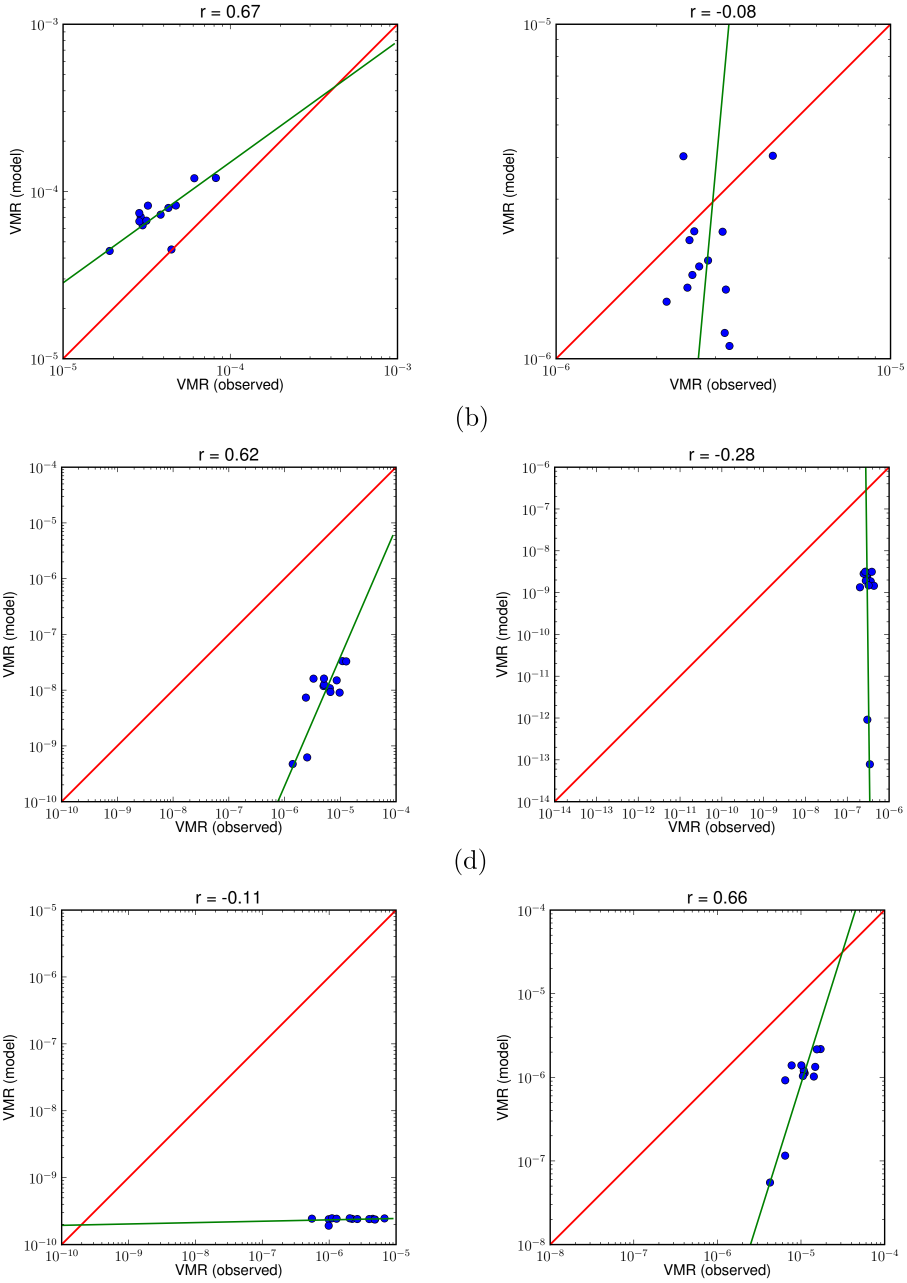

(a) (b) (c) (d) (e) (f)

Figure 4.6: Scatter plots comparing INMS measurements above 1,000 km altitude (horizontal axis) and corresponding MOZART values (vertical axis) from the SolMax run for (a) C_2H_6, (b) C_3H_8, (c) C_4H_2, (d) C_4H_6, (e) C_6H_6, and (f) CH_3C_2H. The Spearman rank correlation and best-fit line (green) as well as the slope-one line (red) are also shown.

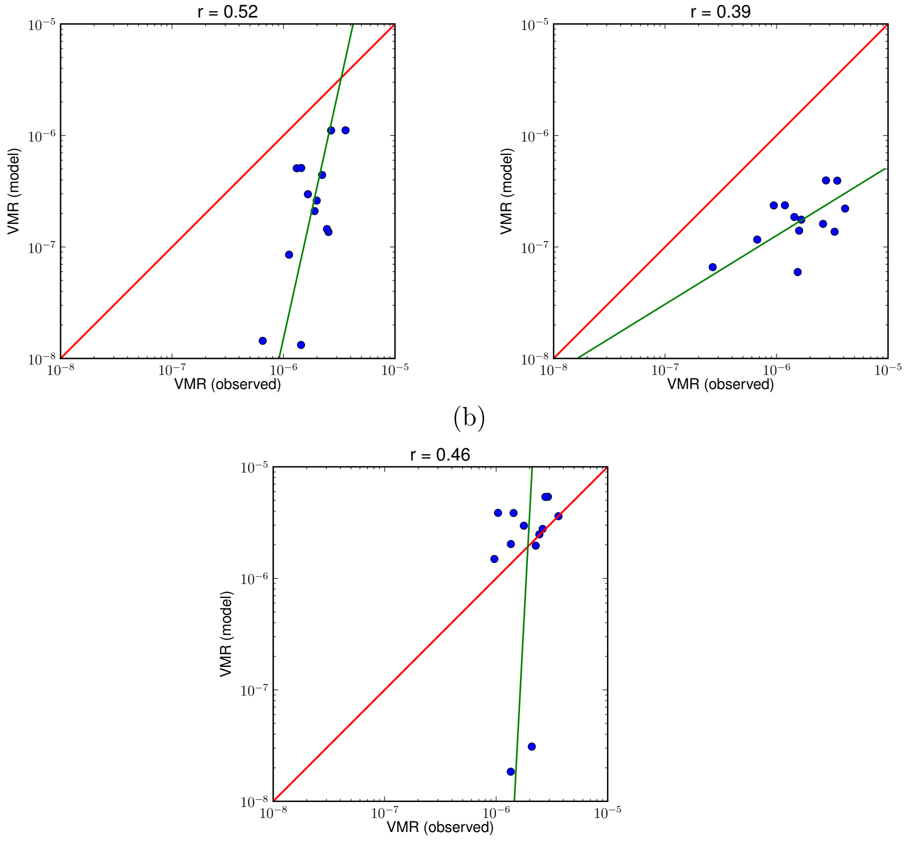

(a)

(b)

(c)

Figure 4.7: Same as Fig. 4.6, but for (a) C_2N_2, (b) HC_3N, and (c) CH_3CN.

Ethane (C_2H_6, Fig. 4.6a)

Ethane shows more variability during Solar Max than Control, increasing its correlation with measurements from 0.44 to 0.67. In the zonal average, the NP region turns from a weak production region of ethane (except above 1,100 km altitude) to a net loss region above 800 km height. The result is that in the Solar Max run, the global zonal-average minimum VMR exists in the NP region above 1,050 km height, which is where the two low-VMR points in the scatter points are located on Titan. The reason for this ethane depletion is that ethane production via $CH_3 + CH_3 + M \rightarrow C_2H_6 + M$ decreases sharply in Solar Max compared to Control, which is important because at the NP, there is not enough Solar input for photolysis of propane to be a major source of ethane as it is elsewhere. (Similarly, the reaction $NH + C_2H_5 \rightarrow C_2H_6 + N$, which is dominant elsewhere on Titan for ethane production over about 900 km altitude, is insignificant at the NP as there is too little photolysis to produce the required NH.) Zonal-average CH_3 VMR drops by about an order of magnitude at the NP compared to Control, therefore little ethane is produced in this way. The reason for this CH_3 depletion at the NP is the almost complete depletion of $^1CH_2$ at the NP in the Solar Max experiment (Fig. 4.8), which in turn causes a sharp drop in the reaction $^1CH_2 + CH_4 \rightarrow CH_3 + CH_3$ above a height of about 800 km, corresponding well with the Solar Max ethane loss region.

Propane (C_3H_8, Fig. 4.6b)

Propane does not look substantially different than in Control—its VMR decreases slightly below measurements, so the previous two outliers from the Control experiment are less detached from the main cluster of data points. Only a single point shows a higher VMR than in measurements.

Diacetylene (C_4H_2, Fig. 4.6c)

Correlation for diacetylene stays unchanged at 0.62, but the two polar outliers have slightly lower concentrations than during the Control run.

1,3-butadiene (C_4H_6, Fig. 4.6d)

C_4H_6 concentrations are clustered more closely together in the plot than in Control and the anti-correlation is lessened.

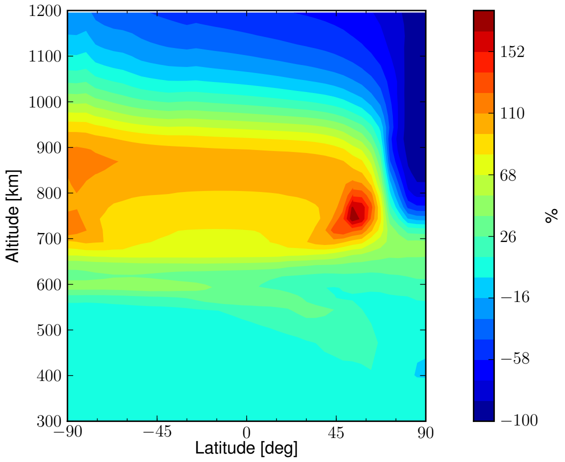

Figure 4.8: Percentual change in zonal-average concentration between Solar Min and Solar Max for $^1CH_2$.

Benzene (C_6H_6, Fig. 4.6e)

During Solar maximum, benzene production is heightened and VMR increases. Still, correlation with measurements becomes slightly negative, but this appears to be only the results of a single low-concentration outlier. Overall, benzene still has far too little variability in the model.

Methylacetylene (CH_3C_2H, Fig. 4.6f)

CH_3C_2H correlation increases from 0.60 to 0.66, but maximum VMR stays relatively unchanged. The main difference is a decrease of VMR to below 10^{-7} at two points.

Cyanogen (C_2N_2, Fig. 4.7a)

Minimum cyanogen VMR increases slightly, which is an improvement over the Control run. Where the Control experiment comparison had two distinct clusters of data, one between 10^{-6} and 10^{-7} and the other below 10^{-8}, the points are more evenly distributed in Solar Max.

Cyanoacetylene (HC_3N, Fig. 4.7b)

Cyanoacetylene correlation stays almost constant (0.39 vs 0.42) and the outliers are not as far removed from the main cluster.

Acetonitrile (CH_3CN, Fig. 4.7c)

As in the Solar Min run, Acetonitrile shows almost no effect of Solar output on its concentration.

All in all, the Solar Max run mainly brings an improvement for ethane, while other species show smaller changes. Both the Solar Min and Max runs have slightly less pronounced NP outliers, although in some cases that is the result of the main cluster moving towards the outliers in the diagrams, rather than the reverse. Since no Cassini measurements from Solar maximum conditions were available for this study yet, results from Solar Max should be seen more as a sensitivity experiment because drawing a meaningful comparison with measurements is more difficult than for Solar Min.

4.1.3 Relative changes between Solar minimum and maximum

Percentage changes from Solar minimum to maximum (Fig. 4.9) tend to show opposite behavior for the thermosphere and the rest of the atmosphere. Methane VMR (Fig. 4.9a) decreases above 1,000 km altitude, but increases slightly below that height, particularly at the SP. The enhanced photolytic destruction in the thermosphere because of the higher amount of EUV radiation received from the Sun explains the decrease, the increase at the SP is more difficult to understand. This is possibly because one methane loss reaction, $CH_4 + CH \rightarrow C_2H_4 + H$, is less active at heights between about 600 and 800 km in the Solar Max case, also leading to less production of ethylene. Indeed ethylene (Fig. 4.9b) shows a decrease in VMR, particularly near the NP, but an increase in a sloping region between about 600 km and 400 km height. More ethylene in that region causes depletion of CN (by about 30 to 40%) and an increase in C_2H_3CN (by about 40 to 60%), because the reaction rate for $CN + C_2H_4 \rightarrow C_2H_3CN + H$ increases. The reasons for the ethylene increase is harder to pinpoint and appears to be the results of many smaller reaction rates adding up. CH VMR is increased by about 30 to 50% in the region of interest and this would lead to higher ethylene production via $CH + CH_2 \rightarrow C_2H_4 + H$, but other reactions may also be involved.

The change in ethane (Fig. 4.9c) is dominated by strong depletion in the thermosphere, especially near the NP. Below 600 km altitude on the other hand there is a slight increase in VMR.

C_2N_2 (Fig. 4.9d) is very strongly increased in the high thermosphere. This is because production via $CN + CH_2CN \rightarrow C_2N_2 + CH_2$ increases so that in the Solar Max case it rivals the usual dominant production reaction in the thermosphere ($N + CHCN \rightarrow C_2N_2 + H$).

HCN (Fig. 4.9e), and even more so HC_3N VMR (Fig. 4.9f), increase quite significantly in ther entire thermosphere.

When compared to observations, it seems that the changes in chemistry between Solar minimum and Solar maximum, e.g. for C_2N_2 and HC_3N, bring the model closer to observations, by increasing the concentrations of these constituents. So while it had been expected that setting the model to Solar minimum conditions would improve the match with observations (because this would correspond better with the actual Solar activity during the measurements), the finding is that increased photolysis and temperatures—and therefore reaction rate coefficients—improve results. This could mean that the photolysis cross sections and quantum yields are underestimated or more likely that the assumed temperature-dependence of reactions tends to make reaction rates too low. It is also possible that the effect of heterogeneous chemistry on atomic hydrogen concentration could drive changes in many species. Molecular hydrogen (not shown) decreases by up to about 40% in the thermosphere at Solar maximum compared to Solar minimum, so if atomic hydrogen were allowed to adapt in the model, it might also change and the rest of the chemistry would react to that. (On the other hand, higher temperatures in the thermosphere might cause a decrease in heterogeneous reaction rates, thereby reducing heterogeneous atomic hydrogen loss.) Clearly making atomic hydrogen a variable species in the model would be of interest if the scheme would continue to be stable.

4.2 How do gravitational tides affect composition?

Temperature fluctuations measured by the descending Huygens probe were the first confirmation of the existence of strong tidally-induced temperature perturbations in Titan's thermosphere. Between about 500 and 1,020 km altitude, Fulchignoni *et al.* (2005) found fluctuations of up to about 20 K amplitude and 200 km vertical wavelength at 1,000 km height. 1–D modeling efforts (Strobel, 2006) for the Huygens landing site have confirmed that these strong perturbations can indeed arise purely as the result of upward propagation of tides, with their associated increase in amplitude as they travel upwards.

There are two kinds of tides on Titan: a gravitational tide caused by the

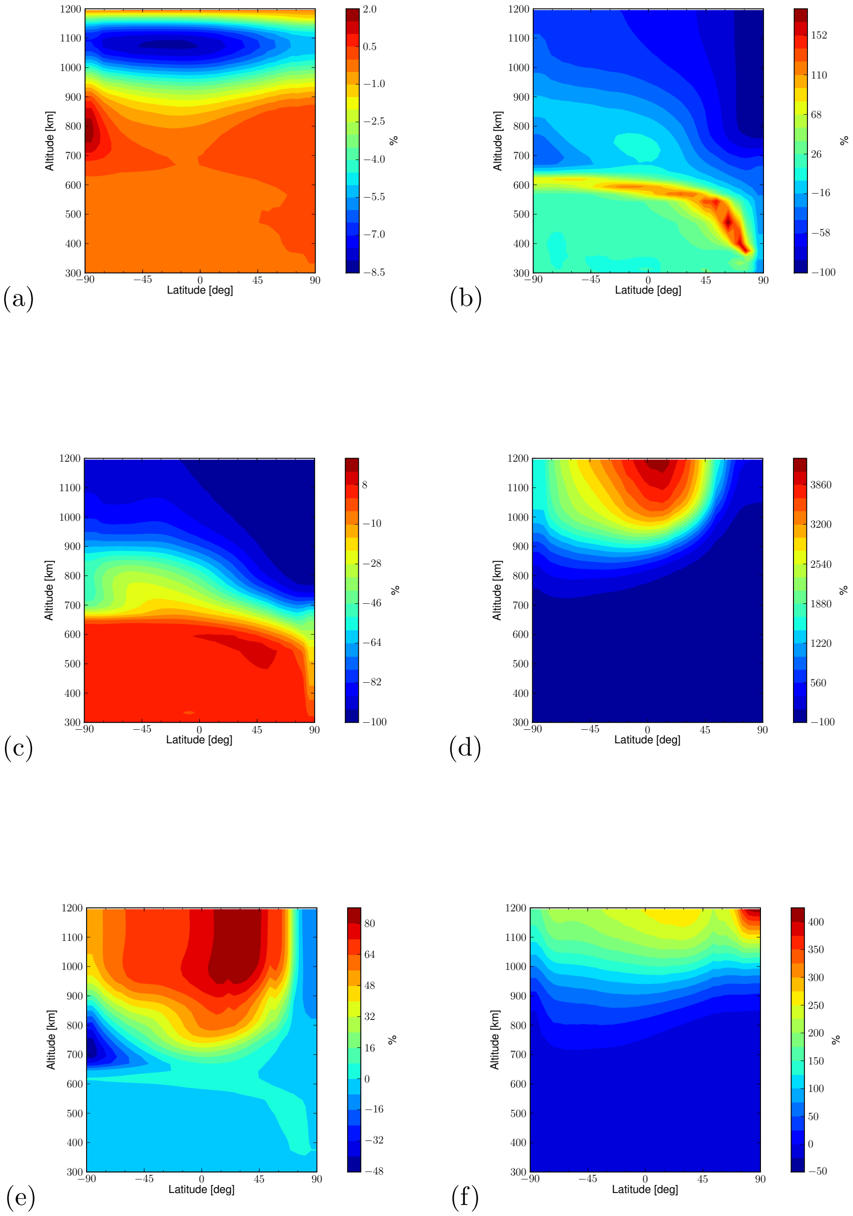

(a) (b) (c) (d) (e) (f)

Figure 4.9: Percentual changes in zonal-average concentrations between Solar Min and Solar Max for (a) CH_4, (b) C_2H_4, (c) C_2H_6, (d) C_2N_2, (e) HCN, and (f) HC_3N.

eccentricity of Titan's orbit around Saturn, and a radiative tide due to differential heating by the Sun. This section concerns itself with the former kind of tide.

Because the atmospheric mass is mainly contained in the troposphere and stratosphere, it is there that the gravitational tide is most strongly forced, although tidal forcing occurs in the entire atmospheric column. The resulting wave travels upwards, so that the total effect of the gravitational tide is a gravitational tidal wave, which is the sum of the upward-propagating wave and the local forcing.

As the wave moves upward, it is damped by critical layers, where $\bar{u} - c$, with $\bar{u}$ the zonal-average zonal wind and c the phase speed of the wave, approaches zero. I.e., a layer of eastward-moving wind will tend to dampen an eastward-propagating wave more than a westward-propagating wave. (This is similar to the stratospheric damping of waves that force the tropical Quasi-Biennial Oscillation [QBO] on Earth.)

The eastward-propagating $s = +2$ mode is forced seven times stronger than the westward-propagating $s = -2$ mode (Tokano, 2002), but this relationship does not necessarily indicate the likeliest wave pattern in the thermosphere, due to the damping effect of critical layers (Darrell Strobel and Jeffrey Forbes, pers. comm.).

Unfortunately, the exact shape of the gravitational tidal wave in the thermosphere is currently unknown. The 3–D structure depends on the latitudinal extent of critical layers that dampen the wave as it travels upwards. Therefore it is difficult to say whether the $s = 0$, $s = +2$, or $s = -2$ mode would be dominant. In the present experiment, the $s = 0$ mode was picked, with a maximum at the equator and a decrease towards to poles with the cosine of latitude.

The vertical wavelength and amplitude of the disturbance, since it depends on the zonal wind field, is also difficult to know. Here, average values from the Strobel (2006) 1–D study were used, but it is clear that it would be preferable to get better estimates from a model that uses the full zonal-average wind field to determine vertical propagation of the gravitational tidal wave. Unfortunately, such a study has not been conducted yet, and given the high degree of uncertainty about the wind field itself, would in all likeliness also contain a considerable margin of error. (I.e., simulations for several possible wind fields would have to be done to obtain upper and lower bounds on tidal amplitude and vertical wavelength.)

The resulting concentrations show a clear effect of the temperature wave on many species: Figures 4.10 to 4.13 show VMRs and temperatures to two opposite phases of the wave (i.e., about 8 Earth days apart). Methane (Fig. 4.10) and C_3H_5 (Fig. 4.12) VMR are positively correlated with T, while ethane (Fig. 4.11) and propane (Fig. 4.13) are negatively correlated, as are most of the other

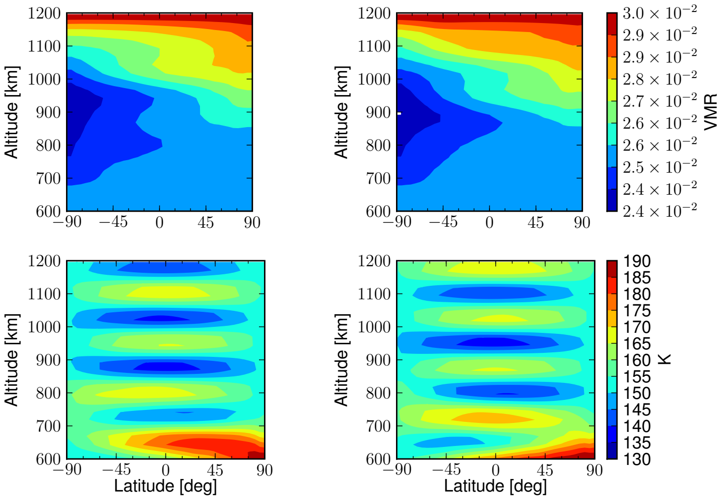

Figure 4.10: CH_4 zonal-mean VMR (top panels) and temperatures (bottom panels) for two opposite phases of the wave.

species not shown here. Table 4.1 lists some of these correlation coefficients. Propane and ethane are also affected enough that their global-average profiles show the vertical wave signature (Fig. 4.14).

Percentual changes (i.e., time-maximum minus time-minimum concentration divided by time average times 100) are relatively robust for several species (Fig. 4.15). First of all, methane (Fig. 4.15a) is affected, symmetrically around the equator at around 1,000 km height and also around 1,100 km height. This bimodal distribution of the differences is somewhat surprising, as the amplitude of the temperature signal increases with height, but otherwise the wave does not affect layers selectively. Several of the heavier species also have two maxima of impact, perhaps partly due to change in methane itself: Particularly ethane (Fig. 4.15b) looks similar, although the change is much bigger (34%) than it is for methane (4.5%).

Propane (Fig. 4.15c) and C_4H_{10} (Fig. 4.15e) on the other hand only have a single clearly layer of strong impact between 1,000 and 1,100 km height. C_4H_8, (Fig. 4.15d) is mainly changed near the top model boundary, while HCN (Fig. 4.15f) has two maxima, with the lower one of HCN lying below 900 km altitude.

The result of this experiment is therefore that the majority of species in the model are influenced by the tidal wave in a statistically significant manner in the thermosphere. The amplitude of the VMR, expressed as a percentage of

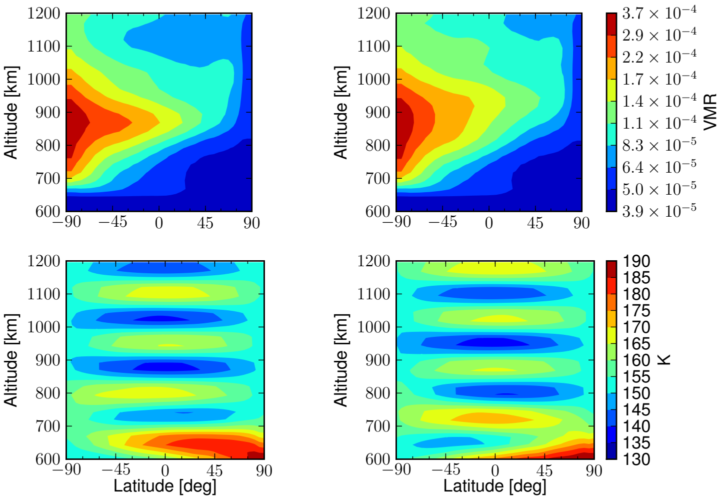

Figure 4.11: Like Fig. 4.10, but for C_2H_6.

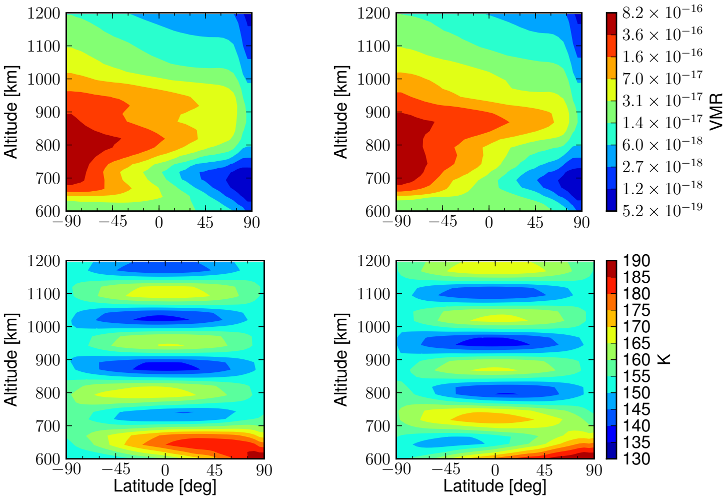

Figure 4.12: Like Fig. 4.10, but for C_3H_5.

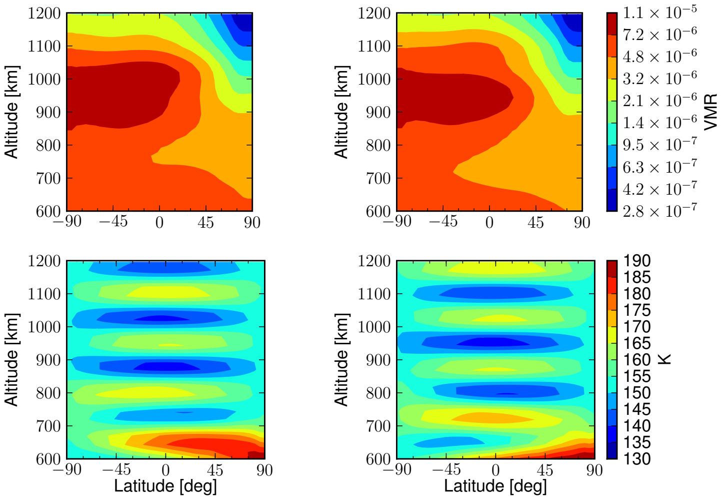

Figure 4.13: Like Fig. 4.10, but for C_3H_8.

Species	Correlation between VMR and T
CH_4	-0.17 ± 0.07
C_2H_2	-0.78 ± 0.02
C_2H_4	-0.76 ± 0.04
C_2H_6	-0.74 ± 0.02
C_3H_5	$+0.50 \pm 0.03$
C_3H_8	-0.41 ± 0.03
C_4H_2	-0.81 ± 0.02
C_4H_6	-0.76 ± 0.01
C_4H_8	$+0.66 \pm 0.03$
C_4H_{10}	-0.77 ± 0.03
HCN	-0.74 ± 0.04

Table 4.1: Correlations between temperature and VMR for selected species. Most species are higher in concentration when the temperature is below average.

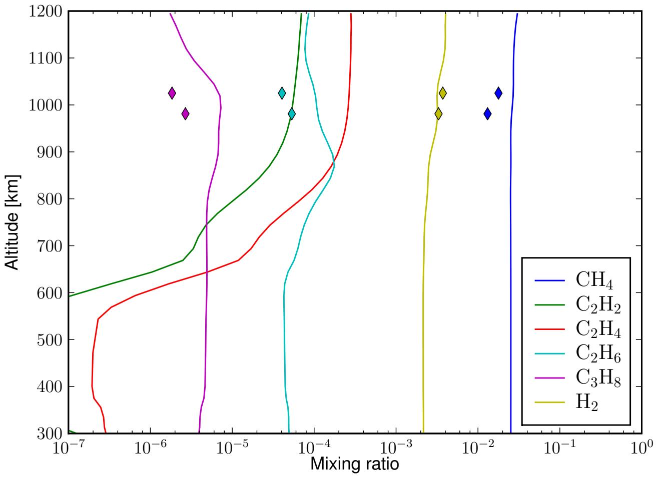

Figure 4.14: Instantaneous global-average VMR profiles for selected species from the Wave run with measurements from Cui *et al.* (2009). (The measured value for propane is meant to represent an upper bound.)

average VMR, is at least a few percent (methane) and up to 80 percent (C_4H_{10}) for the species presented here.

Generally the change in composition for longer-lived species can be said to be around a factor of two, so these gravitational tidal waves are strong enough to create changes that might be detectable by measurements if sufficient time series of data were available. Unfortunately, at this time the Cassini measurements are too sporadic for finding such relatively minor fluctuations. Very accurate instantaneous VMR profiles might be the best way to find the predicted effect, but these are not available from the Cassini data. However, this effect is something that a future mission to Titan might confirm.

4.3 Discussion

In this part of the study, the 3–D chemistry model of Titan's atmosphere was used to address some scientific problems. Since measurements of Titan's atmosphere are still relatively spotty compared to Earth and since only a fraction of Titan's seasonal and the Solar cycle has been covered by observations, the conclusions drawn cannot be immediately verified. However, since normally chemistry simulations for Titan are conducted for Solar average conditions, despite the fact that the Sun had average-to-low UV emissions during the Cassini mission so far, it is of interest to simulate specifically the Solar minimum case.

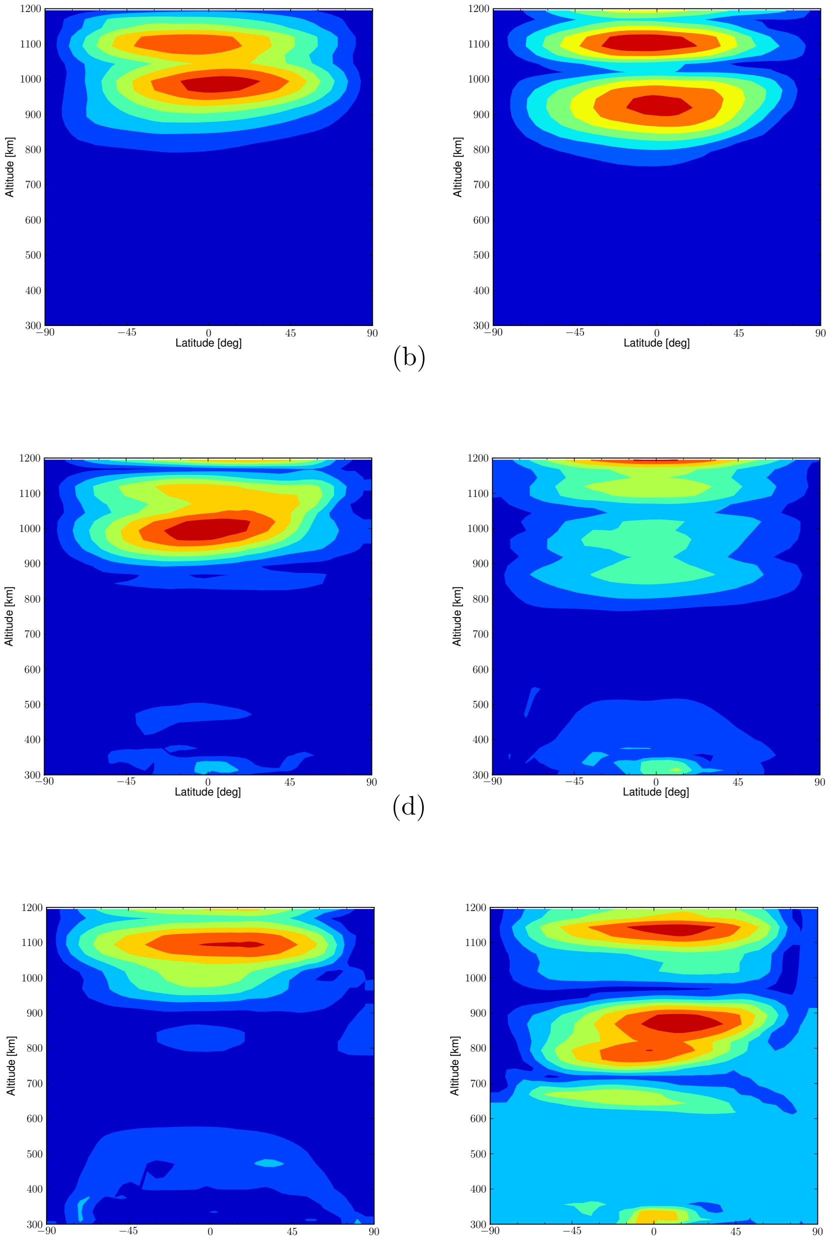

(a) (b)

(c) (d)

(e) (f)

Figure 4.15: Percentual changes in concentrations due to the temperature disturbance for (a) CH_4, (b) C_2H_6, (c) C_3H_8, (d) C_4H_8, (e) C_4H_{10}, and (f) HCN.

One major uncertainty is the impact of the Solar cycle on temperatures and temperatures on reaction rates, because so far only a single GCM simulation of Solar minimum conditions is available and because of the inherent uncertainty about the temperature dependence of some reaction rates.

In general, some of the species in the Solar variability experiments such as propane were influenced strongly, others very little. All in all, Solar minimum values were not in all respects a better fit to observations than for Solar average conditions.

In the second part of this chapter, upward-propagating gravitational tidal waves were considered, which are thought to be the cause of strong temperature fluctuations found in Titan's thermosphere. A time-dependent upward-traveling wave was incorporated into the model to find out if these fluctuations were intense enough to cause changes in chemistry due to their influence on reaction rates.

Highly significant correlations between temperature and VMR were found for many species as expected, but percentages of the VMR signal relative to the average VMR varied. Generally the change was found to be up to about a factor of two, which might be too low to be confirmed directly by available Cassini measurements at this point.

Chapter 5

Summary and outlook

A 3–D chemistry model for Titan's atmosphere was constructed and validated against available Cassini measurements. Good agreements between modeled and observed distributions were found for many species for the Control case, and the wind field was identified as one of the major influences that determines the quality of the fit. However, while some species benefitted from a modification of the GCM-derived winds, the best overall fit was achieved with the unaltered GCM winds.

The basic goal of this study was to show that a 3–D whole-atmosphere chemistry model for Titan's atmosphere, even without fully-coupled dynamics, is an important step towards both better comparison with and interpretation of Cassini measurements and an improved chemistry scheme. The influence of different Solar zenith angles and different temperature and wind fields exlain observed features of the chemical distributions of species that a column model cannot. Also, there is now a sufficient body of measurement data from Cassini that clearly shows horizontal differences in VMR, so validation is possible.

In earlier studies with this model, advection had a very strong influence, while in the experiments described here, advection is clearly secondary to Solar zenith angle variations. Still, it was possible to show that GCMs are now probably producing a relatively realistic meridional circulation, one that is considerably weaker than previously assumed but that still bring model results into better agreement with observations than a diffusion-only model.

The MOZART model in this study was then also run for different levels of Solar activity with accompanying dynamic fields from the GCM. Solar cycle influence on chemistry for Titan had so far not been studied very much, with most models being run (just as the Control experiment in this study) for Solar average conditions, despite the fact the Cassini measurement so far center mostly on a period of lower-than-average Solar activity. It was indeed found that the fit to observations was improved for some species, particularly those that were already quite close to measurements in the Control experiment. Other species that are more problematic in Control did not necessarily improve. Still, the majority of species was clearly influenced in a significant way by the combination of changed photodissociation and wind and temperature fields, with the least affected species (CH_3CN) being likely constrained by the fixed atomic hydrogen profile in the model.

Finally, as a more speculative experiment, an upward-propagating gravitational tidal wave temperature disturbance was put into the model to study the effect on chemistry and see if it would be significant enough to disover in available measurements. Because many chemical reaction rates have been extrapolated to Titan temperatures from measurements at higher temparures, it was felt that results for the warm phase of the wave were probably more realistic than for the cold phase. Definite effects of the temperature disturbance were found, with the problem with validation mainly being Cassini measurements having a large vertical uncertainty in the thermosphere. Nevertheless, as the Huygens descent had shown large local temperature variations from the time-mean, global-mean temperature profile in Titan's atmosphere, it remains an attractive idea that local temperature variations could play an important role in the chemistry and explain discrepancies betwen model and observations or inconsistencies in the measurements themselves (where e.g. two measurements were made at very close coordinates but different times and show very different concentrations). More accurate information about the vertical wavelength of the disturbance in the thermosphere and temperature dependence on chemical rates would be necessary to find out if the effect on chemistry is comparable—or perhaps even larger—than the current experiment suggests.

5.1 Further research

As the Cassini mission is ongoing, new measurements will further modify and refine the existing understanding of chemical distributions in Titan's atmosphere. In the thermosphere, distributions are relatively smooth, so it is hoped that new measurements, particularly for other horizontal coordinates, will agree at least qualitatively—but perhaps also quantitatively—relatively well with the existing model.

Ultimately, a fully-coupled dynamical-chemical model for Titan's atmosphere would be desirable. There have been steps in that direction, but so far chemistry in Titan GCMs had to be very simplified and therefore only worked for a limited vertical range of Titan's atmosphere. The MOZART model shows that using the full chemistry is feasible in a 3–D model, which allows chemical species to be produced over the entire atmospheric extent and then diffused and advected in the model.

An annual cycle was not included in this model, but as new data Cassini becomes availalbe it would be useful to either carry out additional experiments for fixed seasons and interpolate (similar to the Solar actitivity runs) or run a transient experiment with continuously-changing Solar position. Such runs are however limited by available computing resources and were therefore not done for this study.

Further refinements to the model would be incorporation of microphysics. As dicussed previously, it has been proposed that even in the thermosphere haze might have a noticeable effect on chemistry and might explain some of the disparities between observations and models. However, many uncertainties remain regarding the chemical rate constants themselves, so at the present more accurate and applicable measurements of rate constants in the laboratory would probably do more to improve models than postulating all kinds of heterogeneous loss processes that are even harder to study on Earth than chemical kinetics. A model should only incorporate additional processes and refinements when the more basic aspects are relatively certain and well-established and remaining discrepancies can only be explained by lack of complexity in the model. Otherwise there is a risk of new processes being essentially a set of freely-selectable tuning parameters that can be used to cover flaws in the more basic parts of the model, i.e. the chemistry scheme in this case. Therefore, resorting the microphysics to account for model–measurements discrepancies in the thermosphere is somewhat speculative at this point.

The chemistry scheme in the present 3–D Titan model can readily be updated and improved as new progress in 1–D modeling is made and model results can then show if the chemical scheme also works for other locations on Titan. In that sense, this model represents another step in the chemical modeling of Titan's atmosphere: first there were columns models that were compared with all global data for Titan, then came column models that were run for different latitudinal bands that were validated against according subsets of measurements, then meridional 2–D models, and now a coarse but fully 3–D model exists from which concentrations can be retrieved for different Titan coordinates and Solar activity level, matching the conditions at the time of measurement.

Appendix A

Model parameters and reaction rates

Model levels

Level No.	p [hPa]	Median h [km]	Global-mean T [K]	K [cm^2/s]
1	1.2×10^{-8}	1194.00	155.0	5.0×10^{7}
2	1.7×10^{-8}	1169.00	154.8	5.0×10^{7}
3	2.4×10^{-8}	1144.00	154.5	5.0×10^{7}
4	3.5×10^{-8}	1119.00	154.2	5.0×10^{7}
5	5.0×10^{-8}	1094.00	153.8	5.0×10^{7}
6	7.2×10^{-8}	1069.00	153.3	5.0×10^{7}
7	1.1×10^{-7}	1044.00	152.7	5.0×10^{7}
8	1.5×10^{-7}	1019.00	152.2	5.0×10^{7}
9	2.3×10^{-7}	993.80	151.7	5.0×10^{7}
10	3.3×10^{-7}	968.80	151.4	5.0×10^{7}
11	4.9×10^{-7}	943.80	151.3	5.0×10^{7}
12	7.4×10^{-7}	918.80	151.3	5.0×10^{7}
13	1.1×10^{-6}	893.80	151.4	5.0×10^{7}
14	1.7×10^{-6}	868.80	151.7	5.0×10^{7}
15	2.5×10^{-6}	843.80	152.3	5.0×10^{7}
16	3.9×10^{-6}	818.80	153.2	5.0×10^{7}
17	5.9×10^{-6}	793.80	154.3	5.0×10^{7}
18	9.2×10^{-6}	768.80	155.6	5.0×10^{7}
19	1.4×10^{-5}	743.80	157.1	5.0×10^{7}
20	2.3×10^{-5}	718.80	158.9	5.0×10^{7}

Level No.	p [hPa]	Median h [km]	Global-mean T [K]	K [cm^2/s]
21	3.6×10^{-5}	693.80	161.2	4.7×10^{7}
22	5.7×10^{-5}	668.80	163.8	3.5×10^{7}
23	9.4×10^{-5}	643.80	165.8	2.7×10^{7}
24	1.6×10^{-4}	618.80	167.2	2.0×10^{7}
25	2.7×10^{-4}	593.80	168.3	1.5×10^{7}
26	4.7×10^{-4}	568.80	169.8	1.2×10^{7}
27	8.1×10^{-4}	543.80	172.1	8.7×10^{6}
28	1.3×10^{-3}	472.00	173.4	3.9×10^{6}
29	1.9×10^{-3}	400.30	176.9	1.8×10^{6}
30	3.7×10^{-3}	375.10	180.3	1.3×10^{6}
31	6.2×10^{-3}	355.80	183.8	1.1×10^{6}
32	1.1×10^{-2}	334.80	187.3	8.4×10^{5}
33	2.0×10^{-2}	313.10	186.7	6.6×10^{5}
34	3.6×10^{-2}	291.70	185.2	5.2×10^{5}
35	6.5×10^{-2}	270.30	182.3	4.1×10^{5}
36	1.2×10^{-1}	249.00	177.2	3.2×10^{5}
37	2.1×10^{-1}	227.60	171.4	2.5×10^{5}
38	3.8×10^{-1}	206.20	166.9	2.0×10^{5}
39	6.8×10^{-1}	184.90	162.4	1.6×10^{5}
40	1.2×10^{0}	163.80	161.5	1.2×10^{5}
41	2.2×10^{0}	142.90	159.5	9.9×10^{4}
42	4.0×10^{0}	122.80	157.1	7.9×10^{4}
43	7.1×10^{0}	103.80	149.0	6.4×10^{4}
44	1.3×10^{1}	86.25	132.2	3.2×10^{3}
45	2.3×10^{1}	70.88	107.5	3.2×10^{3}
46	4.0×10^{1}	59.07	83.7	3.2×10^{3}
47	6.9×10^{1}	50.09	72.8	3.2×10^{3}
48	1.2×10^{2}	41.99	71.0	3.2×10^{3}
49	2.0×10^{2}	34.28	72.9	3.2×10^{3}
50	3.2×10^{2}	26.95	76.6	3.2×10^{3}
51	4.9×10^{2}	20.05	81.2	3.2×10^{3}
52	7.2×10^{2}	13.78	86.0	3.2×10^{3}
53	9.7×10^{2}	8.45	90.1	3.2×10^{3}
54	1.2×10^{3}	4.37	92.8	3.2×10^{3}
55	1.4×10^{3}	1.85	94.0	3.2×10^{3}
56	1.4×10^{3}	0.71	94.3	3.2×10^{3}
57	1.5×10^{3}	0.29	94.5	3.2×10^{3}

Photolysis reactions and cross sections

#	Reaction			QY source*	CS source*
jch4a	$CH_4 + h\nu$	→	$CH_3 + H$	Lav	W&A
jch4b		→	$^1CH_2 + H_2$	Lav	W&A
jch4d		→	$^1CH_2 + 2\ H$	Lav	W&A
jch4e		→	$CH + H_2 + H$	Lav	W&A
jc2h6a	$C_2H_6 + h\nu$	→	$C_2H_4 + H_2$	W&A	W&A
jc2h6c		→	$C_2H_2 + 2\ H_2$	W&A	W&A
jc2h6e		→	$2\ CH_3$	W&A	W&A
jc2h4a	$C_2H_4 + h\nu$	→	$C_2H_2 + H_2$	W&A	W&A
jc2h2a	$C_2H_2 + h\nu$	→	$C_2H + H$	W&A	W&A
jc2h2b		→	$C_2 + H_2$	W&A	W&A
jc2h5	$C_2H_5 + h\nu$	→	$CH_3 + {}^1CH_2$	Lav	W&A
jc2h3	$C_2H_3 + h\nu$	→	$C_2H_2 + H$	Lav	W&A
jch3c2h	$CH_3C_2H + h\nu$	→	$C_3H_3 + H$	W&A	W&A
jc4h6b	$C_4H_6 + h\nu$	→	$2\ C_2H_3$	W&A	W&A
jc4h6c		→	$C_2H_4 + C_2H_2$	W&A	W&A
jc4h6d		→	$C_3H_3 + CH_3$	W&A	W&A
jc3h6b	$C_3H_6 + h\nu$	→	$CH_3C_2\ H + H_2$	W&A	W&A
jc3h6d		→	$C_3H_4 + {}^1CH_2$	W&A	W&A
jc3h6e		→	$C_2H_3 + CH_3$	W&A	W&A
jc3h6f		→	$C_2H_2 + CH_4$	W&A	W&A
jc3h8a	$C_3H_8 + h\nu$	→	$C_3H_6 + H_2$	W&A	W&A
jc3h8b		→	$C_3H_6 + {}^1CH_2$	W&A	W&A
jc3h8d		→	$C_2H_4 + CH_4$	W&A	W&A
jc6h2a	$C_6H_2 + h\nu$	→	$C_6H + H$	W&A	W&A
jc6h2b		→	$C_4H + C_2H$	W&A	W&A
jhc3nb	$HC_3N + h\nu$	→	$CN + C_2H$	W&A	W&A
jhcn	$HCN + h\nu$	→	$CN + H$	Lav	W&A
jn2a	$N_2 + h\nu$	→	$N + N^+ + e$	Lav	W&A
jn2b		→	$N(^2D) + N^+ + e$	Lav	W&A
jn2c		→	$N_2^+ + e$	Lav	W&A
jn2d		→	$N(^2D) + N$	Lav	W&A
jch3a	$CH_3 + h\nu$	→	$^1CH_2 + H$	Lav	Lav
jch3b		→	$CH + H_2$	Lav	Lav

jc2h5na	$C_2H_5N + h\nu \rightarrow C_2H_4 + NH$	Lav	Lav
jc2h5nb	$\rightarrow CH_3 + H_2CN$	Lav	Lav
jc2h5nc	$\rightarrow C_2H_2 + NH_3$	Lav	Lav
jc4h2a	$C_4H_2 + h\nu \rightarrow C_4H + H$	W&A	W&A
jc4h2b	$\rightarrow 2\ C_2H$	W&A	W&A
jc4h2c	$\rightarrow C_2H_2 + C_2$	W&A	W&A
jc4h2d	$\rightarrow {}^*C_4H_2$	W&A	W&A

*) Lav = Lavvas *et al.*, 2008; W&A = Wilson and Atreya, 2004

Reaction rates

Meaning of the reaction number prefixes for the origin of the rate constants:

- 'k': from Krasnopolsky (2009)
- 'l': from Lavvas *et al.* (2008)
- 'w': from Wilson and Atreya (2004)
- 'T': additionally tuned

#	Reaction	Rate coefficients
k91	$ND \rightarrow N$	1.1×10^{-5}
k92	$ND + N_2 \rightarrow N + N_2$	1.6×10^{-14}
k93	$ND + CH_4 \rightarrow NH + CH_3$	$2.0 \times 10^{-11} e^{-750/T}$
k94	$ND + CH_4 \rightarrow CH_2NH + H$	$5.0 \times 10^{-11} e^{-750/T}$
k95	$ND + H_2 \rightarrow NH + H$	$4.6 \times 10^{-11} e^{-880/T}$
k96	$ND + C_2H_2 \rightarrow CHCN + H$	$1.6 \times 10^{-10} e^{-270/T}$
k97	$ND + C_2H_4 \rightarrow CH_3CN + H$	$4.6 \times 10^{-11} e^{-500/T}$
k98	$ND + C_2H_4 \rightarrow NH + C_2H_3$	$1.8 \times 10^{-10} e^{-500/T}$
k99	$ND + C_2H_6 \rightarrow NH + C_2H_5$	1.9×10^{-11}
k100	$ND + C_3H_4 \rightarrow C_2H_3CN + H$	$4.6 \times 10^{-11} e^{-500/T}$
k101	$ND + C_3H_6 \rightarrow C_2H_5CN + H$	6.6×10^{-11}
k102	$ND + C_4H_4 \rightarrow C_4H_3N + H$	$4.6 \times 10^{-11} e^{-500/T}$
k103	$ND + C_4H_6 \rightarrow C_4H_5N + H$	6.6×10^{-11}
k104	${}^1CH_2 + N_2 \rightarrow CH_2 + N_2$	$2.4 \times 10^{-14} T$
k105	${}^1CH_2 + CH_4 \rightarrow CH_3 + CH_3$	6.0×10^{-11}
k106	${}^1CH_2 + H_2 \rightarrow CH_3 + H$	9.0×10^{-11}
k107	${}^*C_4H_2 \rightarrow C_4H_2$	1.0×10^{1}

#	Reaction	Rate coefficients
k108	$^*C_4H_2 + N_2 \rightarrow C_4H_2 + N_2$	1.4×10^{-15}
k109	$^*C_4H_2 + C_4H_2 \rightarrow C_6H_2 + C_2H_2$	2.3×10^{-12}
k110	$^*C_4H_2 + C_2H_2 \rightarrow C_6H_2 + H + H$	3.5×10^{-13}
k111	$^*C_4H_2 + C_2H_4 \rightarrow C_6H_4 + H + H$	5.0×10^{-13}
k112	$^*C_4H_2 + C_3H_4 \rightarrow C_7H_4 + H_2$	7.0×10^{-13}
k113	$^*C_4H_2 + C_3H_6 \rightarrow C_6H_4 + CH_3 + H$	8.0×10^{-13}
k114	$C + H_2 + M \rightarrow CH_2 + M$	2.0×10^{-29}
k115	$CH + H \rightarrow C + H_2$	1.4×10^{-11}
k116	$CH_2 + H \rightarrow CH + H_2$	$3.6 \times 10^{-11} T^{0.32}$
k117	$CH_2 + H + M \rightarrow CH_3 + M$	$k_0 = 3.5 \times 10^{-29} k_\infty = 3.0 \times 10^{18}$
k118	$CH_2 + CH_2 \rightarrow C_2H_2 + H + H$	$2.0 \times 10^{-10} e^{-400/T}$
k119	$CH_3 + H + M \rightarrow CH_4 + M$	$k_0 = 1.0 \times 10^{-29} e^{260/T} k_\infty = 4.0 \times 10^{17}$
k120	$CH_3 + CH_2 \rightarrow C_2H_4 + H$	7.0×10^{-11}
k121	$CH_3 + CH_3 + M \rightarrow C_2H_6 + M$	$k_0 = 2.8 \times 10^{-3} T^{-8.75} e^{-980/T} k_\infty = 1.0 \times 10^{3}$
k122	$CH_4 + CH \rightarrow C_2H_4 + H$	$3.0 \times 10^{-8} e^{-36/T}$
k123	$C_2 + CH_4 \rightarrow C_3H_3 + H$	$1.0 \times 10^{-10} T^{-0.42} e^{-13/T}$
k124	$C_2 + C_2H_2 \rightarrow C_4H + H$	$1.9 \times 10^{-7} T^{-1.14} e^{-77/T}$
k125	$C_2 + C_2H_4 \rightarrow C_4H_3 + H$	$5.0 \times 10^{-8} T^{-0.93} e^{-58/T}$
k126	$C_2 + C_2H_6 \rightarrow C_3H_3 + CH_3$	$2.8 \times 10^{-8} T^{-0.94} e^{-44/T}$
k127	$C_2 + C_3H_8 \rightarrow C_3H_2 + C_2H_6$	$3.9 \times 10^{-7} T^{-1.31} e^{-94/T}$
k128	$C_2H + CH_4 \rightarrow C_2H_2 + CH_3$	$1.2 \times 10^{-11} e^{-490/T}$
k129	$C_4H + CH_4 \rightarrow C_4H_2 + CH_3$	$1.2 \times 10^{-11} e^{-490/T}$
k130	$C_2H_2 + H + M \rightarrow C_2H_3 + M$	$k_0 = 3.3 \times 10^{-30} e^{-740/T} k_\infty = 1.6 \times 10^{17}$
k131	$C_2H_2 + CH \rightarrow C_3H_2 + H$	$1.6 \times 10^{-9} T^{-0.23} e^{-16/T}$
k132	$C_2H_2 + C_2H \rightarrow C_4H_2 + H$	$8.6 \times 10^{-16} T^{1.8} e^{474/T}$
k133	$C_2H_2 + C_4H \rightarrow C_6H_2 + H$	$7.6 \times 10^{-8} T^{-1.06} e^{66/T}$
k134	$C_2H_3 + H \rightarrow C_2H_2 + H_2$	7.5×10^{-11}
k135	$C_2H_3 + H + M \rightarrow C_2H_4 + M$	$k_0 = 8.0 \times 10^{-33} T^{2.2} k_\infty = 3.0 \times 10^{17}$
k136	$C_2H_3 + CH_2 \rightarrow C_2H_2 + CH_3$	3.0×10^{-11}
k137	$C_2H_3 + CH_3 \rightarrow C_2H_2 + CH_4$	3.3×10^{-11}

#	Reaction	Rate coefficients
k138	$C_2H_3 + CH_3 + M \rightarrow C_3H_6 + M$	$k_0 = 5.0 \times 10^{-26}$ $k_\infty = 1.0 \times 10^{3}$
k139	$C_2H_3 + C_2H_2 \rightarrow C_4H_4 + H$	$3.3 \times 10^{-12} e^{-2520/T}$
k140	$C_2H_3 + C_2H_2 + M \rightarrow C_4H_5 + M$	$k_0 = 1.5 \times 10^{-14} T^{-5.8} e^{-2364/T}$ $k_\infty = 1.0 \times 10^{3}$
k141	$C_2H_3 + C_2H_3 \rightarrow C_2H_4 + C_2H_2$	3.5×10^{-11}
k142	$C_2H_3 + C_2H_3 + M \rightarrow C_4H_6 + M$	$k_0 = 5.0 \times 10^{-26}$ $k_\infty = 1.0 \times 10^{3}$
k143	$C_2H_4 + H + M \rightarrow C_2H_5 + M$	$k_0 = 8.0 \times 10^{-30} e^{-380/T}$ $k_\infty = 1.3 \times 10^{17}$
k144	$C_2H_4 + C \rightarrow C_2H + CH_3$	$4.6 \times 10^{-10} T^{-0.07}$
k145	$C_2H_4 + CH \rightarrow C_3H_4 + H$	1.5×10^{-10}
k146	$C_2H_4 + C_2H \rightarrow C_4H_4 + H$	1.4×10^{-10}
k147	$C_2H_4 + C_4H \rightarrow C_2H_3 + C_4H_2$	$9.5 \times 10^{-10} T^{-0.4} e^{-10/T}$
k148	$C_2H_4 + C_4H \rightarrow C_6H_4 + H$	$9.5 \times 10^{-10} T^{-0.4} e^{-10/T}$
k149	$C_2H_5 + H \rightarrow CH_3 + CH_3$	1.0×10^{-10}
k150	$C_2H_5 + H \rightarrow C_2H_4 + H_2$	3.0×10^{-12}
k151	$C_2H_5 + CH_2 \rightarrow C_2H_4 + CH_3$	3.0×10^{-11}
k152	$C_2H_5 + CH_3 \rightarrow C_2H_4 + CH_4$	2.2×10^{-12}
k153	$C_2H_5 + CH_3 + M \rightarrow C_3H_8 + M$	$k_0 = 8.0 \times 10^{19} T^{-16.1} e^{-1900/T}$ $k_\infty = 5.0 \times 10^{11}$
k154	$C_2H_5 + C_2H_3 + M \rightarrow C_4H_8 + M$	$k_0 = 5.0 \times 10^{-26}$ $k_\infty = 1.0 \times 10^{3}$
k155	$C_2H_5 + C_2H_3 \rightarrow C_2H_4 + C_2H_4$	1.0×10^{-10}
k156	$C_2H_5 + C_2H_5 \rightarrow C_2H_4 + C_2H_6$	2.4×10^{-12}
k157	$C_2H_5 + C_2H_5 + M \rightarrow C_4H_{10} + M$	$k_0 = 6.6 \times 10^{-6} T^{-6.4} e^{-300/T}$ $k_\infty = 3.0 \times 10^{9}$
k158	$C_2H_6 + CH \rightarrow C_2H_4 + CH_3$	$2.7 \times 10^{-8} T^{-0.86} e^{-53/T}$
k159	$C_2H_6 + CH \rightarrow C_3H_6 + H$	$1.1 \times 10^{-8} T^{-0.86} e^{-53/T}$
k160	$C_2H_6 + C_2H \rightarrow C_2H_5 + C_2H_2$	3.5×10^{-11}
k161	$C_2H_6 + C_4H \rightarrow C_2H_5 + C_4H_2$	$3.4 \times 10^{-8} T^{-1.24} e^{-26/T}$
k162	$C_3H_2 + H + M \rightarrow C_3H_3 + M$	$k_0 = 1.7 \times 10^{-26}$ $k_\infty = 6.0 \times 10^{14}$

#	Reaction	Rate coefficients
k163	$C_3H_3 + H + M \rightarrow C_3H_4 + M$	$k_0 = 1.7 \times 10^{-26} k_\infty = 2.0 \times 10^{16}$
k164	$C_3H_3 + CH_3 + M \rightarrow C_4H_6 + M$	$k_0 = 5.0 \times 10^{-26} k_\infty = 1.0 \times 10^{3}$
k165	$C_3H_3 + C_3H_3 + M \rightarrow C_6H_6 + M$	$k_0 = 1.0 \times 10^{-26} k_\infty = 3.0 \times 10^{14}$
k166	$C_3H_4 + H \rightarrow C_2H_2 + CH_3$	$4.0 \times 10^{-11} e^{-960/T}$
k167	$C_3H_4 + H + M \rightarrow C_3H_5 + M$	$k_0 = 8.0 \times 10^{-24} T^{-2} e^{-1220/T} k_\infty = 2.0 \times 10^{17}$
k168	$C_3H_4 + C_2H \rightarrow C_3H_3 + C_2H_2$	$1.2 \times 10^{-9} T^{-0.3}$
k169	$C_3H_5 + H \rightarrow C_3H_4 + H_2$	3.0×10^{-11}
k170	$C_3H_5 + H + M \rightarrow C_3H_6 + M$	$k_0 = 1.0 \times 10^{-24} k_\infty = 2.5 \times 10^{14}$
k171	$C_3H_5 + CH_2 \rightarrow C_4H_6 + H$	5.0×10^{-11}
k172	$C_3H_5 + CH_3 \rightarrow C_3H_4 + CH_4$	$5.0 \times 10^{-12} T^{-0.32} e^{66/T}$
k173	$C_3H_5 + CH_3 + M \rightarrow C_4H_8 + M$	$k_0 = 5.0 \times 10^{-26} k_\infty = 1.0 \times 10^{3}$
k174	$C_3H_5 + C_2H_3 \rightarrow C_3H_6 + C_2H_2$	8.0×10^{-12}
k175	$C_3H_5 + C_2H_3 \rightarrow C_3H_4 + C_2H_4$	4.0×10^{-12}
k176	$C_3H_5 + C_2H_5 \rightarrow C_3H_6 + C_2H_4$	$4.3 \times 10^{-12} e^{66/T}$
k177	$C_3H_5 + C_2H_5 \rightarrow C_3H_4 + C_2H_6$	$1.6 \times 10^{-12} e^{66/T}$
k178	$C_3H_6 + H + M \rightarrow C_3H_7 + M$	$k_0 = 1.5 \times 10^{-29} k_\infty = 5.0 \times 10^{15}$
k179	$C_3H_6 + CH_2 \rightarrow C_3H_5 + CH_3$	$2.7 \times 10^{-12} e^{-2660/T}$
k180	$C_3H_7 + H \rightarrow C_3H_6 + H_2$	4.0×10^{-12}
k181	$C_3H_7 + H + M \rightarrow C_3H_8 + M$	$k_0 = 1.0 \times 10^{-29} e^{260/T} k_\infty = 4.0 \times 10^{17}$
k182	$C_3H_7 + CH_2 \rightarrow C_3H_6 + CH_3$	3.0×10^{-11}
k183	$C_3H_7 + CH_2 \rightarrow C_2H_5 + C_2H_4$	3.0×10^{-11}
k184	$C_3H_7 + CH_3 \rightarrow C_3H_6 + CH_4$	$1.9 \times 10^{-11} T^{-0.32}$
k185	$C_3H_7 + C_2H_3 \rightarrow C_3H_8 + C_2H_2$	2.0×10^{-12}
k186	$C_3H_7 + C_2H_3 \rightarrow C_3H_6 + C_2H_4$	2.0×10^{-12}
k187	$C_3H_7 + C_2H_5 \rightarrow C_3H_8 + C_2H_4$	2.0×10^{-12}
k188	$C_3H_7 + C_2H_5 \rightarrow C_3H_6 + C_2H_6$	2.0×10^{-12}
k189	$C_3H_8 + C_2H \rightarrow C_3H_7 + C_2H_2$	8.0×10^{-11}
k190	$C_4H + C_3H_4 \rightarrow C_7H_4 + H$	$3.4 \times 10^{-8} T^{-0.82} e^{-47/T}$

#	Reaction			Rate coefficients
k191	$C_4H + C_3H_8$	$\rightarrow$	$C_7H_8 + H$	$2.3 \times 10^{-7} T^{-1.35} e^{-56/T}$
k192	$C_4H_2 + H + M$	$\rightarrow$	$C_4H_3 + M$	$k_0 = 1.0 \times 10^{-28} k_\infty = 1.3 \times 10^{15}$
k193	$C_4H_2 + C_2H$	$\rightarrow$	$C_6H_2 + H$	4.0×10^{-11}
k194	$C_4H_2 + C_4H$	$\rightarrow$	$C_8H_2 + H$	4.0×10^{-11}
k195	$C_4H_3 + H$	$\rightarrow$	$C_4H_2 + H_2$	3.0×10^{-11}
k196	$C_4H_3 + CH_3$	$\rightarrow$	$C_4H_2 + CH_4$	3.3×10^{-11}
k197	$C_4H_4 + H + M$	$\rightarrow$	$C_4H_5 + M$	$k_0 = 1.0 \times 10^{7} T^{-7} e^{-1390/T} k_\infty = 6.0 \times 10^{14}$
k198	$C_4H_5 + H$	$\rightarrow$	$C_4H_4 + H_2$	3.0×10^{-12}
k199	$C_4H_5 + H + M$	$\rightarrow$	$C_4H_6 + M$	$k_0 = 5.0 \times 10^{-26} k_\infty = 1.0 \times 10^{3}$
k200	$C_4H_5 + C_2H_2$	$\rightarrow$	$C_6H_6 + H$	$4.0 \times 10^{-16} T^{1.18} e^{-1880/T}$
k201	$C_6H_2 + C_2H$	$\rightarrow$	$C_8H_2 + H$	$1.0 \times 10^{-10} e^{31/T}$
k202	$C_6H_5 + H + M$	$\rightarrow$	$C_6H_6 + M$	$k_0 = 1.0 \times 10^{-29} e^{260/T} k_\infty = 4.0 \times 10^{17}$
k203	$C_6H_6 + C_4H_5$	$\rightarrow$	$C_{10}H_{10} + H$	$2.2 \times 10^{-13} e^{-3220/T}$
k204	$C_6H_6 + C_6H_5$	$\rightarrow$	$C_{12}H_{10} + H$	$6.6 \times 10^{-13} e^{-2010/T}$
k210	$C_6H_6 + C_6H_5$	$\rightarrow$	$C_{12}H_{10} + H$	$1.0 \times 10^{-12} T^{0.2} e^{-2520/T}$
k211	$C_6H_6 + C_6H_5$	$\rightarrow$	$C_{12}H_{10} + H$	$k_0 = 5.0 \times 10^{-19} T^{-4} e^{400/T} k_\infty = 7.0 \times 10^{8}$
k212	$C_6H_6 + C_6H_5$	$\rightarrow$	$C_{12}H_{10} + H$	8.0×10^{-11}
k213	$C_6H_6 + C_6H_5$	$\rightarrow$	$C_{12}H_{10} + H$	$1.6 \times 10^{-12} e^{-2170/T}$
k218	$N + CH$	$\rightarrow$	$CN + H$	$2.8 \times 10^{-10} T^{-0.1}$
k219	$N + CH_2$	$\rightarrow$	$HCN + H$	$5.0 \times 10^{-11} e^{-250/T}$
k220	$N + CH_3$	$\rightarrow$	$H_2CN + H$	$4.3 \times 10^{-10} e^{-420/T}$
k221	$N + H_2CN$	$\rightarrow$	$HCN + NH$	$1.0 \times 10^{-10} e^{-200/T}$
k222	$H + H_2CN$	$\rightarrow$	$HCN + H_2$	$2.0 \times 10^{-10} e^{-200/T}$
k223	$H + H_2CN$	$\rightarrow$	$HCN + H_2$	$1.1 \times 10^{-12} e^{-900/T}$
k224	$H + H_2CN$	$\rightarrow$	$HCN + H_2$	$1.1 \times 10^{-12} e^{-900/T}$
k226	$CH_2CN + H + M$	$\rightarrow$	$CH_3CN + M$	1.0×10^{-29}
k227	$N + C_2H_3$	$\rightarrow$	$CH_2CN + H$	6.2×10^{-11}
k228	$N + C_2H_3$	$\rightarrow$	$C_2H_2 + NH$	1.2×10^{-11}
k229	$N + C_2H_3 + M$	$\rightarrow$	$CH_3CN + M$	4.0×10^{-29}
k230	$N + C_2H_5$	$\rightarrow$	$C_2H_4 + NH$	7.0×10^{-11}

#	Reaction	Rate coefficients
k231	$N + C_2H_5 \rightarrow H_2CN + CH_3$	4.0×10^{-11}
k232	$N + C_2H_5 \rightarrow CH_3CN + H_2$	1.0×10^{-11}
k233	$N + C_2H_5 \rightarrow NH_3 + C_2H_2$	1.0×10^{-11}
k234	$N + CHCN \rightarrow C_2N_2 + H$	1.0×10^{-12}
k235	$N + C_3H_6 \rightarrow C_2H_5CN + H$	1.9×10^{-12}
k236	$N + C_3H_6 \rightarrow NH_3 + C_3H_3$	1.9×10^{-12}
k237	$N + C_4H_4 \rightarrow C_4H_3N + H$	1.9×10^{-12}
k238	$NH + H \rightarrow N + H_2$	$3.0 \times 10^{-16} T^{1.5} e^{-100/T}$
k239	$NH + N \rightarrow N_2 + H$	2.5×10^{-11}
k240	$NH + NH \rightarrow NH_2 + N$	$1.0 \times 10^{-21} T^{2.9} e^{1000/T}$
k241	$NH + CH_3 \rightarrow CH_4 + N$	4.0×10^{-11}
k242	$NH + CH_2 \rightarrow CH_3 + N$	4.0×10^{-11}
k243	$NH + C_2H_3 \rightarrow C_2H_4 + N$	4.0×10^{-11}
k244	$NH + C_2H_5 \rightarrow C_2H_6 + N$	4.0×10^{-11}
k245	$NH + C_2H_2 \rightarrow CHCN + H_2$	$2.0 \times 10^{-9} T^{-1.07}$
k246	$NH_2 + H + M \rightarrow NH_3 + M$	$k_0 = 3.0 \times 10^{-30} k_\infty = 3.0 \times 10^{19}$
k247	$NH_2 + N \rightarrow N_2 + H + H$	1.2×10^{-10}
k248	$NH_2 + NH_2 + M \rightarrow N_2H_4 + M$	$k_0 = 9.0 \times 10^{-20} T^{-3.9} k_\infty = 8.0 \times 10^{17}$
k249	$NH_2 + NH_2 \rightarrow N_2H_2 + H_2$	1.3×10^{-12}
k250	$NH_2 + CH_3 + M \rightarrow CH_3NH_2 + M$	$k_0 = 6.0 \times 10^{-18} T^{-3.85} k_\infty = 6.0 \times 10^{15}$
k251	$N_2H_2 + H \rightarrow N_2H + H_2$	$1.4 \times 10^{-19} T^{2.6} e^{115/T}$
k252	$N_2H_2 + NH_2 \rightarrow NH_3 + N_2H$	$1.5 \times 10^{-25} T^{4.05} e^{810/T}$
k253	$N_2H + H \rightarrow N_2 + H_2$	1.7×10^{-12}
k254	$N_2H_4 + H \rightarrow N_2H_3 + H_2$	$1.0 \times 10^{-11} e^{-1200/T}$
k255	$N_2H_3 + H \rightarrow NH_2 + NH_2$	2.7×10^{-12}
k256	$CH_2NH + H \rightarrow CH_3 + NH$	1.0×10^{-11}
k257	$CN + CH_4 \rightarrow HCN + CH_3$	$5.7 \times 10^{-12} e^{-675/T}$
k258	$CN + C_2H_2 \rightarrow HC_3N + H$	$5.3 \times 10^{-9} T^{-0.52} e^{-19/T}$
k259	$CN + C_2H_4 \rightarrow HCN + C_2H_3$	$1.1 \times 10^{-8} T^{-0.7} e^{-31/T}$
k260	$CN + C_2H_4 \rightarrow C_2H_3CN + H$	$2.7 \times 10^{-9} T^{-0.7} e^{-31/T}$
k261	$CN + C_2H_6 \rightarrow HCN + C_2H_5$	$6.0 \times 10^{-12} T^{0.22} e^{58/T}$
k262	$CN + C_3H_4 \rightarrow HCN + C_3H_3$	4.0×10^{-10}
k263	$CN + C_4H_2 \rightarrow C_5HN + H$	4.2×10^{-10}
k264	$CN + HCN \rightarrow C_2N_2 + H$	$2.5 \times 10^{-17} T^{1.7} e^{-770/T}$

#	Reaction			Rate coefficients
k265	$CN + HC_3N$	→	$C_4N_2 + H$	1.7×10^{-11}
k266	$CN + CH_3CN$	→	$C_2N_2 + CH_3$	$6.5 \times 10^{-11} e^{-1190/T}$
k267	$CN + CH_2CN$	→	$C_2N_2 + CH_2$	5.0×10^{-10}
k275	$CH + HCN$	→	$CHCN + H$	$5.0 \times 10^{-11} e^{500/T}$
k276	$CHCN + H$	→	$C_2N + H_2$	3.0×10^{-11}
k278	$C_2N + CH_4$	→	$CHCN + CH_3$	6.0×10^{-14}
k279	$C_2N + C_2H_6$	→	$C_4H_3N + H_2 + H$	2.9×10^{-12}
k280	$C_3N + CH_4$	→	$HC_3N + CH_3$	5.0×10^{-14}
k281	$C_3N + C_2H_6$	→	$C_5H_5N + H$	3.0×10^{-12}
k282	$C_3N + HCN$	→	$C_4N_2 + H$	3.0×10^{-11}
k283	$CH_2CN + CN$	→	$C_2N_2 + CH_2$	2.0×10^{-10}
k284	$HC_3N + C_2H$	→	$HC_5N + H$	1.0×10^{-11}
k285	$HCN + C_2H_3$	→	$C_2H_3CN + H$	$1.1 \times 10^{-12} e^{-900/T}$
k286	$CH_3CN + H$	→	$CN + CH_4$	$1.7 \times 10^{-12} e^{-1500/T}$
r176	$CH + C_2H_4$	→	$CH_3C_2H + H$	$3.87 \times 10^{-9} T^{-0.55} e^{-29.6/T}$
r238	$2\ CH_3$	→		
r396	$N_2^+ + N$	→	$N^+ + N_2$	1.0×10^{-11}
r397	$N_2^+ + CH_4$	→	$CH_3 + N_2 + H + e$	1.0×10^{-9}
r399	$N^+ + NH$	→	$N_2^+ + H$	3.7×10^{-10}
r400	$N^+ + CH_4$	→	$CH_3 + NH + e$	5.0×10^{-10}
r401	$N^+ + CH_4$	→	$H_2CN + H_2 + e$	5.0×10^{-10}
w56a	$C_3H_3 + H + M$	→	$CH_3C_2H + M$	$k_0 = 1.7 \times 10^{-26} k_\infty = 2.5 \times 10^{-10}$

Conducted experiments

- "Control" — control experiment with advection for average Solar activity conditions
- "Zero" — same as control, but without advection
- "V-Sens" — same as control, but with twice the meridional circulation in the thermo- and mesosphere
- "SolMax" — Solar maximum experiment with appropriate photolysis coefficients and winds

- “SolMin” — Solar minimum experiment with appropriate photolysis coefficients and winds
- “Wave” — same as control, but including an upward-propagating gravitational tidal wave

Appendix B

A Titan column chemistry model

In this appendix, a simple 1–D chemistry model is discussed that serves to demonstrate the basics of chemistry modeling. A simple model can be helpful as an educational tool to understand e.g. the influence of eddy diffusion or reaction rate constants on resulting concentrations. Also, the model can be used diagnostically with MOZART output to study the relative importance of different reactions for a given column in the model. In the latter case, only a single time step is computed to get production and loss rates.

Chemistry equation systems are *stiff*, i.e. in a given volume, e.g. a cubic cm of Titan's thermosphere—as the production and loss plots earlier in the thesis demonstrated—some reactions might take place a few times per second, while other, slower reactions might only happen (statistically speaking) once in a thousand (or even a million) seconds. This gives rise to a large range in chemical lifetimes—some species are formed and destroyed almost entirely in the same place, while others change only slowly due to chemistry and final concentrations depend more on diffusion and advection.

In a 1–D model, one possible algorithm to integrate the set of equations is the Quasi-Steady State Algorithm (QSSA; Jacobson, 2005). Here reactions are separated into three groups according to chemical lifetimes and different algorithms are used for each group: Very short-lived species are assumed to be entirely locally-determined, i.e. their concentrations can be computed using the steady-state assumption. Species of average chemical lifetime are integrated based on an exponential method. (The exponential assures that computed concentrations stay between 0 and 1.) Long-lived species change so slowly due to chemistry that their concentration is integrated linearly (forward Euler equation), as e.g. overshooting during an integration timestep is unlikely. If h is the time step, $P_{c,i,t}$ and $L_{c,i,t}$ are total production and loss rates for species i at time t and $\Lambda_{c,i,t}$ is the implicit loss coefficient ($L_{c,i,t}/N_{i,t}$) and $\gamma = h\Lambda_{c,i,t-h}$, new concentrations are calculated via (eq. 12.46 in Jacobson, 2005):

$$N_{i,t} = \begin{cases} N_{i,t-h} + h(P_{c,i,t-h} - L_{c,i,t-h}) & \gamma < 0.01 \\ N_{i,t-h}\exp(-h\Lambda_{c,i,t-h}) + P_{c,i,t-h}/\Lambda_{c,i,t-h}[1 - \exp(-h\Lambda_{c,i,t-h})] & 0.01 \leq \gamma \leq 10 \\ P_{c,i,t-h}/\Lambda_{c,i,t-h} & \gamma > 10 \end{cases}$$

To build a simple chemistry model, the reaction rates are read from a MOZART pre-processor file and temperature and eddy mixing profiles are set up. Photolysis coefficients are read for a given (fixed) Solar zenith angle from the MOZART photolysis table. Initial concentrations are taken from a MOZART run NetCDF output file. Finally, a time loop using the QSSA method is started. In diagnostic mode, only one timestep is computed, as one is simply interested in obtaining the production and loss rates for a given species.

The Python programming language is used here to give an abbreviated outline of such a toy model. (The number sign, "#", is used for comments in the Python source code.) The model will not run as shown because some subroutines have been left out for brevity. Still, it serves to illustrate that the core of a chemistry model can be functionally relatively compact and straightforward:

```
### First information about level spacing, temperature are
### read from the MOZART file. Tind, latind, and lonind are
### the time step and  column position respectively.

ncfn = 'h0008.nc'
ncfile = NetCDFFile(ncfn, 'r')
tind, latind, lonind = -1, 16, 0
temp = ncfile.variables['T'][tind,:,latind,lonind]
plev = ncfile.variables['lev'][:]
pilev = ncfile.variables['ilev'][:]
ncfile.close()

# time step (s)
dt = 400.
# integration time (s)
ttot = 86400. * 365. * 10.
# the list of solution species:
sol = """H,␣C6H,␣CH3C2H,␣C2H5N,␣ND,␣N2P,␣N,␣NP,␣N2,␣CH4,
NH,␣CH3,␣CH2NH,␣H2,␣C2H2,␣CHCN,␣C2H4,␣CH3CN,␣C2H3,␣C2H6,
C2H5,␣C3H4,␣C2H3CN,␣C3H6,␣C2H5CN,␣C4H4,␣C4H3N,␣C4H6,␣C4H5N,
X1CH2,␣CH2,␣XC4H2,␣C4H2,␣C6H2,␣C6H4,␣C7H4,␣C,␣CH,␣C2,␣C3H3,
C4H,␣C4H3,␣C3H8,␣C3H2,␣C2H,␣C4H5,␣C4H8,␣C4H10,␣C6H6,␣C3H5,
C3H7,␣C7H8,␣C8H2,␣C6H5,␣C10H10,␣C12H10,␣CN,␣HCN,␣H2CN,␣C2N,
CH2CN,␣NH3,␣C2N2,␣NH2,␣N2H4,␣N2H2,␣CH3NH2,␣N2H,␣N2H3,␣HC3N,
C5HN,␣C4N2,␣C3N,␣C5H5N,␣HC5N,␣e,␣H2O"""
# process flags:
do_chem   = True  # chemistry:
do_photo  = True  #   * photolysis
do_reac   = True  #   * other reactions
do_diff   = True  # diffusion (molecular/eddy)
do_output = True  # create ASCII history file

### Now initial species number densities are read from the
### MOZART output file. Also, arrays for production and loss
### rates are created:

ncfile = NetCDFFile(ncfn, 'r')
n['M'] = zeros(len(zlev), float)
for zr, h in enumerate(zlev):
  n['M'][zr] = t.press2numd(t.alt2press(h), temp[zr])
for x in sol:
  n[x] = zeros(len(zlev), float)
  p[x] = zeros(len(zlev), float)
  l[x] = zeros(len(zlev), float)
  n[x][:] = (n['M'][:] * ncfile.variables[x.upper()
                + '_VMR_avrg'][tind,:,latind,lonind])
ncfile.close()

### This function computes a reaction rate from the given
### parameters. The number of parameters determines which
### expression is used:

def comp_rate(rr, m, t):
  if len(rr) == 1: return rr[0]
  elif len(rr) == 2: return rr[0] * exp(rr[1] / t)
  else:
    k0   = rr[0] * (300. / t)**rr[1]
    kinf = rr[2] * (300. / t)**rr[3]
    try: x = rr[4]
    except: x = .6
    c = kinf * k0 * m / (kinf + k0 * m)
    c *= x **(1./(1.+(log10(k0*m/kinf))**2))
    return c

### Now the time loop is started, integrating for a total of
### ttot seconds with a time step of dt.
print "%.2f␣days␣total" % (ttot / 86400.)
while tcur < ttot:
  tcur += dt

### First the eddy and molecular diffusion fluxes are computed
### (not shown) and concentrations updated accordingly:
  if do_diff:
    for zr in range(len(zlev)):
      n[spc][zr] -= ((phi_m[zr] - phi_m[zr+1]) /
                     (zilev[zr]-zilev[zr+1]) * 1.e-5 * dt)
      n[spc][zr] -= ((phi_e[zr] - phi_e[zr+1]) /
                     (zilev[zr]-zilev[zr+1]) * 1.e-5 * dt)

### Now production and loss rates are calculated by summing
### photolysis and non-photolysis reactions.
  for spc in sol:
    for zr, z in enumerate(zlev):
      p[spc][zr] = 0.
      l[spc][zr] = 0.
  for zr, z in enumerate(zlev):
    if do_photo:
      for reac in j.keys():
        spc = j[reac]['spc']
        rate = j[reac]['dat'][zr] * n[spc][zr]
        l[spc][zr] += rate
        for pp in j[reac]['prod']:
          p[pp][zr] += rate
    if do_reac:
      for reac in r.keys():
        rate = comp_rate(r[reac]['rat'], n['M'][zr], temp[zr])
        for spc in r[reac]['spc']:
          if spc == 'M' and len(r[reac]['rat']) > 2: continue
          rate *= n[spc][zr]
        for spc in r[reac]['spc']:
          if spc == 'M': continue
        l[spc][zr] += rate
      for pp in r[reac]['prod']:
        if pp == 'M': continue
        p[pp][zr] += rate

### The model creates some text and PDF (not shown) output files
### with concentrations and production and loss rates:

  if do_output:
    for nspc, spc in enumerate(diagspc):
      ofile.write("t␣=␣%u␣;␣species␣%s\n" % (tcur, spc))
      for zr, z in enumerate(zlev):
        ofile.write("%4f␣%20f␣%20e\n" % (z, n[spc][zr],
          n[spc][zr]/n['M'][zr]))
      ofile.write("t␣=␣%u␣;␣species␣l_%s\n" % (tcur, spc))
      for zr, z in enumerate(zlev):
        ofile.write("%4f␣%20e\n" % (z, l[spc][zr]))
      ofile.write("t␣=␣%u␣;␣species␣p_%s\n" % (tcur, spc))
      for zr, z in enumerate(zlev):
        ofile.write("%4f␣%20e\n" % (z, p[spc][zr]))

### Here the QSSA method is used to update concentrations.
### (In diagnostic mode this step is not necessary.)
  if do_chem:
    for zr, z in enumerate(zlev):
      for spc in sol:
        ll = l[spc][zr] / n[spc][zr]
        if dt * ll < .01:     # linear
          n[spc][zr] += dt * (p[spc][zr] - l[spc][zr])
        elif .01 <= dt * ll <= 10:  # exponential
          e = exp(-dt*ll)
          n[spc][zr] = n[spc][zr] * e + p[spc][zr] / ll * (1. - e)
        else:          # steady-state
          n[spc][zr] = p[spc][zr] / ll

### And finally the VMR of molecular hydrogen at the top is fixed:
  n['H2'][0]  = 4.e-3 * n['M'][0]

### After the time loop: show how long the model took to run
print "run␣finished;␣%2u␣mins,␣%2u␣secs␣total" % (mm, ss)
```

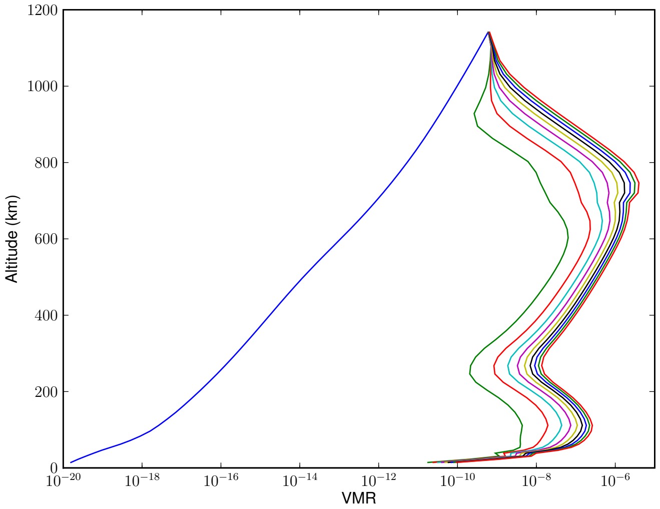

Figure B.1: Sample output from the Titan column model using an earlier version of the chemistry scheme, showing the time evolution of the benzene profile. Time interval between profiles is 100,000 s ($27.\overline{7}$ Earth hours) and the run begins with the initial benzene profile (blue line on the left), then quickly converges toward a relatively stable profile at $t = 900,000$ s (250 Earth hours).

Fig. B.1 shows the spin-up of the model from an initial profile during an integration time of 250 Earth hours. For the complete Titan chemistry scheme, even a diagnostic run with complete output of all species may take a few minutes. Execution speed of a simple bytecode-compiled model will typically be (at least) a factor of ten slower than MOZART, so this is not surprising. Therefore, for conducting runs with such a toy model, a smaller reaction set and number of solution species is usually desirable. Still, a toy model can serve as a useful adjunct to the actual FORTRAN production model and allows to verify the chemistry scheme is stable because QSSA is more sensitive to stability problems than MOZART's solver. MOZART may tolerate concentrations below 0 or above 1 if the number of grid points and species affected is low, and while this is is generally a desirable feature, it can also mask stability issues with the underlying chemistry scheme.

Appendix C

Cassini INMS validation data

In this appendix, the Cassini INMS retrievals are shown as height–VMR plots of relevant species. The data was supplied by J. Cui (pers. comm.; also used for analysis in Cui *et al.*, 2008). The blue dots denote the expectation values for VMRs and heights and error boxes are shown in red.

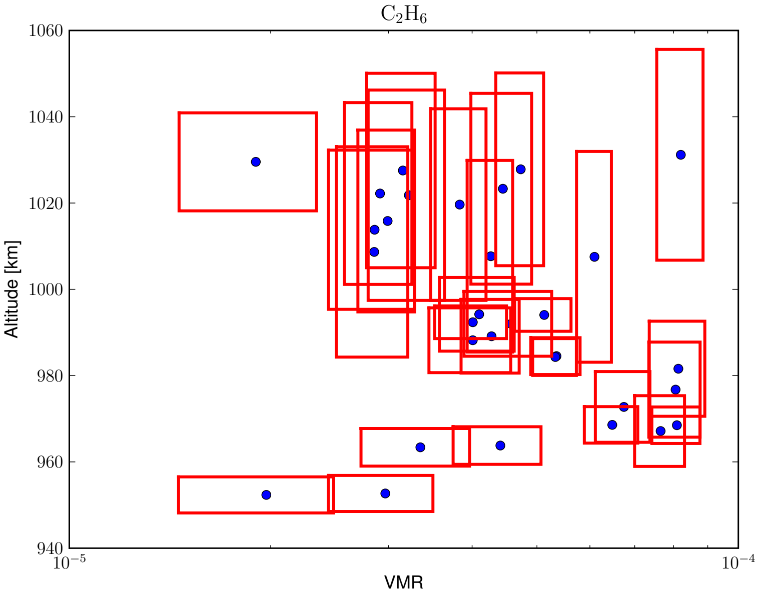

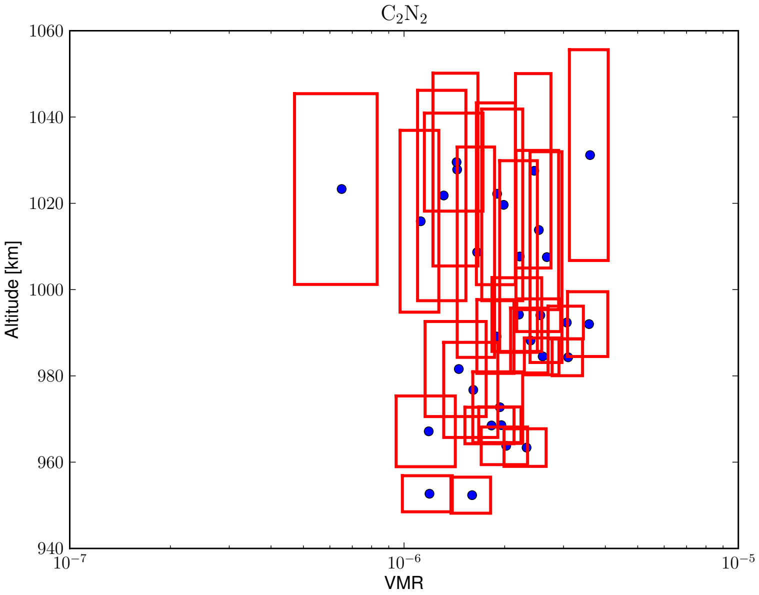
C_2N_2
1060
1040
1020
1000
980
960
940
Altitude [km]
10^{-7}
10^{-6}
10^{-5}
VMR

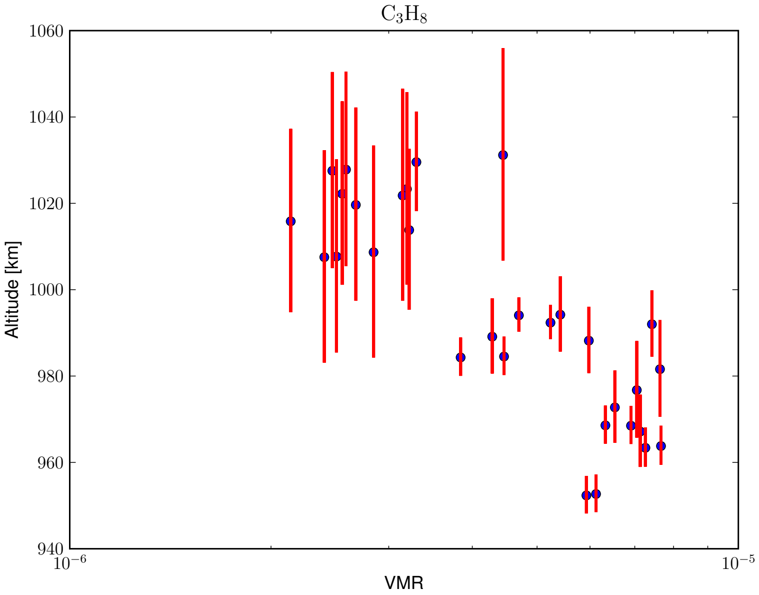
C_3H_8
1060
1040
1020
1000
980
960
940
Altitude [km]
10^{-6}
10^{-5}
VMR

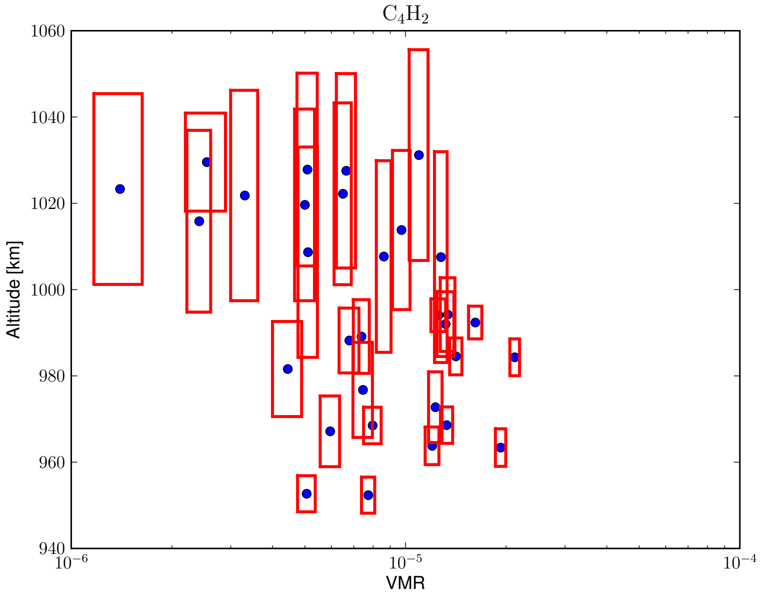
C_4H_2
1060
1040
1020
1000
980
960
940
Altitude [km]
10^{-6}
10^{-5}
10^{-4}
VMR

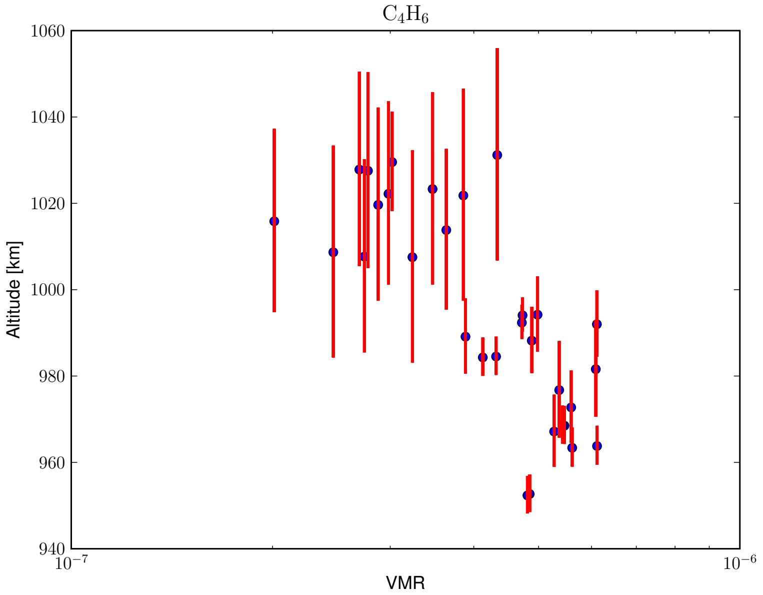
C_4H_6
1060
1040
1020
1000
980
960
940
Altitude [km]
10^{-7}
10^{-6}
VMR

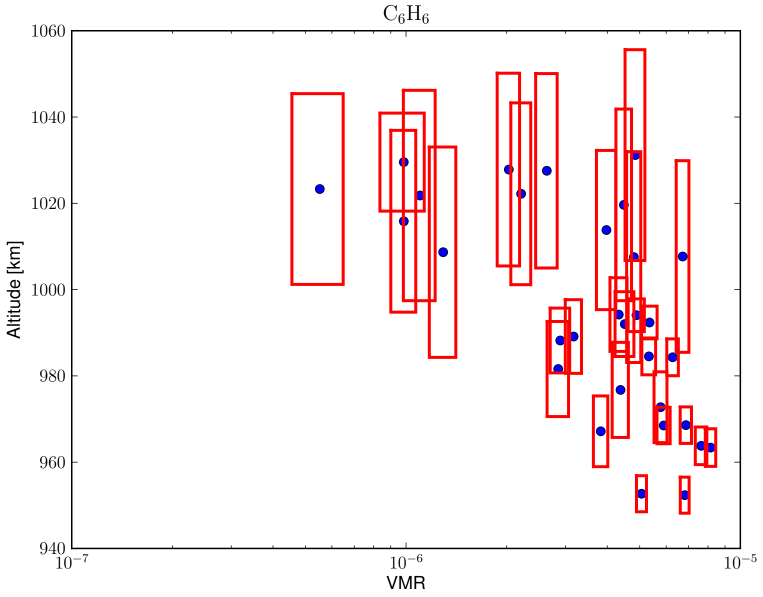
C_6H_6
1060
1040
1020
1000
980
960
940
Altitude [km]
10^{-7}
10^{-6}
10^{-5}
VMR

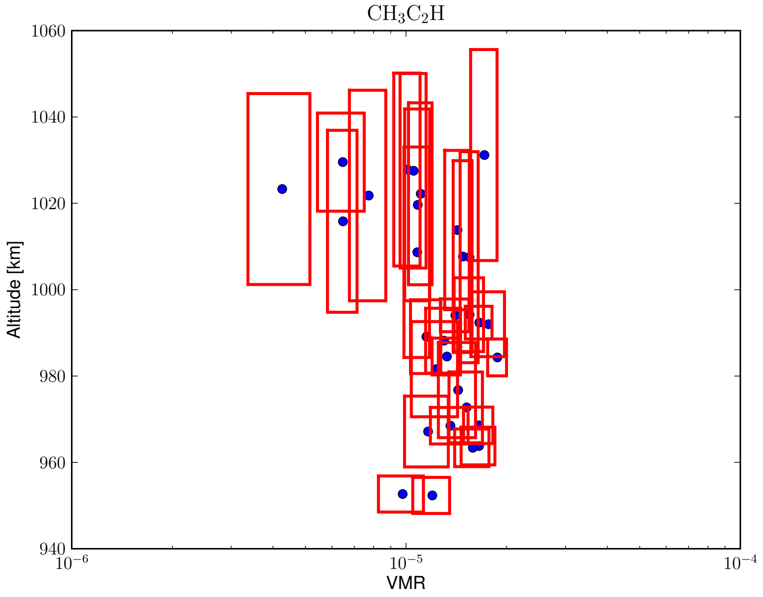
CH_3C_2H
1060
1040
1020
1000
980
960
940
Altitude [km]
10^{-6}
10^{-5}
10^{-4}
VMR

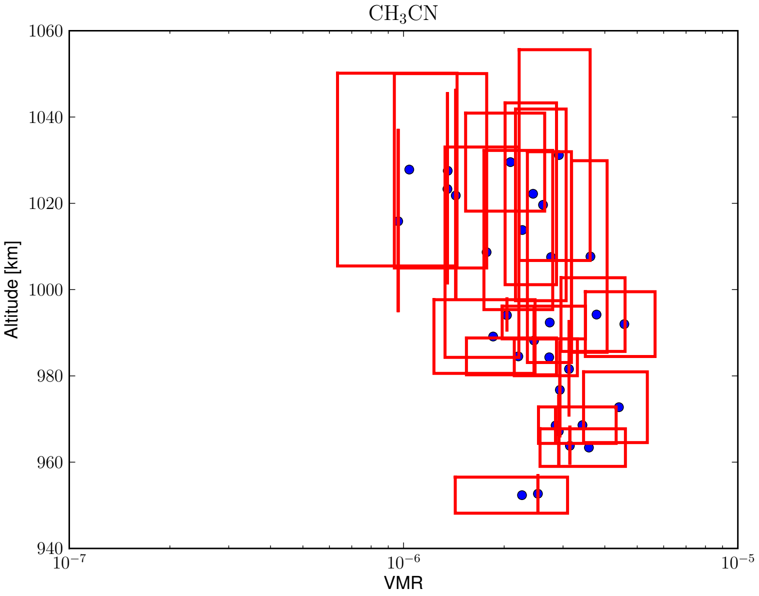
CH$_3$CN
1060
1040
1020
1000
980
960
940
Altitude [km]
10^{-7}
10^{-6}
10^{-5}
VMR

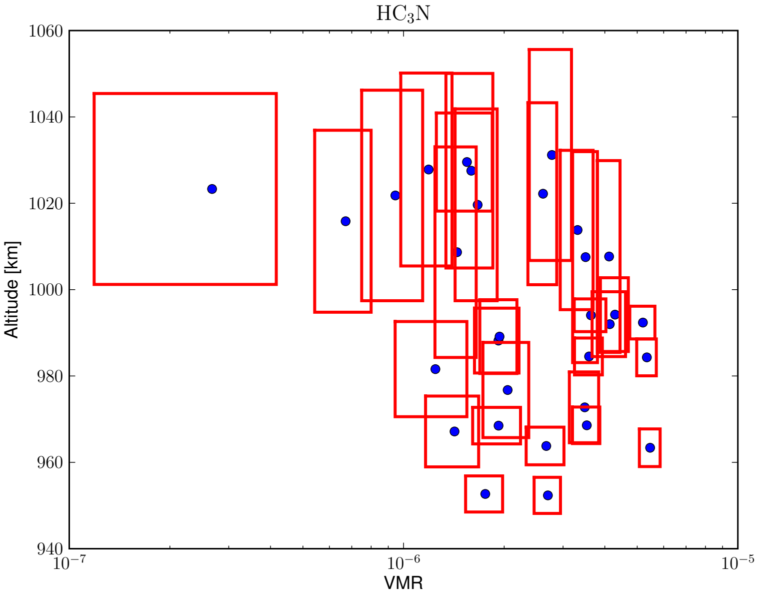
HC$_3$N
1060
1040
1020
1000
980
960
940
Altitude [km]
10^{-7}
10^{-6}
10^{-5}
VMR

Appendix D

Some names of chemical species

Chemical Formula	English Name	German Name
H	atomic hydrogen	Atomarer Wasserstoff
H_2	molecular hydrogen	Molekularer Wasserstoff
CH_3	methyl radical	Methylradikal
CH_3C_2H	methylacetylene (propyne)	Propin (Methylacetylen)
CH_4	methane	Methan
C_2H_2	acetylene	Ethin (auch Azetylen)
C_2H_4	ethylene (ethene)	Ethen (auch Ethylen)
C_2H_6	ethane	Ethan
C_3H_3	propargyl radical	Propargylradikal
C_3H_8	propane	Propan
C_4H_2	diacetylene (butadiyne)	Diazetylen
C_4H_6	1,3-butadiene	1,3-Butadien (Vinylethylen)
C_6H_6	benzene	Benzol (Benzen)
HCN	hydrogen cyanide	Cyanwasserstoff (Blausäure)
HC_3N	cyanoacetylene	Cyanoazetylen
CH_3CN	acetonitrile	Azetonitril
C_2H_3CN	acrylonitrile	Acrylnitril
C_2N_2	cyanogen	Dicyan
N	atomic nitrogen	Atomarer Stickstoff
N_2	molecular nitrogen	Molekularer Stickstoff
NH_3	ammonia	Ammoniak

Appendix E

Glossary and list of abbreviations

- advection—transport by wind
- CICLOPS—Cassini Imaging Central Laboratory for Operations
- CIRS—Cassini Infrared Spectrometer
- CS—(absorption) cross section
- CTM—Chemistry Transport Model
- Dec—declination
- GITM—Global Ionosphere–Thermosphere Model
- HASI—Huygens Atmospheric Structure Instrument (Huygens lander instrument)
- IAU—International Astronomical Union
- INMS—Ion and Neutral Mass Spectrometer (Cassini instrument)
- IRIS—Voyager Infrared Interferometer Spectrometer, the precursor to CIRS
- JPL—Jet Propulsion Laboratory
- life time—a measure for the relative importance of process; shorter life times mean higher relevance of either transport or chemistry, respectively
- LST—Local Solar Time

- MOZART—Model of Ozone and Related Tracers, a CTM for Earth's tropo- and stratosphere
- NH—Northern Hemisphere
- NP—North Pole
- ODR–Orthogonal Distance Regression
- photolysis—dissociation of a molecule due to absorption of UV radiation
- polymer—large molecules (macromolecules) composed of repeating subunits (monomers). If the monomers can bond to only *two* other monomers each, a chain-like polymer is formed, otherwise more complex, cross-linked structures are possible.
- polyyne—a group of organic compounds with alternating single and triple bonds, such as diacetylene (C_4H_2) and triacetylene (C_6H_2)
- QY—quantum yield
- RA—right ascension
- SH—Southern Hemisphere
- SP—South Pole
- tide—1. Gravitational tide: The effect of the gravity of e.g. the Sun or the Moon for Earth, or in the case of Titan, Saturn, which leads to an accumulation of atmospheric mass in the direction (and opposite direction) towards the other body. 2. Radiative tide: The effect caused by the diurnal cycle heating which causes an atmosphere to swell vertically during the day when it is heated.
- UV—ultraviolet (radiation)
- UVIS—Ultraviolet Imaging Spectrograph (Cassini instrument)
- UVS—Ultraviolet Spectrometer (Voyager instrument), the precursor of UVIS
- VMR—Volume Mixing Ratio

References

Achterberg, R. K., B. J. Conrath, P. J. Gierasch, F. M. Flasar, and C. A. Nixon (2008): Titan's middle-atmospheric temperatures and dynamics observed by the Cassini Composite Infrared Spectrometer. *Icarus*, **194**, 263–277.

Atreya, S., E. Y. Adams, H. B. Niemann, J. E. Demick-Montelara, T. C. Owen, M. Fulchignoni, F. Ferri, and E. H. Wilson (2006): Titan's methane cycle. *Planetary and Space Science*, **54**, 1177–1187.

Atreya, S. (2007): Titan's organic factory. *Science*, **316**, 843–845.

Banks, P. M. and G. Kockarts (1973): *Aeronomy.* Academic Press, New York, 430 pp.

Bell, J. M.: The dynamics in the upper atmospheres of Mars and Titan. Ph.D. dissertation, University of Michigan, 2008.

Boggs, P. T., R. H. Byrd, and R. B. Schnabel (1985): A stable and efficient algorithm for nonlinear orthogonal distance regression. University of Colorado Department of Computer Science Technical Report Number CU-CS-317-85.

Brasseur, G. P., D. A. Hauglustaine, S. Walters, P. J. Rasch, J.-F. Müller, C. Granier, and X. X. Tie (1998): MOZART, a global chemical transport model for ozone and related chemical tracers 1. Model description. J Geophys Res-Atmos, **103**, 28265–28289.

Brown, R. H., L. A. Soderblom, J. M. Soderblom, R. N. Clark, R. Jaumann, J. W. Barnes, C. Sotin, B. Buratti, K. H. Baines, and P. D. Nicholson (2008): The identification of liquid ethane in Titan's Ontario Lacus. *Nature*, **454**, 607–610.

Canosa, A., A. Paramo, S. D. Le Picard, and I. R. Sims (2007): An experimental study of the reaction kinetics of C2(X1[Sigma]g+) with hydrocarbons (CH4, C2H2, C2H4, C2H6 and C3H8) over the temperature range 24–300 K: Implications for the atmospheres of Titan and the Giant Planets, *Icarus*, **187**, 558–568.

Coustenis, A. and Bezard (1995): Titan's atmosphere from Voyager infrared observations, IV. Latitudinal variations of temperature and composition of Titan's equatorial region. *Icarus*, **80**, 54–76.

Coustenis, A., R. K. Achterberg, B. J. Conrath, D. E. Jennings, A. Marten, D.

Gautier, C. A. Nixon, F. M. Flasar, N. A. Teanby, B. Bézard, R. E. Samuelson, R. C. Carlson, E. Lellouch, G. L. Bjoraker, P. N. Romani, F. W. Taylor, P. G. J. Irwin, T. Fouchet, A. Hubert, G. S. Orton, V. G. Kunde, S. Vinatier, J. Mondellini, M. M. Abbas, and R. Courtin (2007): The composition of Titan's stratosphere from Cassini/CIRS mid-infrared spectra. *Icarus*, **189**, 35–62.

Coustenis, A. and F. W. Taylor (2008): *Titan: Exploring an Earthlike World.* Series on Atmospheric, Oceanic and Planetary Physics, World Scientific Publishing Company, 130 pp.

Cui, J., R. V. Yelle, V. Vuitton, J. H. Waite, W. T. Kasprzak, D. A. Gell, H. B. Niemann, I. C. F. Mueller-Wodarg, N. Borggren, G. G. Fletcher, E. L. Patrick, E. Raaen, and B. A. Magee (2009): Analysis of Titan's neutral upper atmosphere from Cassini Ion Neutral Mass Spectrometer measurements. *Icarus*, **200**, 581–615.

Dobrijevic, M., E. Hebrard, S. Plessis, N. Carrasco, P. Pernot, M. Bruno-Claeys (2009): Comparison of methods for the determination of key reactions in chemical systems: Application to Titan's atmosphere, *Advances in Space Research*, **45**, 77–91.

Doege, M. C., D. R. Marsh, G. P. Brasseur, I. Mueller-Wodarg, T. Tokano, and C. E. Newman (2008): A 3-D Chemistry Transport Model for Titan's Thermosphere. American Geophysical Union, Fall Meeting 2008, abstract #P21A-1336.

Fulchignoni, M., F. Ferri, F. Angrilli, A. J. Ball, A. Bar-Nun, M. A. Barucci, C. Bettanini, G. Bianchini, W. Borucki, G. Colombatti, M. Coradini, A. Coustenis, S. Debei, P. Falkner, G. Fanti, E. Flamini, V. Gaborit, R. Grard, M. Hamelin, A. M. Harri, B. Hathi, I. Jernej, M. R. Leese, A. Lehto, P. F. Lion Stoppato, J. J. López-Moreno, T. Mäkinen, J. A. M. McDonnell, C. P. McKay, G. Molina-Cuberos, F. M. Neubauer, V. Pirronello, R. Rodrigo, B. Saggin, K. Schwingenschuh, A. Seiff, F. Simões, H. Svedhem, T. Tokano, M. C. Towner, R. Trautner, P. Withers, and J. C. Zarnecki (2005): *In situ* measurements of the physical characteristics of Titan's environment. *Nature*, **438**, pp.785–791.

Giorgini, J.D., Yeomans, D.K., Chamberlin, A.B., Chodas, P.W., Jacobson, R.A., Keesey, M.S., Lieske, J.H., Ostro, S.J., Standish, E.M., Wimberly, R.N. (1996): JPL's On-Line Solar System Data Service, *Bulletin of the American Astronomical Society*, **28**, 1158.

Hébrard, E., M. Dobrijevic, Y. Bénilan, and F. Raulin (2006): Photochemical kinetics uncertainties in modeling previous termTitan'snext term atmosphere: a review, *J. Photochem. Photobiol.*, **C 7**, 211–230.

Hebrard, E., M. Dobrijevic, Y. Bénilan, and F. Raulin (2007): Photochemical kinetics uncertainties in modeling Titan's atmosphere: First consequences. *PaSS*, **55**, 1470–1489.

Horowitz, L. W., S. Walters, D. L. Mauzerall, L. K. Emmons, P. J. Rasch, C.

Granier, X. Tie, J.-F. Lamarque, M. G. Schultz, G. S. Tyndall, J. J. Orlando, and G. P. Brasseur (2003): A global simulation of tropospheric ozone and related tracers: Description and evaluation of MOZART, version 2. *J. Geophys. Res.*, **108**, 4784.

Hourdin, F., P. Levan, O. Talagrand, R. Courtin, D. Gautier, and C. P. McKay (1995): Numerical simulation of the general circulation of the atmosphere of Titan. *Icarus*, **117**, 358–374.

Imanaka (2004): Laboratory experiments of Titan tholin formed in cold plasma at various pressures: implications for nitrogen-containing polycyclic aromatic compounds in Titan haze. *Icarus*, **168**, pp. 344–366.

Jacobson, M. Z. (2005): Fundamentals of Atmospheric Modeling. Cambridge University Press, 828 pp.

Jacobson, R. A., P. G. Antreasian, J. J. Bordi, K. E. Criddle, R. Ionasescu, J. B. Jones, R. A. Mackenzie, M. C. Meek, D. Parcher, F. J. Pelletier, W. M. Owen, Jr.1, D. C. Roth, I. M. Roundhill, and J. R. Stauch (2006): The gravity field of the Saturnian system from satellite observations and spacecraft tracking data. *Astron. J.*, **132**, 2520–2526. doi:10.1086/508812

Kinnison, D. E., G. P. Brasseur, S. Walters, R. R. Garcia, D. R. Marsh, F. Sassi, V. L. Harvey, C. E. Randall, L. Emmons, J.-F. Lamarque, P. Hess, J. J. Orlando, X. X. Tie, W. Randel, L. L. Pan, A. Gettelman, C. Granier, T. Diehl, U. Niemeier, A. J. Simmons (2007): Sensitivity of chemical tracers to meteorological parameters in the MOZART-3 chemical transport model. *J. Geophys. Res.*, **112**, doi: 10.1029/2006JD007879.

Krasnopolsky, V. (2009): A photochemical model of Titan's atmosphere and ionosphere. *Icarus*, **201**, 226.

Kuiper, G. P. (1944): Titan: a satellite with an atmosphere. *Astrophys. J.*, **100**, 378–383.

Lara, L. M., E. Lellouch, J. J. López-Moreno, and R. Rodrigo (1996): Vertical distribution of Titan's atmospheric neutral constituents. *J Geophys Res-Planet.*, **101**, 23261–23283.

Lassell (1847): Observations of Mimas, the closest and most interior satellite of Saturn. *Monthly Notices of the Royal Astronomical Society*, **8**, 42.

Lavvas, P. P., A. Coustenis, and I. M. Vardavas (2008a): Coupling photochemistry with haze formation in Titan's atmosphere, Part I: Model description. *PaSS*, **56**, 27–66.

Lavvas, P. P., A. Coustenis, and I. M. Vardavas (2008b): Coupling photochemistry with haze formation in Titan's atmosphere, Part II: Results and validation with Cassini/Huygens data. *PaSS*, **56**, 67–99.

Lavvas, P., R. V. Yelle, and V. Vuitton (2009): The detached haze layer in Titan's mesosphere. *Icarus*, **201**, 626–633.

Lebonnois, S., D. Toublanc, F. Hourdin, and P. Rannou (2001): Seasonal variations of Titan's atmospheric composition. *Icarus*, **152**, 384–406.

Lebonnois, S., E. L. O. Bakes, and C. P. McKay (2002): Transition from gaseous compounds to aerosols in Titan's atmosphere, *Icarus*, **159**, 505–517.

Lebonnois, S. and D. Toublanc (1999): Actinic fluxes in Titan's atmosphere, from one to three dimensions: application to high-latitude composition. *J Geophys Res-Planet.*, **104**, 22025–22034.

Liang, M.-C., A. Heays, B. Lewis, S. Gibson, and Y. Yung (2007a): Source of nitrogen isotope anomaly in HCN in the atmosphere of Titan. *Astrophys J*, **664**, L115–L118.

Liang, M.C., Yung, Y. L., and Shemansky, D. E. (2007b): Photolytically generated aerosols in the mesosphere and thermosphere of Titan. *Astrophys J*, **661**, L199–L202.

Lin, S. and R. B. Rood (1997): An explicit flux-form semi-Lagrangian shallow-water model on the sphere. *Q J Roy Meteor Soc*, **123**, 2477–2498.

Matthews, C.N. (1995): Hydrogen cyanide polymers: from laboratory to space, *Planetary and Space Science*, **43**, Issues 10–11, Dust, Molecules and Backgrounds: from Laboratory to Space, 1365–1370.

McEwan, M. J. and L. F. Phillips: *Chemistry of the atmosphere.* Edward Arnold Ltd, London 1975, 301 pp.

McKay, C. P., A. Coustenis, R. E. Samuelson, M. T. Lemmon, R. D. Lorenz, M. Cabane, P. Rannou, and P. Drossart (2001): Physical properties of the organic aerosols and clouds on Titan. *Planetary and Space Science*, **49**, 79–99.

Mitri, G., A. P. Showman, J. I. Lunine, and R. D. Lorenz (2007): Hydrocarbon Lakes on Titan. *Icarus*, **186**, 385–394.

Mueller-Wodarg, I. C. F., R. V. Yelle, M. Mendillo, L. A. Young, and A. D. Aylward (2000): The thermosphere of Titan simulated by a global 3-dimensional time-dependent model, *J. Geophys. Res.*, **105**, 20833–20856.

Mueller-Wodarg, I. C. F., R. V. Yelle, M. Mendillo, and A. D. Aylward (2003): On the global distribution of neutral gases in Titan's upper atmosphere and its effect on the thermal structure, *J. Geophys. Res.*, **108**, 1453, doi:10.1029/2003JA010054.

Mueller-Wodarg, I. C. F., R. V. Yelle, N. Borggren, and J. H. Waite Jr. (2006): Waves and horizontal structures in Titan's thermosphere. *J. Geophys. Res.*, **111**, 16.

Mueller-Wodarg, I. C. F. (2002). The application of general circulation models to the atmospheres of terrestrial-type moons of the giant planets. Geophysical monograph, **130**, 398 pp.

Mueller-Wodarg, I. C. F., R. V. Yelle, M. J. Mendillo, and A. D. Aylward (2003): On the global distribution of neutral gases in Titan's upper atmosphere and its effect on the thermal structure. *J. Geophys. Res.*, **108**, 1453.

Mueller-Wodarg, I. C. F., R. V. Yelle, M. Mendillo, L. A. Young, A. D. Aylward (2000): The thermosphere of Titan simulated by a global three-dimensional time-dependent model. *J Geophys Res.*, **105**, 20833–20856.

Mueller-Wodarg, I. C. F., R. V. Yelle, J. Cui, and J. H. Waite (2008): Horizontal structures and dynamics of Titan's thermosphere. JGR, **113**, doi:10.1029/2007JE003033.

Porco, C. C., E. Baker, J. Barbara, K. Beurle, A. Brahic, J. A. Burns, S. Charnoz, N. Cooper, D. D. Dawson, A. D. Del Genio, T. Denk, L. Dones, U. Dyudina, M. W. Evans, S. Fussner, B. Giese, K. Grazier, P. Helfenstein, A. P. Ingersoll, R. A. Jacobson, T. V. Johnson, A. McEwen, C. D. Murray, G. Neukum, W. M. Owen, J. Perry, T. Roatsch, J. Spitale, S. Squyres, P. Thomas, M. Tiscareno, E. P. Turtle, A. R. Vasavada, J. Veverka, R. Wagner, and R. West (2005): Imaging of Titan from the Cassini spacecraft. *Nature*, **434**, 159–168.

Rannou, P., F. Hourdin, C.P. McKay and D. Luz (2004): A coupled dynamics-microphysics model of Titan's atmosphere, *Icarus*, **170**, pp. 443–479.

Rannou, P., S. Lebonnois, F. Hourdin, and D. Luz (2005): Titan atmosphere database. *Adv Spc Res*, **36**, 2194–2198.

Richardson, M. I., A. D. Toigo, and C. E. Newman (2007): PlanetWRF: A general purpose, local to global numerical model for planetary atmospheric and climate dynamics. *J. Geophys. Res.,* **112**, doi:10.1029/2006JE002825.

Ridley, A. J., Y. Deng, and G. Toth (2006): The global ionosphere thermosphere model, *Journal of Atmospheric and Terrestrial Physics*, **68**, 839–864, doi:10.1016/j.jastp.2006.01.008.

Ruiz-Bermejo, M., C. Menor-Salvan, J. L. de la Fuente, E. Mateo-Marti, S. Osuna-Esteban, J. A. Martin-Gago, S. Veintemillas-Verdaguer (2009): CH4/N2/H2-spark hydrophobic tholins: A systematic approach to the characterisation of tholins. Part II, *Icarus*, **204**, 672–680.

Sagan, C. and B. N. Khare (1979): Tholins: organic chemistry of interstellar grains and gas. *Nature*, **277**, 102.

Sharma, P. and S. Byrne (2010): Constraints on Titan's topography through fractal analysis of shorelines. Icarus, **209**, 723–737.

Shemansky, D. E., A. I. F. Stewart, R. A. West, L. W. Esposito, J. T. Hallett, and X. Liu (2005): The Cassini UVIS Stellar Probe of the Titan Atmosphere. *Science*, **308**, 978–982.

Stiles, B. W., R. L. Kirk, R. D. Lorenz, S. Hensley, E. Lee, S. J. Ostro, M. D. Allison, P. S. Callahan, Y. Gim, L. Iess, P. P. del Marmo, G. Hamilton, W. T. K. Johnson, R. D. West, and The Cassini RADAR team (2008): Determining Titan's Spin State from Cassini RADAR images. *The Astronomical Journal*, **135**, 1669–1680.

Stofan, E. R. Lunine, J. I., Lopes, R., Paganelli, F., Lorenz, R. D., Wood, C.

A., Kirk, R., Wall, S., Elachi, C., Soderblom, L. A., Ostro, S., Janssen, M., Radebaugh, J., Wye, L., Zebker, H., Anderson, Y., Allison, M., Boehmer, R., Callahan, P., Encrenaz, P., Flamini, E., Francescetti, G., Gim, Y., Hamilton, G., Hensley, S., Johnson, W. T. K., Kelleher, K., Muhleman, D., Picardi, G., Posa, F., Roth, L., Seu, R., Shaffer, S., Stiles, B., Vetrella, S., West, R. (2006): Mapping of Titan: Results from the first Titan radar passes. *Icarus*, **185**, 443–456.

Strobel, D. F. (1982): Chemistry and evolution of Titan's atmosphere. *Planet. Space Sci.*, **30**, 839–848.

Strobel, D. F. (2006): Gravitational tidal waves in Titan's upper atmosphere. *Icarus*, **182**, 251–258.

Teanby, N. A., P. G. J. Irwin, R. de Kok, C. A. Nixon, A. Coustenis, E. Royer, S. B. Calcutt, N. E. Bowles, L. Fletcher, C. Howett, and F. W. Taylor (2008): Global and temporal variations in hydrocarbons and nitriles in Titan's stratosphere for northern winter observed by Cassini/CIRS. *Icarus*, **193**, 595–611.

Teanby, N. A., R. de Kok, and P. G. J. Irwin (2009): Small-scale composition and haze layering in Titan's polar vortex, *Icarus*, **204**, 645–657, ISSN 0019-1035, DOI: 10.1016/j.icarus.2009.07.027.

Tokano, T., F. M. Neubauer, M. Laube, and C. P. McKay (1999): Seasonal variation of Titan's atmospheric structure simulated by a general circulation model. *Planetary and Space Science*, **47**, 493–520.

Tokano, T. (2002): Tidal Winds on Titan Caused by Saturn. *Icarus*, **158**, 499–515.

Tokano, T., C. P. McKay, F. M. Neubauer, S. K. Atreya, F. Ferri, M. Fulchignoni, and H. B. Niemann (2006): Methane drizzle on Titan. *Nature*, **442**, 432–435.

Tokano, T. (2008): Dune-forming winds on Titan and the influence of topography. *Icarus*, **194**, 243–262.

Tokano, T. (2008): The Dynamics of Titan's troposphere. *Phil. Trans. R. Soc. A*, **367**, 633–648.

Tokano, T. (2009): Impact of Seas/Lakes on Polar Meteorology of Titan: Simulation by a Coupled GCM-Sea Model. *Icarus*, **204**, 619–636.

Tokano, T. (2010): Relevance of fast westerlies at equinox for the eastward elongation of Titan's dunes. *Aeolian Research*, in press. Available online 23 May 2010, ISSN 1875-9637, DOI: 10.1016/j.aeolia.2010.04.003.

Toublanc, D., J. P. Parisot, J. Brillet, D. Gautier, F. Raulin and C. P. McKay (1995): Photochemical Modeling of Titan's Atmosphere. *Icarus*, **113**, 2–26.

Viereck and Puga (1999): The NOAA Mg II core-to-wing solar index: Construction of a 20-year time series of chromospheric variability from multiple satellites., *JGR*, **104**, 9995–10005.

Waite, H. (2005): Ion Neutral Mass Spectrometer Results from the First Flyby of Titan. *Science*, **308**, 982–986.

Walterscheid, R. L., G.Schubert (2006): A tidal explanation for the Titan haze layers, *Icarus*, **183**, 471–478.

Wilks, D. J. (1995): *Statistical methods in the atmospheric sciences.* International Geophysics Series, Volume 59, Academic Press, Oxford, 467 pp.

Wilson, E. and S. Atreya (2004): Current state of modeling the photochemistry of Titan's mutually dependent atmosphere and ionosphere. *J. Geophys. Res.*, **109**, 39.

Woods, T. and G. Rottman (2002): Solar ultraviolet variability over time periods of aeronomic interest, in Comparative Aeronomy in the Solar System, edited by M. Mendillo, A. Nagy, and J. Hunter Waite, Jr., Geophys. Monograph Series, Wash. DC, 221–234.

Yelle, R. V., N. Borggren, V. de La Haye, W. T. Kasprzak, H. B. Niemann, I. Müller-Wodarg, J. H. Waite (2006): The vertical structure of Titan's upper atmosphere from Cassini Ion Neutral Mass Spectrometer measurements. *Icarus*, **182**, 567–576.

Yelle, R. V. (1991): Non-LTE models of Titan's upper atmosphere. *Astrophys J*, **383**, 380–400.

Yelle, R. V., D. F. Strobel, E. Lellouch and D. Gautier (1997): Engineering models for Titan's atmosphere. Huygens: Science, Payload and Mission, Proceedings of an ESA conference, 243.

Yung, Y. L., M. Allen, J. P. Pinto (1984): Photochemistry of the atmosphere of Titan. *Icarus*, **72**, 468–472.

Zebker, H.A., Y. Gim, P. Callahan, S. Hensley, R. Lorenz and The Cassini Radar Team (2009): Analysis and interpretation of Cassini Titan radar altimeter echoes, *Icarus*, **200**, 240–255.

Zhu, X. (2006): Maintenance of equatorial superrotation in the atmospheres of Venus and Titan. *Planetary and Space Science*, **54**, 761–773.

Acknowledgments

The author would like to thank Prof. Guy P. Brasseur for suggesting Titan's atmospheric chemistry as the thesis theme and his valuable insights into chemistry modeling, Daniel R. Marsh from ACD (NCAR) for his insightful comments, and Prof. Joachim Saur and Tetsuya Tokano for supporting this cooperation between NCAR and the University of Cologne and their general guidance.

I am indebted to Tetsuya Tokano, Jun Cui, Jared Bell, Claire Newman, and Ingo Mueller-Wodarg for sharing their model or observational data and the helpful discussions I have had with them.

Furthermore, I am grateful to Eric H. Wilson for his encouragement and providing his cross section and quantum yield data. Stacy Walters and Garth D'Attilo of ACD have been an important source of computing support for the various ACD computers as well as NCAR high-performance compute servers.

Finally, I would like to thank the developers of Python, NumPy, SciPy, Matplotlib, Apple Keynote, LyX, and AT&T Graphviz for creating such excellent software that is truly a pleasure to use.

All images by NASA and the NASA Jet Propulsion Laboratory (JPL) are in the Public Domain as per the NASA copyright policy which states that "NASA material is not protected by copyright unless noted", see `http://www.jsc.nasa.gov/policies.html#Guidelines` and `http://www.jpl.nasa.gov/images/policy/`.

Erklärung

Ich versichere, dass ich die von mir vorgelegte Dissertation selbständig angefertigt, die benutzten Quellen und Hilfsmittel vollständig angegeben und die Stellen der Arbeit – einschließlich Tabellen, Karten und Abbildungen –, die anderen Werken im Wortlaut oder im Sinn nach entnommen sind, in jedem Einzelfall als Entlehnung kenntlich gemacht habe; dass diese Dissertation noch keiner anderen Fakultät oder Universität zur Prüfung vorgelegen hat; dass sie – abgesehen von unten angegebenen Teilpublikationen – noch nicht veröffentlicht worden ist sowie, dass ich eine solche Veröffentlichung vor Abschluss des Promotionsverfahrens nicht vornehmen werde. Die Bestimmungen der Promotionsordnung sind mit bekannt. Die von mir vorgelegte Dissertation ist von Prof. Joachim Saur und Prof. Guy P. Brasseur betreut worden.

....

Hamburg, den

Lebenslauf

Geburtsdatum: 26.12.1976
Geburtsort: Hamburg
Staatsangehörigkeit: Deutsch
Schulbildung:
1983–1987 Grundschule Bockhorster Weg, Stade
1987–1989 Orientierungsstufe Hohenwedel, Stade
1989–1996 Vincent-Lübeck-Schule, Stade
Studium:
1997–2003 Diplom in Meteorologie, Universität Hamburg
Berufliche Tätigkeiten:
2000–2001 Abteilung für Theoretische Meteorologie, Universiät Hamburg
2006–2009 National Center for Atmospheric Research, Boulder, Colorado, USA

....

Hamburg, den